Detection of chromium and mercury in water using rGO incorporated Cu-based nanomaterials

by

Moremi Harold

DISSERTATION

submitted in fulfilment of the

requirements for the degree of

Qualification

in

Master of science (Chemistry)

in the

FACULTY OF SCIENCE AND AGRICULTURE

(school of physical and minerals)

at the

UNIVERSITY OF LIMPOPO

Supervisors: Dr. P.M. Shumbula

Mr. C. Maswanganyi

Dr. A. Jijana (MINTEK)

2024

ABSTRACT

Heavy metal ions can build up for years or even decades in a number of body organs. Heavy metal poisoning symptoms have the potential to be fatal and to cause permanent harm. According to the United States Environmental Protection Agency (EPA), heavy metals such as chromium, nickel, cadmium, copper, lead, mercury, and arsenic are classified as the most toxic, hence it is important to be able to find simple, rapid methods to detect them in either wastewater or drinking water. In this research study, Cu-based nanomaterials on reduced graphene oxide (RGO) are prepared and then used as an electrocatalyst for the detection of chromium(III) and mercury(II). Copper oxide (CuO) and copper sulfide (CuS) nanoparticles (NPs) were prepared using co-precipitation method and chemical reduction method, respectively. Copper chloride dihydrate ($CuCl_2.2H_2O$) was employed as a metal source in both methods. In the case of copper sulfide nanoparticles, thioacetamide (TAA) was employed as the sulfur source in the presence of GSH (Glutathione), which was employed as a capping agent. Both CuONPs and CuSNPs were also coated with Gold (Au) to form polyhedral hetero-structure composed of both gold nanoparticles and CuO nanoparticles. The prepared CuO, CuS, CuO-Au and CuS-Au were then incorporated on RGO using different chemical processes in order to produce CuO/RGO, CuS/RGO, CuO-Au/RGO and CUS-Au/RGO nanocomposites. All prepared nanoparticles and nanocomposites were characterized with ultraviolet visible (UV-Vis) spectroscopy, X-ray diffraction (XRD), energy dispersive X-ray (EDX) spectroscopy, transmission electron microscopy (TEM), fourier-transform infrared (FTIR) microscopy and Raman spectroscopy. In addition, glassy carbon electrodes (GCEs) modified with CuO, CuS, CuO-Au, CuS-Au CuO/RGO, CuS/RGO, CuO-Au/RGO and CUS-Au/RGO were prepared, and the electrochemical activities of each modified electrode were investigated using the $[Fe(CN)_6]^{3-/4-}$ probe via cyclic voltammetry (CV) and electrochemical impedance spectroscopy (EIS). CuS-Au/RGO exhibited high electron transfer with low resistance charge transfer (R_{ct}) by EIS analysis. Therefore, was chosen as the material of interest during the development of the electrochemical sensor for both Cr(III) and Hg (II) heavy metal ions. The sensor parameters such as scan rate, pH and deposition potential and time were optimized. The CUS-Au/RGO showed good stability

and reactivity at pH of 6.17. The fabricated sensor exhibited very low detection limits of 2 ppb for Hg(II) and 2 ppb for Cr(III). However, the CuS-Au/RGO nanocomposite based electrochemical sensor evidently demonstrated to have a strong binding affinity and preference for Hg(II) than Cr(III)

DECLARATION

I hereby declare that “Detection of chromium and mercury in water using RGO incorporated Cu-based nanomaterials” is my own work and that all the sources used to compile this work are acknowledged and indicated in the form of references.

_____on this _____10th_____day of _____July_____ 2024___

Moremi H (Student [redacted]

DEDICATIONS

This work is dedicated to my late father and brother.

Albert and Kenneth Moremi

ACKNOWLEDGEMENTS

Without the assistance and guidance of multiple people who each made a unique contribution and extension, this dissertation would not have been feasible. I'm grateful to everyone who helped make this research project feasible with their invaluable support during its planning and execution.

I would like to express my sincere gratitude to my three supervisors (Dr. P.M Shumbula, Dr. A.N Jijana and Mr C. Maswanganyi) for support and guidance through all the stages of working on this research project. To my lab mate Precious- Thank you for all the laughs and memories. I would like to also thank my mother and siblings for the endless love, prayers and sacrifices. I would like to thank Prof. Harris for the XRD analysis.

Finally, I would like to thank God for giving me the necessary opportunity, strength, ability and knowledge to complete this research.

LIST OF ABBREVIATIONS

HMIs- Heavy metal ions

Hg- Mercury

Cr- Chromium

NPs- Nanoparticles

GO- graphene oxide

RGO- Reduced graphene oxide

CuO- Copper oxide

CuS-Copper sulfide

Au- Gold

UV-VIS- Ultraviolet - visible spectroscopy

FTIR- Fourier transform infrared spectroscopy

TEM- Transmission electron microscopy

EDX- Energy-dispersive X-ray

XRD- X-ray diffraction pattern

Eg- Bandgap

CV- Cyclic voltammetry

ASV-Anodic stripping voltammetry

GCE-Glass carbon electrode

ΔEp - Change in peak potential

Epa - Anodic peak potential

Epc - Cathodic peak potential

ipc - Cathodic peak current

ipa - Anodic peak current

Rct - Charge transfer resistance

LOD- Limit of detection

dH_2O – Distilled water

LIST OF FIGURES

LIST OF TABLES

TABLE OF CONTENT

CHAPTER 1

INTRODUCTION

1.1. Background

The pollution of natural streams by anthropogenically released heavy metals (HMs) is a worldwide problem. The primary causes of contamination in their discharge are wastewater, household effluents, and industrial operations. Moreover, HMs can also be released into the environment by other natural processes such rainfall, weathering, and soil and rock erosion [1, 2]. The primary concerns are the inherent challenges of biomagnification, which may arise at multiple levels in the biological food chain, and the possible toxicity that an excess of heavy metals may bring to plants and wildlife. As a result, both humans and animals may have severe health issues [3].

Heavy metals are biologically persistent and non-biodegradable pollutants that can accumulate for years or even decades in a variety of bodily organs. Heavy metals can have both positive and negative effects on human health. Their effects on living systems depend on their concentration and duration of exposure. Many heavy metals, including nickel (Ni), thallium (Tl), arsenic (As), mercury (Hg), lead (Pb), cobalt (Co), manganese (Mn), zinc (Zn), cadmium (Cd), and chromium (Cr), are extremely persistent and hence have a special significance in ecotoxicology [4]. World health organization (WHO) recommended limits for these heavy metals (Cr, Cd, Zn, Mn, Ni, Pb, and) to be as follows: Pb and Ni concentrations in drinking water are 0.05 mg/l, 0.003 mg/l, 3.0 mg/l, 0.4 mg/l, 0.07 mg/l and 0.01 mg/l respectively; in fish, they are 2.0 mg/kg [5].

It is known that heavy metals have an impact on biological system components and cellular organelles. These include the membrane of the cell, the mitochondria, the lysosome, the endoplasmic reticulum, the nucleus, and some of the enzymes that are involved in metabolism, detoxification, and damage repair [6]. The interaction between metal ions and nuclear proteins has been found to cause damage to the latter as well as conformational changes that may initiate cancer, apoptosis, or alter the cell cycle [7, 8].

Nanoparticles have recently been integrated with electrochemical sensors to form a very effective analytical method to detect heavy metals. Nanomaterials possess properties such as large surface area, strong adsorption ability and high conductivity which makes them a suitable potential material for electrode modification [9]. Functionalization reduces the NPs' tendency to aggregate and stabilizes their dispersion. Moreover, combining and hybridizing nanomaterials can increase their sensitivity and specificity and make them more appealing for use in sensing platform designs.

1.2. Problem statement

According to Rand Water, the quality of the river water reflects how water is being used within the community areas. It reflects the environmental awareness and attitudes of its users [10]. The quality of the water reflects what is done in a catchment area, because river runoffs are ultimately the results of human activity and lifestyle. South Africa is the world's biggest producer of chromite ore, which is the main source of the element chromium. The primary sources of mercury are fish and rocks in the earth's crust, although coal-fired power stations can also emit mercury into the atmosphere. It is also used by South African traditional health practitioners for health purposes [11]. According to the United States Environmental Protection Agency (EPA), heavy metals such as chromium, nickel, cadmium, copper, lead, mercury, and arsenic are classified as the most toxic. Heavy metals Heavy metals such as mercury, cadmium, lead and arsenic are known to be toxic even at lower concentrations (<0.05 mg/L) [12,13]. In contrast to copper, iron and zinc which are known to be toxic only at higher concentrations (>0.05 mg/L) [12, 13]. Ingestion of these toxic HMs can lead to diverse health issues. Therefore, it is of great significant that they become detected in water and food samples before consumption.

Different techniques have previously been employed for the detection of heavy metals in water. Spectroscopic techniques such as fluorescent chemosensor [14], atomic absorption spectroscopy (AAS) [15] and inductively coupled plasma mass spectroscopy (ICP-MS) [16] have also been used in the past for the detection of heavy metals. Though they have advantages such as high detection limit, high sensitivity and versatility, they also have several drawbacks like high cost, highly sophisticated and numerous steps.

Several studies were conducted to find an alternative detection method for heavy metals [17, 18]. Electrochemical sensors have been identified as an alternative route to detect heavy metals. This is due to their exceptional vantages such as low cost, simplicity, sensitivity, and its user friendly.

1.3. Motivation of the study

Water contamination has become a global environmental issue. With the rapid growth of industrialization, clean water has become very scarce. Inorganic and organic effluents, acid mine drainage, industrial wastewater and sewage are among the most common sources of water pollutants. Various heavy metals are found in water and are poisonous to human health. Different techniques have been employed to detect heavy metals such as chromium, mercury, lead, arsenic, etc., in water. It has been demonstrated that using electrochemical sensors instead of spectroscopic methods is a more efficient way to identify heavy metals in water. Electron mediators can be used to chemically modify the electrode surface of the electrochemical sensors. Suitable materials are required for the electrode surface modification. Thermal, mechanical, vibrational, electrical, and optical characteristics are known to be present in carbon-based materials such graphene oxide [19, 20]. Graphene oxide is known to be less stable and soluble. However, reducing it tends to enhance its stability and solubility [21]. On the other hand, nanoparticles help to improve the detection of toxic metals and the efficiency of photochemical reactions in water [21]. Infusing conductive RGO with copper sulfide (CuS), copper oxide (CuO), gold/copper sulfide (Au/CuS), and gold/copper oxide (Au/CuO) nanomaterials will improve the selectivity of the desired molecules and enhance both their specific surface area and catalytic activity. Nanostructuring the electrodes with metallic nanoparticles can lead to fast electrode kinetics, large surface area, high conductivity, and high catalytic activity. Modified sensors also show a high degree of functionalization and size dependent properties [22].

This project seeks to produce a stable sensor using screen printed electrodes modified by copper (Cu)-based nanomaterials, i.e., copper oxide (CuO), copper sulfide (CuS), gold/copper oxide (Au/CuO) and gold/copper sulfide (Au/CuS), incorporated into reduced graphene oxide (RGO). The developed sensor will then be used in the detection of

chromium and mercury. This project is driven by the need to produce a sensitive, low cost, reproducible and point-of-care electrochemical sensor for detecting chromium and mercury.

1.4. Aims and objectives

1.4.1. Aim

The aim of the study is to fabricate an RGO/Cu-based nanocomposites electrochemical sensor for the detection of chromium and mercury in water**.**

1.4.2 Objectives

The objectives of this study are set as follows:

i) synthesise and characterize graphene oxide (GO)

ii) synthesise and characterize Cu-based nanomaterials (CuO, CuS, Au/CuS and Au/CuO)

iii) incorporate Cu-based nanomaterials in RGO

iv) modify screen-printed electrodes (SPEs) using the as-synthesized Cu-based nanomaterials incorporated in GO

v) detect chromium(VI) and mercury(II)

1.4. Study outline

This dissertation is presented in 6 chapters.

- Chapter 2 provides a detailed assessment of the literature, covering all sorts of nanomaterials and various methods used to prepare them. There is also a discussion on various heavy metals found in water and electrochemical techniques employed to analyze and detect different water contaminants.

- Chapter 3 presents different characterization techniques and their principles used for this study

- Chapter 4 highlights the experimental procedures used to prepare and incorporate Cu-based nanomaterials in RGO. This chapter also includes the list of materials used.

- Chapter 5 explores the characterization of Cu-based nanomaterials in RGO using techniques mentioned in chapter 3. A detailed discussion with regard to shape and size of the materials is also given.

- Chapter 6 outlines the electrochemical properties of the different modified electrodes. Also discuss the stability of the fabricated sensor along with its sensitivity towards detecting Cr(III) and Hg(II)

REFERENCES

1. Ariño, C. et al. (2017) 'Voltammetric determination of metal ions beyond mercury electrodes. A review,' Analytica Chimica Acta, 990, pp. 11-53.
2. Tchounwou, P.B. et al. (2012) 'Heavy metal toxicity and the environment,' in EXS, pp. 133-164.
3. Khanna, P., 2011. Assessment of heavy metal contamination in different vegetables grown in and around urban areas. Research journal of environmental toxicology, 5(3), p. 162.
4. Cotruvo, J.A. (2017) '2017 WHO Guidelines for Drinking Water Quality: First addendum to the fourth Edition,' Journal AWWA, 109(7), pp. 44-51.
5. Storelli, M.M. et al. (2005) Trace elements in loggerhead turtles (Caretta caretta) from the eastern Mediterranean Sea: overview and evaluation. Environmental pollution, 135(1), pp. 163-170.
6. Wang, S. and Shi, X. (2001) 'Molecular mechanisms of metal toxicity and carcinogenesis,' in Springer eBooks, pp. 3-9.
7. Chang, L.W. et al. (1996) Toxicology of metals.

8. Beyersmann, D. and Hartwig, A. (2008) ‘Carcinogenic metal compounds: recent insight into molecular and cellular mechanisms,’ Archives of Toxicology, 82(8), pp. 493-512.
9. Pandey, P.N. et al. (2007) ‘Application of thiolated gold nanoparticles for the enhancement of glucose oxidase activity,’ Langmuir, 23(6), pp. 3333-3337.
10. Rand water (2022) Drinking water quality info sheets. Available at: https://www.randwater.co.za/drinkingwaterquality.php (Accessed: 4 June 2022).
11. Street, R. et al. (2015) ‘Metallic mercury use by South African traditional health practitioners: perceptions and practices,’ Environmental Health, 14(1).
12. Griffiths, C. et al. (2012) ‘US Environmental Protection Agency evaluation of surface water quality improvements,’ Rev.Environ. Econ. Pol, 6, p. 1.
13. World Health Organization, Guidelines for drinking-water quality: recommendations, World Health Organization, 2014.
14. Zhang, J.F. et al. (2011) ‘A pellet-type optical nanomaterial of silica-based naphthalimide-DPA-Cu(ii) complexes: recyclable fluorescence detection of pyrophosphate,’ Chemical Communications, 47(12), p. 3568.
15. Gonzales, A. et al. (2009) ‘Peat as a natural solid-phase for copper preconcentration and determination in a multicommuted flow system coupled to flame atomic absorption spectrometry,’ Analytica Chimica Acta, 636(2), pp. 198-204.
16. Liu, Y. et al. (2005) ‘Nanometer titanium di oxide immobilized on silica gel as sorbent for preconcentration of metal ions prior to their determination by inductively coupled plasma atom ice mission spectrometry,’ Talanta, 68(1), pp. 25-30.
17. Zhang, Q.X. et al. (2015) ‘Interesting inter-ference evidences of electrochemical detection of Zn(II), Cd(II) and Pb(II) on three different morphologies of MnO_2 nanocrystals,’ J Electroanal Chem, 739, pp. 89-96.
18. Zhu, C. et al. (2015) ‘Electrochemical sensors and biosensors based on nanomaterials and nanostructures,’ Anal Chem, 87, pp. 230-249.

19. Arshad, F. et al. (2018) ‘Polyethylenimine modified graphene oxide hydrogel composite as an efficient adsorbent for heavy metal ions,’ Separat. Purif. Technol, 209, pp. 870-880.
20. Abedalkader, A. et al. (2020) ‘Synthesis of graphene oxides particle of high oxidation degree using a modified Hummers method,’ Ceramic internationals, 15(46), pp. 23997-24007.
21. Konis, D. et al. (2014)’Dispersion behaviour of graphene oxide and reduced graphene oxide,’ Journal of colloid and interface science, 4309, pp. 108-112.
22. Kenmpahanumakkagari, S. et al. 2017) ‘Nanomaterial-based electrochemical sensors for arsenic-A review,’ Biosens. Bioelectron, 95, pp. 106-116.

CHAPTER 2

LITERATURE REVIEW

2.1. Introduction

The chapter offers a thorough explanation of all aspects of the study's design and procedures. Overall, this chapter provides the literature relevant to the research question or aim.

2.2. Nanotechnology

Nanotechnology is the science that involves the preparation of particles or materials at a nanoscale of 1 to 100 nm as defined by the national nanotechnology initiative or NSF [1]. Nanotechnology has infiltrated all sectors due to its unique and evident impacts, which give the scientific community numerous breakthroughs in the medical, agricultural, and other domains. It also has an enormous potential to revolutionize a broad variety of instruments and processes in health and biotechnology and enhance their personalization, usability, cost efficiency, reliability, and ease of administration [2].

Altering the morphology of the particles affects the surface chemistry, thus changing its surface-to-volume ratio and properties. This leads to particles with different antimicrobial effects, solubility and bioactivity compared to the larger materials of the same composition. Over the past decades, nanoscale particles have attracted a lot of attention due to their remarkable electrical, optical, and magnetic properties [3]. Their infinite size gives them more significant surface areas, higher reactivity, and a tuneable nature of several properties than their respective bulk materials [4-6]. These various distinctive properties have stimulated the growth of nanoscience and the application of nanoparticles (NPs) in a wide range of fields such as biomedicine, cosmetics, electronics, analysis food, environmental and remediation, or paints [7-11].

2.3. Nanoparticles

NPs are wide class of materials that include particulate substances, which have one dimension less than 100 nm at least [12]. Depending on the overall shape these materials

can be 0D, 1D, 2D or 3D [13]. The importance of these materials realized when researchers found that size can influence the physiochemical properties of a substance e.g., the optical properties. Based on their dimensions, composition, and material characteristics, nanoparticles can be categorized into a wide range of categories. There exist classifications that differentiate between inorganic and organic nanoparticles; the former includes fullerenes, quantum dots, and gold nanoparticles, while the latter includes dendrimers, liposomes, and polymeric nanoparticles. Alternatively, nanoparticles might be classified as carbon-based, ceramic, semiconducting, or polymeric. Furthermore, there are two categories for nanoparticles: hard (such fullerenes, silica particles, and titania [titanium dioxide]) and soft (like liposomes, vesicles, and nanodroplets).

2.3.1. Metal nanoparticles

Due to their optical characteristics, such as surface plasmon resonance (SPR) and the capacity to modulate optical field, metal nanoparticles such as those made of gold, silver, copper, etc., are very interesting, and could find use in a wide range of applications. The advantage of small size of metal nanoparticles facilitates them to penetrate through the biological or physiological membrane that is usually impermeable to other macromolecules [14, 15].

2.3.1.1. Gold nanoparticles (AuNPs)

Gold nanoparticles (AuNPs) have been used since ancient times to make stained glass, but it was long assumed that the colour of the gold suspension was a result of the chemicals used to prepare it. It has been discovered and reported that the colors of the gold nanoparticles depend on their sizes and shapes [16].

AuNPs have been researched for their wide variety of applications in different fields such as optics, electronics, energy and medicine. Their application in medicine includes ultra-sensitive biomarkers [17], localized heat therapy [18], contrast agents [19]. AuNPs are also suitable candidates to function as drug delivery vectors [18] due to their ability to link with multiple functional groups, for allowance of target drug delivery. The large surface area to volume renders them especially suitable for this task, also absorption of light by the plasmon of AuNPs can be used to initiate heat-sensitive release of medical

compounds. The plasmonics of the gold nanoparticles also allow for localized heat therapy by the absorption of light of specific wavelengths. The energy absorbed is later dissipated to the surrounding area. This technique has been shown to be highly efficient in conjunction with heat-sensitive release of anti-carcinogens as a method of fighting cancer tumour.

AuNPs could be categorized depending on the shape, size, and physical properties. The first reported shape in the field of AuNPs was spherical, although they were not exactly spherical. Later, various other forms were obtained, such as nanorods, nanoshells, and nanocages (Figure 2.1).

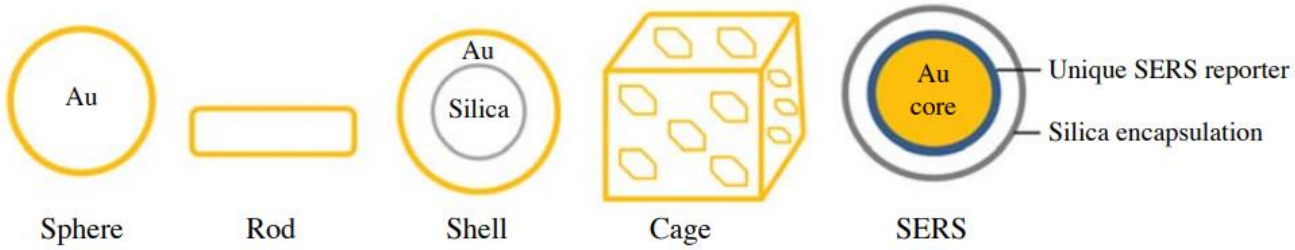

Figure 2. 1. Various shapes of Au nanoparticles [20].

2.3.1.2. Silver nanoparticles (AgNPs)

Silver has been utilized for thousands of years because it possesses antimicrobial properties. Because silver is non-toxic to humans and possesses antimicrobial properties, it is preferred as a nanoparticle. Antibacterial activity refers to the destruction or inhibition of bacterial growth without compromising the integrity of neighboring cells. Due to their environment-free nature, AgNPs are among the most alluring inorganic materials [21]. Additionally, it has numerous uses in a variety of industries, including photography, diagnostics, catalysis, biosensors, and antimicrobials [22, 23, 24, 25, 26].

Fundamental research over the last three decades has revealed that silver nanoparticles possess a unique combination of desirable features, including unusual optical qualities

associated with surface Plasmon resonance (SPR), well-developed surfaces, catalytic activity, and high electrical conductivity [27]. Ag NPs have been shown in studies to interact with heavy metals in aqueous solutions. Zuo et al. (2015), for example, demonstrated that AgNPs improved the removal capacity of bioavailable Cd from solution [28]. Silver nanoparticles are prepared using a variety of techniques, including physical, chemical, and biological. Physical and chemical techniques are typically deemed to be expensive and risky. However, the biologically produced nanoparticles exhibit good stability, high solubility, and high yield.

2.3.1.3. Copper nanoparticles

The eighth most common metallic element in the Earth's crust is copper (Cu), which is neither made nor destroyed after it has been solubilized from the crust. As a result, homeostatic regulation of copper is tightly controlled [29]. With the atomic number of 29, a mass of 63.546u, and a density of more than 5 g/cm^3, copper (Cu) is a transition metal with a distinctive reddish-orange hue and metallic shine. It possesses several intriguing characteristics, such as strong ductility, malleability, high thermal and electrical conductivity, great resistance to corrosion, minimal chemical reactivity, etc. [30,31].

Copper particles have a propensity to oxidize when exposed to air, which causes aggregation of particles due to surface oxidation, making the manufacture of copper nanoparticles far more challenging than that of noble metals. CuNPs are created in an environment with inert gas to avoid this issue [32]. Surfactants [33] or protective polymers [34, 35] may be used in certain cases to avert oxidation. Physical, chemical, and biological processes can all be used to create a wide variety of copper nanoparticles.

2.3.2. Metal chalcogenides nanoparticles

Metal chalcogenides or semiconductor nanomaterials have properties halfway between metals and nonmetals, giving them a wide range of applications as reported in the literature [36]. Due to the huge bandgaps of semiconductor NPs, bandgap tuning resulted in significant changes in their properties. As a result, they are deemed significant and advantageous in applications such as photocatalysis, photo optics, and electronic devices. Due to their optimal bandgap and band edge positions, several semiconductor

NPs are particularly efficient in water splitting applications [37, 38]. Below is the literature review of the selected metal chalcogenides nanomaterials.

2.3.2.1. Copper sulfides materials

Narrow band gap copper sulfide (CuS) nanoparticles exhibit at least different, but stable phases with different Cu:S molar ratios. These phases include covellite (CuS), anilite ($Cu_{1.75}S$), digenite ($Cu_{1.8}S$), djurlite ($Cu_{1.95}S$), and chalcocite (Cu_2S) [39]. Covellite (CuS) has garnered a lot of attention lately due to its exceptional concentration of free carriers within the copper sulfide class. The copper-to-sulfur phase CuS has the lowest Cu to S ratio among thermally and air-stable phases. Disulfide linkages are created in the covellite crystal lattice to maintain a balance between lattice site occupancy and coordination at this low Cu to S ratio. covellite's p-type metallic property originates from the ensuing electrical structure. The highest Cu to S ratio is seen in pure high chalcocite (Cu_2S). For $Cu_{2-x}S$ materials, the free holes originate from copper deficiency, hence at NIR wavelengths, Cu_2S (x=0) has few free carriers and no LSPR. Cu_2S can, however, change into the djurleite ($Cu_{1.97}S$) phase when exposed to air because it has enough open holes to display NIR LSPR [40].

Copper sulfide grows with 0-D (quantum dots) [41], 1-D (nanotubes [42]; nanowires [42, 43]; nanorods [44, 45]; nanoneedles [46]), 2-D (nanoplates [47]; nanoribbons [48]; nanodisks [49]; nanosheets [46, 50, 51]) and 3-D (nano-cubes [52], nanospheres [53-55], cages [56]. Copper sulfide (CuS) is a p type semiconductor with excellent optical and electrical properties, has been extensively studied for various applications [57-62]. CuS nanoparticles are gradually emerging as a promising platform for sensing [63], molecular imaging [64], photothermal therapy [65], drug delivery [66], as well as multifunctional agents that can integrate both imaging and therapy [67]. With a maximal absorbance at 900 nm, CuS nanoparticles exhibit an optical NIR range absorption band [68].

2.3.2.2. Cadmium sulfides nanoparticles

Cadmium sulfide nanoparticles have attracted a lot of attention due to their size-dependent characteristics. At normal temperature and pressure, the band gap energy of bulk CdS is 2.42 eV and it exhibits a hexagonal wurtzite-type structure [69]. Its melting

point is 1600˚C additionally. The phase of CdS nanoparticles changes from hexagonal wurtzite to the cubic phase of rock salt under extremely high pressure [70]. Due to size-dependent characteristics, 2.5 nm CdS crystallites were discovered to have a melting point as low as 400˚C and 0.7 nm CdS crystallites to have a band gap energy of 3.85 eV [71]. CdS nanocrystals have a wide range of morphologies, but the most common ones thus far have been flakes, spheres, dendrites, nanowires, nanorods, triangular, hexagonal, and sea urchin-like shapes [72, 73, 74, 75, 76]. Braun et al. (1999) described the synthesis of three different morphologies of hollow spheres, hexagonal pore arrays, and Cd^{+2} and H_2S nanoparticles using a lyotropic liquid crystal template [77]. However, Chen et al. (2006) have created novel hollow spheres of CdS nanoparticles with a nanoscale dimension [76].

2.3.2.3. Zinc selenide nanoparticles

According to Reiss et al. (2004), II-VI semiconductors are made up of an element from group 2 and an element from group 6 of the periodic table [78]. Usually, the atoms that make up a semiconductor's group II-VI bandgap (Eg) determine it. When the atoms that make up a semiconductor are heavier, the bandgap (Eg) will narrow. The quantum size effect will raise the bandgap in comparison to the bulk semiconductor for nanoparticles with diameters of roughly 2 to 10 nm. Additionally, it will result in a variety of bright colors reflecting minute variations in particle size [79]. ZnSe, one of the most significant II-VI group semiconductors, is a suitable choice for short-wavelength lasers and other optoelectronic devices including blue-green laser diodes and turnable mid-IR laser sources [80-81]. It has a room temperature bulk band gap of 2.7 eV.

The condition of the surface of the nanoparticles affects the quantum yield and emission lifetime of the band gap luminescence. It is discovered that the bare ZnSe nanoparticles as they are produced frequently exhibit surface flaws, which lead to non-radiative deactivation following stimulation. Additionally, because they aggregate quickly, these nanoparticles will have improper chemical interactions with one another [82].

2.3.2.4. Zinc oxide nanoparticles

The Zn atom in ZnO nanoparticles has an atomic number of 30 and is in the d-block of the periodic table, whereas the O atom is an atomic number 8 and is in the p-block. The ionicity of the II-VI compound semiconductor ZnO lies on the line between covalent and ionic semiconductors. Due to its extremely broad band gap (=3.3 eV at 300 K) and potential for use in optoelectronics, ZnO is attracting a lot of attention in research. Some of ZnO's optoelectronic uses are similar to those of GaN, another wide-gap semiconductor (= 3.4 eV at 300 K), which is frequently employed to create green, blue-ultraviolet, and white light-emitting devices. The availability of reasonably high-quality bulk ZnO single crystals and a significant exciton binding energy (=60 meV) are two advantages ZnO has over GaN. Additionally, ZnO has significantly simpler crystal-growth technology, which may reduce the price of ZnO-based electronics. Its effective piezoelectric property which is generally used in sensors, transducers, and actuators amongst others, has made it one of the most studied oxides in its nano-form in the modern era [83]. Due to its strong luminescence, ZnO has been proved to be a suitable material for phosphor applications [84]. Its high thermal conductivity also makes it useful as an additive in materials and products including plastics, rubbers, cement, and ointments. Furthermore, the ZnO radiation hardness is important for optoelectronic applications at high altitudes or even in space [85].

As schematically shown in Figure 2.2, ZnO is a group II-VI binary compound semiconductor that typically crystallizes in one of three forms: hexagonal wurtzite, cubic zincblende, or cubic rocksalt (or Rochelle salt).

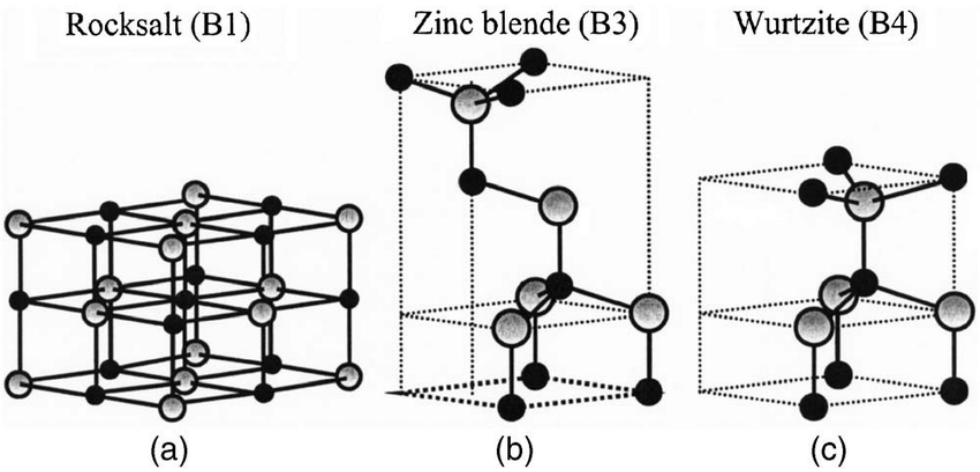

Figure 2. 2. Different crystal structures of ZnO [86].

2.3.2.5. Copper oxides nanomaterials

Copper Oxide (CuO) is the simplest member known in the family of copper related compounds. The material exhibits a range of potential physical properties, such as high temperature superconductivity, electron correlation effects, and spin dynamics [87, 88]. As a semiconducting compound with a monoclinic structure, CuO has attracted particular attentions in different technological fields, Examples include solar cell applications [89], active catalyst [90], gas sensor [91], high efficiency thermal conducting material [92], magnetic recording medium [93], and very good selectivity. It possesses useful photovoltaic and photoconductive properties. This is because crystal structures of copper oxide nanomaterials possess a narrow band gap [94]. Besides their properties, CuO NPs possess some novel characteristics that make them to be a centre of interest in researchers. CuO NPs are known to play a significant role in improving fluid viscosity and enhance thermal conductivity. It is these novel properties that render them a potentially useful energy-saving material that can improve the effect of energy conversion [95].

Due to their unique properties, CuO NPs have been applied in different areas, including gas sensors [96], catalysis [97], batteries [98], high temperature superconductors [99], and solar energy conversion [100], and field emission emitters [99]. For industrial catalysis, these nanomaterials may function as a replacement of noble metal catalysts for

carbon monoxide oxidation [101], which would reduce production cost and improve the catalytic efficiency. The suspension has excellent thermal conductivity and can be used as a heat transfer fluid in machine tools [102].

Copper nanoparticles are cost-effective as compared to other nanomaterials such as silver oxide, and can therefore be easily incorporated with polymers to successfully produce composites with unique chemical and physical properties. Due to their ability to reduce friction [103], and mend worn surfaces, CuO NPs are used as an additive in lubricants, polymers/plastics, and metallic coatings [104]. Moreover, the extremely high surface areas and unusual crystal morphologies provide them with antimicrobial activity, and they dose-dependently inhibit Escherichia coli strains, but not Salmonella typhimurium [105]. This finding paves the way to develop a novel and specific antimicrobial agent [106, 107].

2.3.3. Carbon-based nanoparticles

Carbon nanomaterials including graphene, carbon nanotubes (CNTs), crystalline diamond, and diamond-like carbon have found a wide range of applications due to their excellent electrochemical properties. The polymorphs of carbon used as electrode materials for electrochemical sensing in recent years include graphene, CNTs, and diamond. In addition, the outstanding characteristics of carbon nanomaterials, such as their high conductivity, high surface-to-volume ratio, and high electron mobility at room temperature, have facilitated several developments in electrochemical sensors.

2.3.3.1. Graphene and its derivatives

Graphene and its derivatives have their own unique advantages and can be used in many domains. Graphene, which is a strong material, is a carbon allotrope denoting two-dimensional planar hexagonal network of honeycomb lattices composed of carbon atoms. The thickness of a graphene sheet is usually approximately 1 nm [108]. Graphene is known to be constituted of various interesting properties that made it to be a centre of attraction in the field of science. Some of the interesting properties that influenced researchers to focus on it are high thermal conductivity, high electric conductivity, high elasticity and flexibility, and other remarkable properties.

Reduced graphene oxide (RGO) is the form of GO that is processed by chemical, thermal, and other methods in order to reduce the oxygen content [109]. The reduced graphene oxide is an excellent support for nanocomposites since the high specific area allows distribution of the nanoparticles evenly. Furthermore, the structural defects of the RGO may contribute to higher dispersion of the nanoparticle composite. Ganesan et al. prepared CuO nanoparticles decorated on graphene oxide for cancer activity and catalytic applications [110].

2.3.3.2. Fullerenes

Symmetric nanocarbon structures are known as fullerene molecules [111]. In 1985, fullerene was found [112]. Polygones, or pentagons and hexagons, make up a fullerene molecule. The number of carbon atoms in a fullerene molecule's structure determines its name. C60 is a typical fullerene compound [113,114]. It is also known as Buckminsterfullerene. It bears the name of Buckminster, an American architect. With a diameter of 7.09 A, the fullerene C60 consists of 60 carbon atoms as depicted in Figure 2.3 below. The forms of fullerene molecules, which are composed of carbon atoms, include hollow spheres, ellipsoids, and tubes. Another name for spherical fullerenes is "bucky balls". Fullerenes' remarkable chemical characteristics are largely determined by their electronic structure [115]. Because each fullerene's carbon atom is connected to three nearby carbon atoms on a polyhedron's vertices, it creates two single bonds and one double bond [116]. The formation of fullerene molecules has been accomplished by a number of techniques, including CVD, laser ablation, and arc-discharge practice. Additionally, described are higher fullerene analogs, such as C70, C120, C185, C540, C720, and so on [117,118].

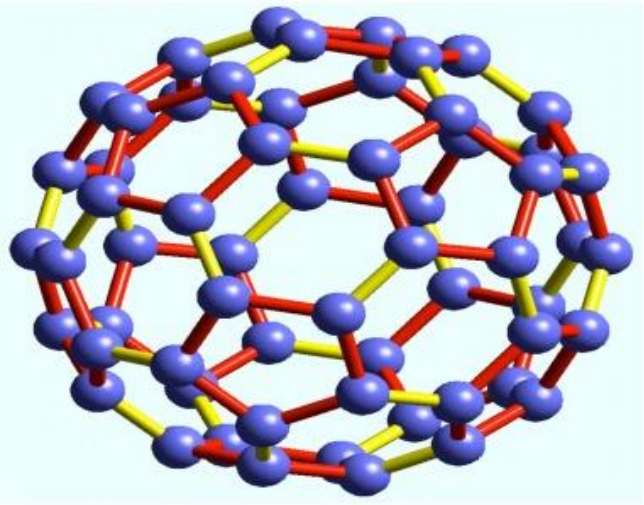

Figure 2. 3. The Buckminsterfullerene C60 Molecular Structure [119].

2.3.3.3. Carbon nanotubes

Carbon nanotube are a hollow carbon tube consisting of three adjacent carbon atoms that share a sp^2 covalent connection. The carbon atoms are arranged hexagonally inside the tube. The bond separation is roughly 1.44 A. CNTs can be several hundred microns long and have a typical diameter of 1-5 nm, which is 100,000 times thinner than an ordinary human hair. Along the CNT's axis, they can enable ballistic electron and hole movement by forming a closed, comparatively stable system.

Single-walled carbon nanotubes (SWCNTs) and multi-walled carbon nanotubes(MWCNTs) are the two different forms of carbon nanotubes (Figure 2.4). They have a layer of graphite that has a cylinder-shaped shape and measures 1 nm in diameter and 100 nm in length. These materials stand out due to their diminutive size and exceptional physical, mechanical, and electrical properties [120]. With an adjacent shell separation of roughly 0.34 nm, the nanotubes may be made up of one up to tens of thousands of concentric carbon shells [121]. Due to the sp^2 connections between the individual carbon atoms, carbon nanotubes are known for their increased tensile strength as well as their elasticity, which allows them to bend and buckle when subjected to strong compressive stresses and can still return to their initial structure [122].

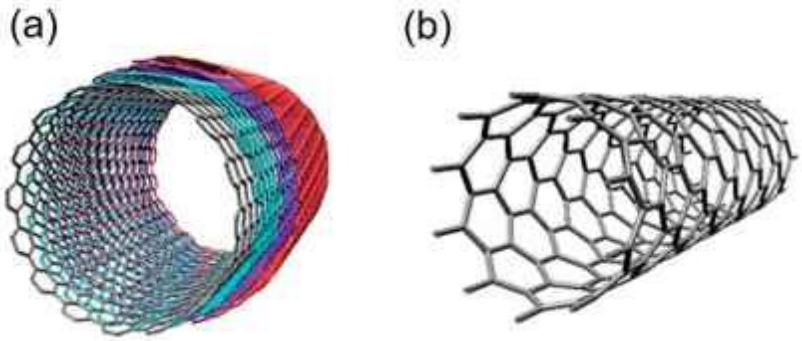

Figure 2. 4. Schematic diagram of (a) MWCNT and (b) SWCNT [123].

2.3.4. Fabrication techniques for metal, metal chalcogenides and carbon-based nanoparticles

Techniques for synthesizing metal sulfides or oxides nanoparticles generally rely on the same techniques that have been used to prepare metal nanoparticles. Different methods have also been developed in the past few decades for synthesizing carbon-based nanoparticles.

2.3.4.1. Techniques for synthesizing metal nanoparticles

Techniques for synthesizing metal nanoparticles are based either on “bottom-up” (in which atomic-level precursors are used to synthesize nanosized materials) or “top-down” (in which a bulk solid is broken down into progressively smaller components), as can be seen in Figure 2.5. Employing a bottom-up approach affords the use of many various techniques such as chemical vapour deposition, sol-gel processes, spray pyrolysis, laser pyrolysis, and molecular condensation. The use of these methods allows the morphological parameters of nanoparticles to be manipulated by various parameters such as concentrations of reagents and reaction conditions. As for the top-down route, nanomaterials are prepared through diverse range of synthesis approaches like lithographic techniques, ball milling, etching, and sputtering [124].

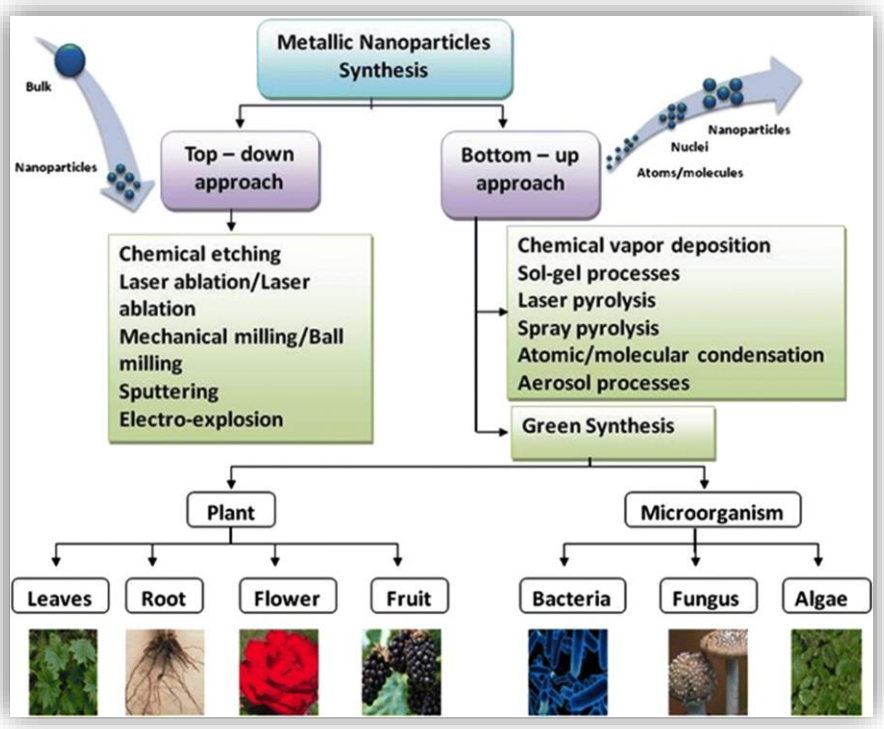

Figure 2. 5. Various synthesis techniques for the preparation of metal nanoparticles [125].

Although both synthetic techniques have their advantages and drawbacks, the bottom-up approach has received much attention due to its ability of offering greater scope for controlling the size and shape of the resulting nanoparticles. One of the bottom-up approach reported the most by various researchers in the synthesis of metal nanoparticles such as gold (Au), silver (Ag) or copper (Cu) NPs often entails the reduction of Au(III), Ag(I), Cu(I) or Cu (II) sources [126].

2.3.4.2. Techniques for synthesizing metal sulfides or oxides nanoparticles

The synthesis of metal or metal chalcogenides NPs essentially centres on mainly four chemical reaction types, namely, (1) reduction, (2) hydrolysis, (3) condensation, and (4) oxidation. Depending on the choice of final materials, either one or a combination of afore mentioned chemistries can be applied. However, the growth of research has prompted researchers to develop more techniques for synthesizing metal chalcogenides

nanoparticles. Some researchers reported on the advantages of using chemical co-precipitation, and selected it as the most unique and simplest method for the synthesis of metal chalcogenide NPs. Some of the advantages over other synthetic techniques are easy controllability over the particle size, low-cost, and requires lower temperatures. However, it was also indicated that its biggest challenge is agglomeration. But employing stabilizers or capping agents, one is able to avoid agglomeration.

Besides co-precipitation method for the synthesis of metal chalcogenides nanoparticles, there are several methods that have been employed before. The synthesis of metal chalcogenides, for example, copper-based nanomaterials (CuO/CuS NPs), on the other hand, basically requires hydrolysis of the precursors followed by a dehydration process leading to the final product. Additionally, an oxidation process (sometimes unavoidable for Cu-based NPs) can be deployed for the preparation of these Cu-based NPs with higher oxidation numbers from their respective precursors of lower oxidation states. In synthetic processes, the techniques that are applied provide a suitable environment and energy to facilitate the process of choice while additional constraints are imposed to modulate the stability, properties, and morphology of the final NPs. The methods for synthesizing Cu-based nanomaterials can be classified into five major categories (Figure 2.6).

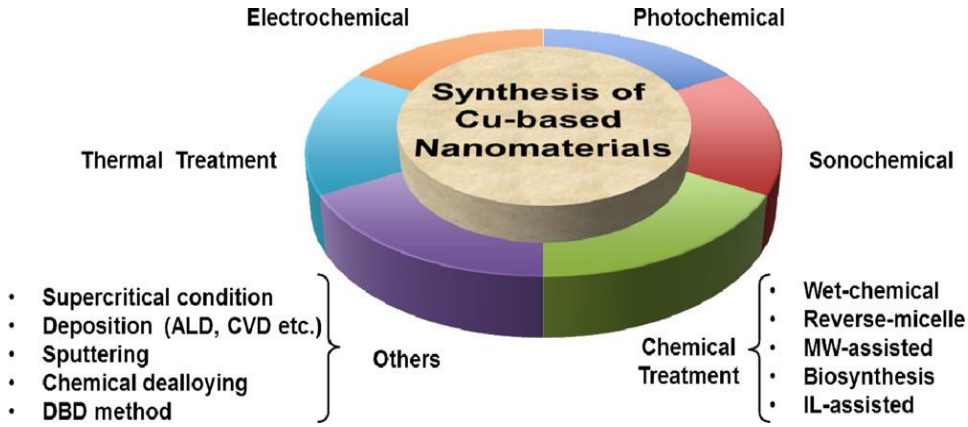

Figure 2. 6. Different methods for the preparation of Cu-based nanomaterials [127].

Among these, the most popular procedure is based on “chemical treatment”, and some of the most modern methods could be regarded as an extension of this protocol providing advantages in terms of shape and/or size selectivity.

2.3.4.2. Techniques for synthesizing carbon-based nanoparticles

Various methods have been used to prepare or produce carbon-based nanomaterials. The development of advanced components with improved performance and multifunctionality made from next-generation nano-carbon composites has drawn attention. Precursors made of carbon, such as graphene and CNTs, are essential for determining whether the technology will remain viable in the long run. Acetylene, methane, benzene, toluene, and xylene are only a few of the carbon precursors that have been used to create CNTs thus far [128,129]. The most common techniques for creating carbon nanotubes are gas-phase catalytic growth [130], chemical vapor deposition (CVD) [131], arc discharge [132], and laser ablation [133].

Graphene oxide (GO) it is an oxidized form of graphene. Its properties were discovered first by a British chemist Benjamin Brodie in 1859 before the discovery of graphene [134]. He prepared graphene oxide by mixing 1:3 ratio of graphite and pottasium chloritate ($KClO_3$) together and then react the mixture with nitric acid in the duration of 3 or 4 days [135]. The method involved the use of very strong acids and potassium chlorate. The method was then improved by L.Staundenmaier who used two-third of nitric acid (HNO_3) to sulphuric acid (H_2SO_4) [136]. However, the method caused explosions upon the addition of potassium chlorate ($KClO_3$) [136]. In 1958, chemist hummer and offeman introduced their method (figure 1) which became the most popular method for the synthesis of graphene oxide. Their method requires less time than the previous methods and provides a good yield. In their method they replaced potassium chlorate ($KClO_3$) with potassium permanganate ($KMnO_4$) and nitric acid (HNO_3) with sodium nitrate ($NaNO_3$). These changes eliminated the fog acid produced by the fuming HNO_3. The oxygen produced by the Hummers’ method was more that the oxygen produced by Brodie’s method [137].

Reduction of GO consist of three processes: 1) oxidation 2) exfoliation and 3) reduction. RGO can be prepared using a strong reducing agent, such as hydrazine hydrate (NaBH4). But it's very non-eco-friendly and it decreases the sensor performance. So, to eliminate these adverse effects, an eco-friendly reducing agent such as ascorbic acid can be used instead [138]. This reaction does not produce toxic gases [139].

2.3.5. Applications of nanoparticles

2.3.5.1. Carbon based nanomaterials

graphene and its composites offer distinct benefits with a variety of applications and methods, including solution dispersion, thermal decomposition, vacuum filtration, spin coating, thermal chemical vapor deposition (CVD), and chemical decomposition polymer processing [140-146]. RGO has shown to be a strong contender for a number of uses, including the creation of composite paper-like materials, solar cells, field effect transistors (FET), and energy applications. The potential of carbon nanotubes has been noted in a number of applications, including biological applications [147], water filtration membranes [148], catalyst supports [149], energy storage devices [150], field emission devices [151], thermal conductors [152], thermal interface materials [153], and more. Due to the special physical and chemical characteristics of fullerenes, numerous researchers are investigating the potential uses of this molecule and its functionalized derivatives in a variety of fields, including photovoltaics [154], medicine [155], gas adsorption/storage [156], and pharmaceuticals [157], to name a few.

2.3.5.2. Metal Chalcogenides

Chalcogenide nanocrystals find use in a wide range of applications, such as biomedical devices, storage devices, detectors, emissive materials, sensors, and energy harvesting thermoelectric devices. The uses of compound copper chalcogenide nanocrystals are among the most extensively studied and acknowledged among the several types of nanocrystals. Their compositional and structural diversity is the reason for this. In property development, their band shape and defect concentration are crucial [158]. Cui et al.'s study described the synthesis of many copper-based chalcogenide nanocrystals for increased solar energy harvesting via near-infrared plasmonics. Research revealed that

Cu7S4@Pd had significant near-infrared absorption plasmonic absorption, which provided a heat carrier from Cu7S4 to Pd and caused catalytic processes on the surface of Pd [159].

2.3.5.3. Semiconductor

Semiconductor nanostructures exhibit intriguing physical and chemical characteristics as well as practical capabilities in comparison to their typical bulk equivalents and molecular materials. Among the most appealing characteristics of these materials are their processability, surface functionality, strong chemical and photobleaching stability, continuous absorption bands, narrow and intense emission spectra, and surface functionality. Numerous studies on the fabrication of semiconductor nanoparticles show how "nanochemistry" has evolved [160]. To adjust their qualities for various applications of interest, one can alter parameters including surface, shape, and size characteristics [161]. Research and applications in emerging technologies, including miniaturized sensors and imaging devices, energy conversion, non-linear optics, nanoelectronics, nanophotonics, solar cells, catalysis, detectors, photography, biomedicine, and others, have been greatly influenced by these unique properties of semiconductor nanomaterials. Semiconductor materials have distinct photophysical characteristics including photoluminescence and changes in the absorption range [162]. These characteristics result from quantum effects generated by specific semiconductor materials' band structure confinement and band edge feature tuning [163].

2.3.6. Cu-based nanomaterials supported on graphene.

Numerous carbon-based materials are being investigated as supports for Cu-based nanomaterials due to recent developments in the application of metal-embedded carbon networks, particularly in electrocatalysis. Because of their intriguing physical and chemical characteristics, such as their high surface area, high conductivity, multiple surface functionalization options, and their inherent ability to incorporate guest materials due to their special hollow geometry, carbon nanotubes (CNTs) stand out among carbon support materials [164-166].

Due to its exceptionally high surface area (about 2600 m2/g), strong thermal and electrical conductivity, and chemical durability, graphene has long been known to be a desirable catalyst support. Many techniques have been used to create graphene-supported Cu based NPs, but they usually entail combining a graphene oxide solution with a Cu salt and reducing them together [167]. The reduced graphene oxide is an excellent support for nanocomposites since the high specific area allows distribution of the nanoparticles evenly. Furthermore, the structural defects of the RGO may contribute to higher dispersion of the nanoparticle composite.

2.4. Heavy metals in water

Heavy metals are the most prevalent kind of pollution when it comes to environmental monitoring factors. They originate from the chemical leaching of bedrock, water drainage, and the discharge of waste waters from urban, industrial, and rural sources [168]. In general, they are not biodegradable and they have long biological half-lives hence they tend to bioaccumulate in higher trophic levels of the food chain yet they may be toxic even in trace quantities [169-173]. Our waterways are becoming more contaminated with trace metals, particularly heavy metals, which is a result of rising industrialization and urbanization [174].

Heavy metals have a discernible effect on aquatic flora and fauna, which via biomagnification enters the food chain and eventually impacts people as well [175]. Mercury, lead, cadmium, and arsenic are four heavy metals that have been classified by the World Health Organization as being among the ten chemical substances that seriously endanger human health [176,177,178]. Trace amounts of metals are typically necessary for biological processes in cells, including signaling and transportation [179]. Metals play a vital role in cellular processes, but their concentration range has a significant effect on human health. If the range of metal concentration is less than the range of toxicity, it is considered safe. It has different physiological and cytological consequences when it exceeds the allowable limits [180].

2.4.1. Lead

Lead (Pb) is a well-known water contaminant and is utilized extensively in industry. The automotive industry, which needs large amounts of lead (Pb) for the production of batteries, as well as mining and the processing of lead ores are the most significant anthropogenic environmental sources of exposure to lead compounds [181]. Exposure to lead has been associated with several illnesses and can alter the physiological activities of the body [182]. It is extremely toxic and negatively impacts the body's neurological, biochemical, and cognitive systems. Constipationtion, stomach pain, gastrointestinal issues, and impacts on the central nervous system are linked to it [183]. The two most typical ways that lead enters animals are by ingestion and inhalation.

The harmful impacts of lead exposure on health are widely recognized. These in children include behavioral issues at low Pb levels, developmental delays, seizures, and in rare instances, very high Pb-related mortality [184]. The level of concern for lead poisoning in blood around the globe is 10µg/dl [185]. Despite having numerous negative consequences on the body, lead is known to have no physiological purpose. Because lead binds to the sophydryl (SH) group, it may inhibit some proteins [186]. Blood lead levels and MAD levels in erythrocytes are correlated, according to a study on lead-exposed workers. Lead-exposed workers' blood lead levels and MAD levels in erythrocytes are connected, according to a study. Glutathione reductase and glutathione S-transferase inhibition brought on by decreased glutathione production affects glutathione metabolism [187]. These enzymes raise ALA concentrations and oxidize hemoglobin [188]. It competes with calcium at the molecular level and inhibits the hemo-biosynthetic pathway, resulting in hematological consequences [189]. When a child's blood level exceeds 10 µg/dl, treatment should be considered. Adults don't experience symptoms until their blood level rises above 80 µg/dl. However, children with a level of 45 µg/dl typically require medical attention [190]. According to the ATSDR (1999), a child's mental retardation or behavioral and cognitive issues may result at a significantly lower level of 30 µg/dl [191].

Various organizations have set acceptable levels for lead in drinking water. For example, the American Academy of Pediatrics defines lead poisoning as having a lead level of

more than 10 µg/l. However, according to KEBS and WHO, the most amount of lead that can be present in drinking water is 0.1 mg/l [192,193,194,195].

2.4.2. Mercury

Mercury, or Hg, is a metallic element that is liquid at normal pressure and temperature, and is one of the basic natural elements that comprise the composition of Earth. Mercury is referred to as a "heavy metal" due to its high density of 13.534 g·cm-3 at STP. In addition to various human activities, natural processes such as volcanic eruptions, geothermal activity, and mineral deposit degradation release mercury into the atmosphere. The third type of mercury source is re-emission. Amounts of mercury released or re-emitted into the environment annually from all sources range from 5500 to 8900 tons, according to certain modern calculations of mercury flow through the environment [196]. Three kinds of mercury exist in the environment: elemental or metallic mercury (Hg^0), inorganic mercury (Hg^+, Hg^{2+}), and organic mercury (also known as methyl or ethyl mercury) [197]. Mercury can be found in air, water, and soil. Applications for mercury compounds in mining include the extraction of gold and several industrial processes. It has also been widely employed up to this point in fluorescent light tubes, dental amalgam, and thermometers.

Mercury exposure is harmful to human health. Mercury comes in several forms that can damage the kidneys, lungs, immune system, central and peripheral neurological systems, and if exposure levels are high enough, they can even be lethal [198, 199]. Methylmercury, or MeHg, is the type of mercury that poses the greatest risk to human health. MeHg consumption was the root cause of multiple large outbreaks. Neurological damage from chronic mercury toxicity includes ataxia, muscle weakness, numbness in the limbs, difficulty speaking, eating, and swallowing, as well as an enhanced tendon reflex in those exposed to high concentrations of Me-Hg [200]. The US Environmental Protection Agency (USEPA) has established a Maximum Contaminant Level (MCL) of 2 µg/L for mercury in drinking water. The USEPA has also established a land disposal limit (LDR) standard for wastewater treatment at 0.15 mg/L [201].

2.4.3. Cadmium

Cadmium (Cd) is another hazardous inorganic substance that is utilized in many different industries, including the plastic, painting, battery, and electroplating sectors. Even though it is uncommon, cadmium can be found naturally in water, soil, minerals, carbonate, hydroxide, and sulfide salts. Following industrial activity, there may be high quantities of cadmium (Cd) in the air, water, and soil. This could result in significant human exposure to Cd. Smokers are more likely than non-smokers to be exposed to this metal, which can lead to fatal lung conditions as well as severe lung damage. Long-term exposure to Cd can harm the kidneys, bones, and lungs, while short-term exposure can result in diarrhea [202].

One of the carcinogens that prevents the enzymes from fixing errors that lead to DNA mismatches is cadmium [203, 204]. It is well recognized that it is opposing to vital elements and a teratogen. Cadmium causes the most terrible type of cancer by inhibiting mismatch repair (MMR) [204, 205], which magnifies cellular errors and increases gene alterations. Difficulties with renal function brought on by exposure to cadmium (Cd) can also encourage the development of arterial hypertension. An increased risk of ischemic heart disease, acute coronary syndromes, and problems from arterial hypertension may ensue from this.

2.4.4. Arsenic

ArsenicO(As) is a dangerous and carcinogenic material [206, 207]. It is a naturally oc$_{cu}$rring element that can be found at a 5 mg/kg average concentration in the earth's crust [208]. Although there are man-made sources of arsenic, the main way that arsenic enters groundwater is through geological weathering. It is estimated that this natural discharge of arsenic into ground or surface water puts 140 million people in at least 70 nations at danger of arsenic poisoning [209]. Based on its origin and mode of mobilization, arsenic is divided into three primary exposure sources: geological, anthropogenic, and biological. More than 150 minerals include arsenic in conjunction with arsenopyrite or sulphide [210, 211]. There are four oxidation states of As in the natural environment: As(V), As(III), As(0), and As(-III). Arsenic is mostly found in

groundwater as As(III) and As(V), with trace amounts of methyl and dimethyl arsenic compounds also found there [212,213,214].

Exposure to As might come from the workplace or tainted food and water. It has the infamous names "king of poisons" and "poison of king" [215]. β1-integrin distribution was seen in a cutaneous toxicity investigation conducted with cultured human keratinocytes. Reduced integrin expression in keratin cytes may cause aberrant apoptosis and skin manifestations [216]. The highest allowable limit of arsenic in drinking water, according per BIS Standards (IS 10500: 2012), is 0.01 mg/l (ppm) or 10 µg/L (ppb).

2.4.5. Chromium

Chromium (Cr) is a transition metal mostly utilized in paints, pigments, alloys, and catalyst manufacturing processes. Both hexavalent (chromium(-6), Cr(VI), Cr^{+6}) and trivalent (chromium(-3), Cr(III), Cr^{+3}) chromium oxidation forms are frequently found in water distribution networks, natural environments, and water treatment processes. It has long been believed that humans require trivalent chromium as a vitamin. Though there is no established molecular mechanism for Cr(III) in cells, recent research has not demonstrated any harmful consequences from low Cr(III) in the diet, raising doubts about whether Cr(III) is actually a necessary nutrient [217].

Due to inhalation routes of exposure, hexavalent chromium is classified as a recognized human carcinogen by the USEPA (1998) and IARC (1990) [218]. Cr(VI) may raise the mortality and incidence of several malignancies in humans, such as those of the lung, throat, bladder, kidney, testicles, bone, and thyroid [219]. Cr(VI)-induced oxidative stress and high levels of ROS generation target the lipid and DNA content of cells, resulting in lipid peroxidation and DNA damage, respectively. Tumor growth and progression can result from medium to low level ROS generation in cells [220]. Pentavalent and tetravalent chromium are released when Cr(VI) is converted to Cr(III) during metabolic processes. Glutathione stabilizes these bi-products, which have a greater affinity for cell membranes [221]. Although this system aids in detoxifying, it is altered by continuous exposure, which results in the production of free radicals [222]. Lipid peroxidation damages the cell membrane as a result [223,224,225].

2.5. Techniques for detecting heavy metals

A metal ion detector is a tool used to find out whether metal ions are present in the environment. It can also be helpful to measure the amount of metal ions present. The development of strategic methods to render water bodies safe for human use is crucial given the health issues that the entire world is currently confronting. We must have a way to identify the presence of these harmful metal ions in water samples before we can remove them. This will enable us to choose the best removal approach and quantitatively assess the amount of pollution that is currently present. To do this, an accurate detection method that is both economical and time-efficient, as well as ecologically friendly, needs to be created. The sensitivity of the detection method should also be taken into consideration when selecting which one to use in order to simply and accurately detect even minute amounts of metal ions. A number of methods for identifying heavy metal ions have been reported and used in the last few decades. Some offer intriguing benefits, but because of their disadvantages, it has also been discovered that they are difficult to use. The methods listed below for identifying heavy metal ions (HMIs) have been documented in the literature [226].

2.5.1. Colorimetric Sensing

Colorimetry is a rapid and easy method for detecting heavy metal ions. A novel kind of Al^{3+} colorimetric probe was described: 5-mercaptomethyl tetrazole (MMT) was modified to act as a chelating ligand on the surface of gold nanoparticles (AuNPs), creating a mercaptomethyl gold nanoparticle (MMT-AUNP) probe. Color changes were caused by the aggregation of MMT-AuNPs caused by the addition of Al^{3+}. The probe's absorption spectra dropped at 520 nm and formed a new absorption peak at 620 nm when it was titrated with various quantities of aluminum ions. The solution's color also shifted from red to dark blue. (E)-1-(4-((4-(diethylamino)-2-hydroxybenzylidene)amino) phenyl)-3,4-diphenyl-1H-pyrrole-2,5-dione (BASB) is a novel synthetic Schiff base receptor that was employed as a colorimetry sensor for the selective detection of aluminum ions. When Al^{3+} was present, BASB's color changed from colorless to yellow, and this was explained by the BASB·Al^{3+} combination that formed. It was also demonstrated that the receptor

solution’s absorption spectra dropped at 373 nm and a new absorption peak developed at 425 nm with the ongoing addition of aluminum ions [227].

2.5.2. Optical sensing

The reflective or absorptive characteristics of a substance can be used to identify its optical effects. Numerous methods, such as indicator dyes, ionophores, optical fibers, capillary-type devices, integrated optics etc., are used to detect HMIs. These visual modalities do have certain drawbacks, though. Numerous optical sensors lack selectivity and are unable to identify multiple ionic species at once. This problem is particularly prevalent in indicators, which react with hydrogen atoms and require strict pH control through the use of masking agents. The basis for indicators is the binding of HMIs to the indicator dye, which modifies the indicator’s absorbance or fluorescence. As an indicator for the heavy metal ion in these sensors, which cannot be determined directly by visual means, it functions as a transducer. In a different class of indicators, the luminescence within the indicator dye is both statically and dynamically quenched by heavy metal ions, which function as "quenchers." When quenching happens dynamically, only the excited state of the fluorophore interacts with the quencher as opposed to the ground state in static quenching. There is a reversibility to the dynamic quenching process because the dye is not cooked. Improved sensitivity is one benefit of fluorescent indicators; however, many of them are non-selective and can bind to several metal ions. Some indicators have low stability, need additional reagents, are not readily available in pure form, which is required for sensing applications, and cannot be used for optical detection of heavy metal ions. Many indicators only bind at high or low pH values, or they bind irreversibly. The fundamental issue with indicator dye-based sensors is that they increase process complexity by requiring a distinct dye and analysis wavelength for each heavy metal ion. Ionophores have become more popular for heavy metal ion detection because of the drawbacks of indicator reagents. Ionophores can detect HMIs because of their capacity to bind with certain ions. Ionophores are frequently combined with chromogenic or fluorogenic components to combine optical output with the ionophore’s capacity to bind to specific ionsIn these instances, even though the chromo-ionophore is required to produce the visual signal, the heavy metal ion is recognized due to its selective interaction

with ionophores. Protons equal to the metal ion's charge evaporate from the chromo-ionophore during the ionophore-HMI interaction, changing the chromo-ionophore's color or fluorescence.
[228].

2.5.3. Electrochemical sensing

Electrochemical methods are dependable, affordable, and easy to utilize. In addition, these methods provide faster analytical and response time than spectroscopic methods. When compared to spectroscopic and optical techniques, these methods have larger limits of detection (LOD) and lesser sensitivity, which necessitates design alterations such switching to a different biosensing electrode or altering the electrode's composition. Though the sensitivity of electrochemical techniques may not be as high when compared to other techniques, the short response time and high ease of use are important advantages and may allow electrochemistry to be implemented in real systems. The fundamental idea behind electrochemical approaches is that the presence of HMIs or other ions alters the electrical signal and electrical characteristics (charge, current, impedance, voltage, etc.). Depending on the parameters that are impacted, these methods can be categorized as voltammetric, amperometric, potentiometric, etc. [228].

Amongst all the electrochemical techniques, voltammetry is the most widely used method for detecting heavy metal ions. Using voltammetric methods, a current-voltage curve is produced by measuring current at various applied potentials. The technique of voltammetry is widely employed in the detection of heavy metal ions due to its exceptional accuracy, low detection limit, and high sensitivity. Although voltammetry comes in a variety of forms, all of them follow the same basic process of measuring current by altering potential. In this investigation, heavy metal ion analysis was done using stripping voltammetry.

Ultimately, stripping voltammetry entails two primary stages: electrodeposition, which entails depositing the analyte solution from the well mixed solution onto the electrode, and the voltammetric step, which entails removing the analyte to enable analysis with any of the VM methodologies. Anodic potential scan and cathodic potential scan are two

additional categories for stripping voltammetry that are derived by using, respectively, anodic stripping voltammetry (ASV) and cathodic stripping voltammetry (CSV). Stripping voltammetry has a very low detection limit, makes it a great tool for downsizing, and only requires very basic, fairly priced instruments [229]. Zinc ions in acetate buffer were detected using anodic stripping voltammetry and a disposable copper-based electrochemical sensor. [230]. The Zn^{2+} concentration in blood serum could also be detected and measured by the sensor, in addition to its good sensitivity and reduced limit of detection. Figure 2.7 displays anodic stripping voltammograms at the different Zn^{2+} ion concentrations.

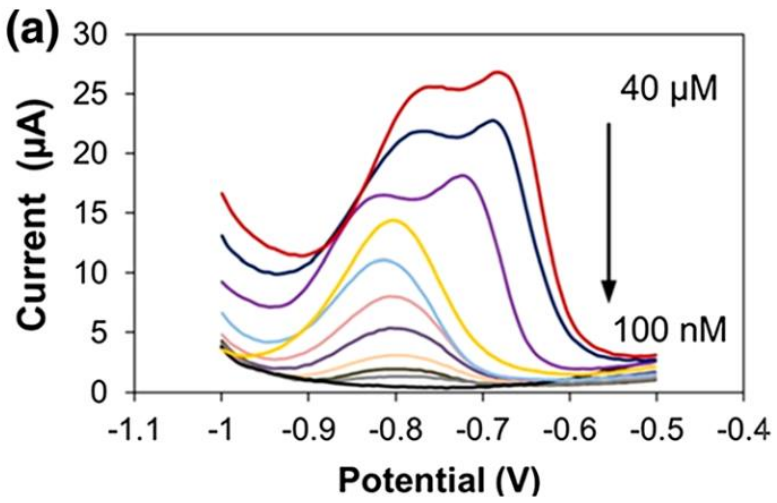

Figure 2. 7. Anodic stripping voltagram of Zn^{2+} samples in a range from 100 nM to 40 μM range [230].

2.5.4. Spectroscopic sensing

Atomic absorption spectroscopy (AAS), a highly sensitive method, is one of the spectroscopic techniques used to detect HMIs. Additional methods include capillary electrophoresis, UV/Vis spectroscopy, liquid chromatography, inductively coupled plasma optical emissions spectroscopy (ICP-MS), and X-ray fluorescence spectroscopy. Although these methods come with expensive equipment and require skilled workers to operate the sophisticated equipment, they are flexible enough to detect various HMI

concentrations for a wide variety of elements at the same time with very low detection limits. For instance, AAS can detect mercury ions much below the part per billion range. These techniques have been used to find copper, lead, and mercury ions at concentrations lower than parts per billion. But the disadvantages are beginning to exceed the benefits. Spectroscopic techniques necessitate intricate sample preparation and pre-concentration procedures, in addition to costly equipment and intricate operation procedures. Atomic spectroscopy techniques, such as using a certain wavelength to excite single atoms from their ground state to their excited state, are often used to measure the concentrations of HMIs. Sensitive concentrations of HMIs can be determined by measuring the energy absorbed during this excitation, which is proportionate to the concentration of various atoms present in the sample [228]. Below is a single-beam atomic spectrophotometer (Figure 2.8).

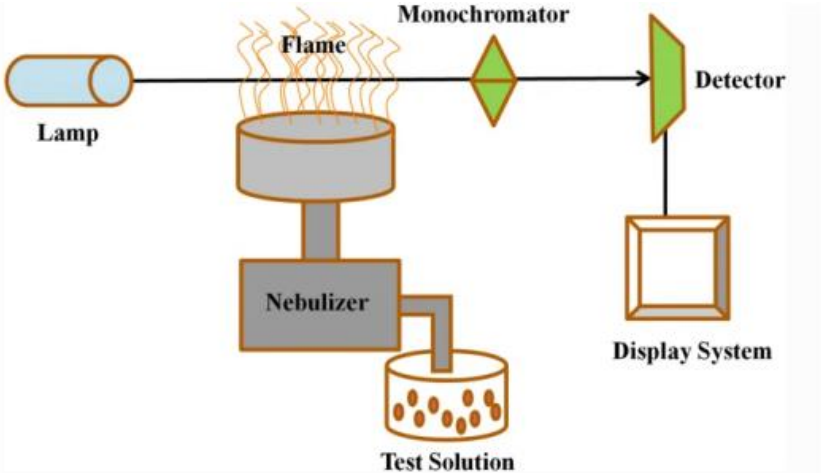

Figure 2. 8. Metal ion detection with a single-beam atomic absorption spectrophotometer. It is made up of an electronic "readout" device, a detector, a monochromator, an atomizer to produce gas-phase atoms or ions for examination, and a primary light source [228].

2.5.5. Fluorescent Sensing

A fluorescence system with two distinct fluorescent groups-one acting as an energy acceptor (A) and the other as an energy donor (D)-is necessary for the Fluorescence

Resonance Energy Transfer System (FRET). Non-radiative energy transfers from donor D to recipient A may happen when the fluorescence system is excited using donor D's excitation wavelength. The fluorescence of the system was extinguished after energy transfer if the fluorescence quantum yield of receptor A was zero, and the receptor's fluorescence was visible if it was also an emitter of fluorescence. The following are necessary for the production of FRET: (1) As seen in figure 2.9, there needs to be sufficient proximity between the energy donor and the acceptor; (2) there needs to be a specific overlap between the emission spectrum of the energy donor and energy acceptor, which is also depicted in Figure 2.9 [227].These modalities have been used to detect cadmium via the methanol solution of HQZn and further indicators with success, but the simultaneous detection of multiple species remains an issue.

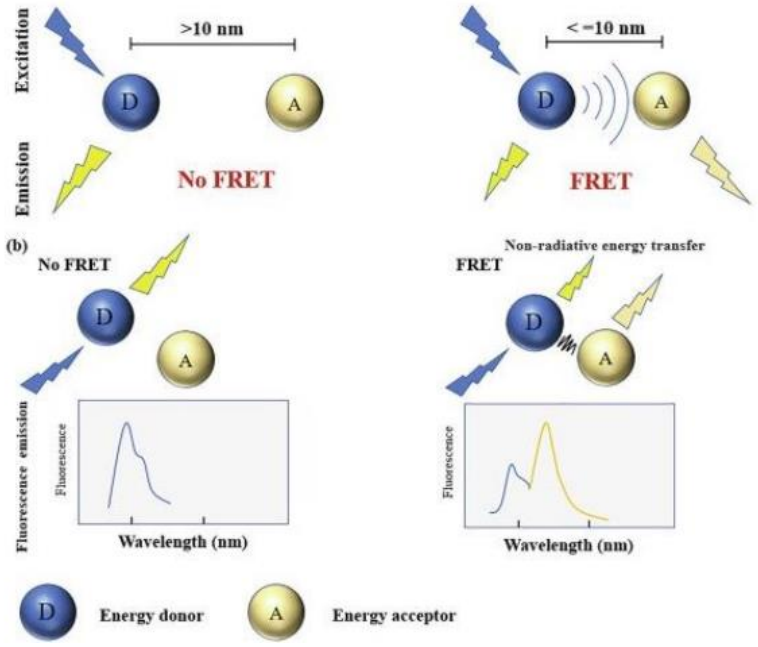

Figure 2. 9. The distance and wavelength spectral conditions needed to ensure FRET [228].

2.6. The significance of detecting heavy metals

Heavy metals are High atomic weight metallic chemical elements that may be hazardous to the environment and living things [229]. Lead, mercury, and cadmium are among the hazardous metals; others, like zinc, copper, manganese, and nickel, are poisonous at higher concentrations but are beneficial to humans at trace amounts. Furthermore, some hazardous semi-metals like selenium and arsenic are regarded as being just as harmful as heavy metals [231,232]. Exposure to heavy metals at abnormal quantities has a number of detrimental health impacts and can cause a variety of illnesses. In addition to food, medicine, and other factors, exposure can come from industrial operations including smelting and the disposal of production waste [233]. Since metals do not eventually break down into innocuous chemicals, heavy metal pollution differs from pollution caused by numerous organic species. There is a growing need for analytical methods that can be used to track the presence of heavy metals in biological matrices like blood, sweat, and urine as well as in the environment because of the widespread industrial and agricultural use of these substances and their potentially harmful effects on humans and other organisms. The intricate connections between the body's metal concentration and harmful pathological consequences have led to a constant need for more advanced analytical instruments with higher heavy metal detection sensitivity and selectivity.

2.7. Advantages of nanomaterials in the development of a sensor for detecting heavy metals

Chemical sensors based on nanomaterials have been widely used in heavy metal detection as an effective analytical tool. Numerous advantages of these nanosensors include improved mobility, selectivity, high sensitivity, device performance, and the capacity to detect things on-site. Because of their high surface-to-volume ratio, high reactivity, high level of functionalization, and size-dependent properties, nanosensors have a higher sensitivity [234]. Due to their high surface-to-volume ratios, nanoparticles and nanoclusters are more sensitive to environmental changes this makes them ideal choices for the detection and measurement of minute amounts of signals or analytes [235]. High selectivity in detecting particular chemicals or target analytes is made possible by functionalizing nanoparticles and nanoclusters with particular compounds or coatings.

This makes it possible to precisely identify and separate out different substances, contaminants, or biomarkers. Nanosensors are suited for real-time monitoring applications because of their small size and quick reaction. They have the ability to collect data continuously and instantly, making it possible to notice changes or events right away. Superior adsorbents based on carbon have been investigated for the removal of various inorganic and organic contaminants. Their tunable surface functional groups are the most crucial component of effective carbon adsorbents for heavy metals (HMs). According to Vilela et al. (2016), the innovative graphene-oxide-based microbots, or GOx-microbots, are self-propelled, active devices designed to remove and capture heavy metals (HMs), such as lead, and then recover them for recycling [236].

REFERENCES

1. Hasan, S. (2015) 'A Review on Nanoparticles: Their Synthesis and Types Biosynthesis: Mechanism,'4, pp. 9-11.
2. Divesh, G. (2019) 'A Literature Review of Nanotechnology,' JETIR, 6 (1).
3. Jeevanandam, J. et al. (2018) 'Review on nanoparticles and nanostructured materials: History, sources, toxicity and regulations,' Beilstein J. Nanotechnol, 9, pp.1050-1074.
4. Barik, T.K., Maity, G.C., Gupta, P., Mohan, L., Santra, T.S. (2021) Nanomaterials: An Introduction. Nanomaterials and Their Biomedical Applications, 16(1).
5. Singh, B.K. et al. (2020) An overview on metal-related catalysts: metal oxides, nanoporous metals and supported metal nanoparticles on metal organic frameworks and zeolites. Rare Metals, 39, pp. 751-766.
6. Salem, S.S. et al. (2020) 'Antibacterial, Cytotoxicity and Larvicidal Activity of Green Synthesized Selenium Nanoparticles Using Penicillium corylophilum,' Journal of Cluster Science, 32(2), pp. 351-361.
7. Khan, S. et al. (2022) 'A review on nanotechnology: Properties, applications, and mechanistic insights of cellular uptake mechanisms,' Journal of Molecular Liquids, 348, p. 118008.

8. Pérez-Hernández. H. et al. (2021) ‘Ecological drawbacks of nanomaterials produced on an industrial scale: Collateral effect on human and environmental health,’ Water, Air, & Soil Pollution, 232(10).
9. Singh, R. and Singh, S. (2019) ‘Nanomanipulation of consumer goods: Effects on human health and environment,’ in Springer eBooks, pp. 221-254
10. Pathakoti, K. et al. (2019) ‘Nanoparticles and their potential applications in agriculture, biological therapies, food, biomedical, and pharmaceutical industry: a review,’ in Apple Academic Press eBooks, pp. 121-162.
11. Elkodous, M. et al. (2021) ‘Recent advances in waste-recycled nanomaterials for biomedical applications: Waste-to-wealth,’ Nanotechnology Reviews, 10(1), pp. 1662-1739.
12. Laurent, S. et al. (2008) ‘Magnetic iron oxide nanoparticles: synthesis, stabilization, vectorization, physicochemical characterizations, and biological applications,’ Chemical Reviews, 108(6), pp. 2064-2110.
13. Tiwari, J.N. et al. (2012) ‘Zero-dimensional, one-dimensional, two-dimensional and three-dimensional nanostructured materials for advanced electrochemical energy devices,’ Progress in Materials Science, 57(4), pp. 724-803.
14. Parveen, S. et al. (2012) ‘Nanoparticles: a boon to drug delivery, therapeutics, diagnostics and imaging,’ Nanomedicine: Nanotechnology, Biology and Medicine, 8(2), pp. 147-166.
15. Noruzi, M. et al. (2011) ‘Rapid green synthesis of gold nanoparticles using Rosa hybrida petal extract at room temperature,’ Spectrochimica Acta Part A: Molecular and Biomolecular Spectroscopy, 79(5), pp. 1461-1465.
16. Subara, D. and Jaswir, I. (2018) ‘Gold Nanoparticles: Synthesis and application for Halal Authentication in Meat and Meat Products,’ International Journal on Advanced Science Engineering and Information Technology, 8(4-2), pp. 1633-1641.
17. Thayer, A. (2007) ‘BUILDING UP NANOTECH RESEARCH,’ Chemical & Engineering News, 85(15), pp. 15-21.
18. Horton, M.A. and Khan, A. (2006) ‘Medical nanotechnology in the UK: a perspective from the London Centre for Nanotechnology,’ Nanomedicine: Nanotechnology, Biology and Medicine, 2(1), pp. 42-48.

19. Kawasaki, E.S. and Player, A. (2005) ‘Nanotechnology, nanomedicine, and the development of new, effective therapies for cancer,’ Nanomedicine: Nanotechnology, Biology and Medicine, 1(2), pp. 101-109.
20. Minakshi, D. et al. (2012) ‘Review on gold nanoparticles and their applications,’ Toxicology and Environmental Health Sciences,3(4).
21. Britto, J.D. and Sebastian, S.R. (2011) ‘Biosynthesis of silver nano particles and its antibacterial activity against human pathogens,’ Int J Pharm Pharm Sci, 5, pp. 257-259.
22. Sun, T. and Seff, K. (1994) ‘Silver Clusters and Chemistry in Zeolites,’ Chemical Reviews, 94(4), pp. 857-870.
23. Hussain, J. et al. (2011b) ‘Silver nanoparticles: preparation, characterization, and kinetics,’ Advanced Materials Letters, 2(3), pp. 188-194.
24. Soares, J.M. et al. (2011) ‘Exchange-spring behavior in nanopowders of $CoFe_2O_4$-$CoFe_2$,’ Applied Physics Letters, 98(7).
25. Patil, S. et al. (2015) ‘Green synthesis of silver nanoparticle from leaf extract of Aegle marmelos and evaluation of its antibacterial activity,’ Int J Pharm Pharm Sci, 7(6), pp. 169-173.
26. Hussain, J. et al. (2011) ‘Silver nanoparticles: preparation, characterization, and kinetics,’ Advanced Materials Letters, 2(3), pp. 188-194.
27. Henglein, A. (1989) ‘Small-particle research: physicochemical properties of extremely small colloidal metal and semiconductor particles,’ Chemical Reviews, 89(8), pp. 1861-1873.
28. Zuo, Y.N. et al. (2015) ‘Transport, fate, and stimulating impact of silver nanoparticles on the removal of Cd (II) by Phanerochaete chrysosporium in aqueous solutions,’ Journal of Hazardous Materials, 285, pp. 236-244.
29. Gawande, M.B. et al. (2016) ‘Cu and Cu-Based Nanoparticles: Synthesis and Applications in Catalysis,’ Chemical Reviews, 116(6), pp. 3722-3811.
30. Mohajerani, A. et al. (2019) ‘Nanoparticles in construction materials and other applications, and implications of nanoparticle use,’ Materials, 12(19), p. 3052.
31. Al-Hakkani, M.F. (2020) ‘Biogenic copper nanoparticles and their applications: A review,’ SN Applied Sciences, 2(3).

32. Gracia-Pinilla, M.A. et al. (2009) ‘Deposition of size-selected Cu nanoparticles by inert gas condensation,’ Nanoscale Research Letters, 5(1).
33. Pham, L.Q. et al. (2012) ‘Copper nanoparticles incorporated with conducting polymer: Effects of copper concentration and surfactants on the stability and conductivity,’ Journal of Colloid and Interface Science, 365(1), pp. 103-109.
34. Cioffi, N. et al. (2005) ‘Synthesis, analytical characterization and bioactivity of Ag and Cu nanoparticles embedded in poly-vinyl-methyl-ketone films,’ Analytical and Bioanalytical Chemistry, 382(8), pp. 1912-1918.
35. Mishra, G. et al. (2011) ‘Synthesis and ultrasonic characterization of CU/PVP Nanoparticles-Polymer suspensions,’ Open Journal of Acoustics, 01(01), pp. 9-14.
36. Terna, A.D. et al. (2021) ‘The future of semiconductors nanoparticles: Synthesis, properties and applications,’ Materials Science and Engineering: B, 272, p. 115363.
37. Abdullah, B.J. (2022) ‘Size effect of band gap in semiconductor nanocrystals and nanostructures from density functional theory within HSE06,’ Materials Science in Semiconductor Processing, 137, p. 106214.
38. Fang, J. et al. (2019) ‘Recent advances in low-dimensional semiconductor nanomaterials and their applications in high-performance photodetectors,’ InfoMat, 2(2), pp. 291-317.
39. Lindroos, S. et al. (2000) ‘Growth of CuS thin films by the successive ionic layer adsorption and reaction method,’ Applied Surface Science, 158(1-2), pp. 75-80.
40. Lotfipour, M. et al. (2011) ‘A-Chalcocite nanoparticle synthesis and stability,’ Chemistry of Materials, 23(12), pp. 3032-3038.
41. Lin, M.-C. and Lee, M. (2011) ‘$Cu_{2-x}S$ quantum dot-sensitized solar cells,’ Electrochemistry Communications, 13(12), pp. 1376-1378.
42. Gao, L. et al. (2004) ‘Microemulsion-directed synthesis of different CuS nanocrystals,’ Solid State Communications, 130(5), pp. 309-312.
43. Lu, Q. et al. (2002) ‘One-Step synthesis and assembly of copper sulfide nanoparticles to nanowires, nanotubes, and nanovesicles by a simple organic Amine-Assisted hydrothermal process,’ Nano Letters, 2(7), pp. 725-728.
44. Roy, P. et al. (2008) ‘Synthesis of twinned CuS nanorods by a simple wet chemical method,’ Crystal Growth & Design, 8(5), pp. 1530-1534.

45. Roy, P. and Srivastava, S.K. (2007) ‘Low-temperature synthesis of CuS nanorods by simple wet chemical method,’ Materials Letters, 61(8-9), pp. 1693-1697.
46. Jiang, X. et al. (2000) ‘Preparation and phase transformation of nanocrystalline copper sulfides (Cu_9S_8, Cu_7S_4 and CuS) at low temperature,’ Journal of Materials Chemistry, 10(9), pp. 2193-2196.
47. Saranya, M. and Grace, A.N. (2012) ‘Hydrothermal Synthesis of CuS Nanostructures with Different Morphology,’ Journal of Nano Research, 18-19, pp. 43-51.
48. Xu, H. et al. (2006) ‘Sonochemical synthesis of crystalline CuS nanoplates via an in-situ template route,’ Materials Letters, 60(17-18), pp. 2203-2206.
49. Zhang, H. et al. (2008) ‘Phase-Selective synthesis and Self-Assembly of monodisperse copper sulfide nanocrystals,’ The Journal of Physical Chemistry C, 112(35), pp. 13390-13394.
50. Zhang, J. et al. (2011) ‘Visible light photocatalytic H2-Production activity of CuS/ZnS porous nanosheets based on photoinduced interfacial charge transfer,’ Nano Letters, 11(11), pp. 4774-4779.
51. Zhu, Y. et al. (2007) ‘Controllable synthesis of CuS nanotubes and nanobelts using lyotropic liquid crystal templates,’ Journal of Materials Science, 42(3), pp. 1042-1045.
52. Xu, L. et al. (2009) ‘Facile preparation of copper sulfide nanoparticles from perovskite templates containing bromide anions,’ Colloids and Surfaces A: Physicochemical and Engineering Aspects, 349(1-3), pp. 69-73.
53. Li, Z. et al. (2012) ‘Bubble template synthesis of copper sulfide hollow spheres and their applications in lithium-ion battery,’ Materials Letters, 68, pp. 28-31.
54. Wang, Y. et al. (2010) ‘Ion-Exchange synthesis and enhanced Visible-Light photoactivity of CuS/ZnS nanocomposite hollow spheres,’ The Journal of Physical Chemistry C, 114(32), pp. 13642-13649.
55. Wang, Y. et al. (2010) ‘One-Pot synthesis and optical property of Copper(I) sulfide nanodisks,’ Inorganic Chemistry, 49(14), pp. 6601-6608.
56. Jiao, S. et al. ‘(2006) Well-defined non-spherical copper sulfide mesocages with single-crystalline shells by shape-controlled Cu_2O crystal templating,’ Advanced Materials, 18(9), pp.1174-1177.

57. Chung, J. and Sohn, H. (2002) ‘Electrochemical behaviors of CuS as a cathode material for lithium secondary batteries,’ Journal of Power Sources, 108(1-2), pp. 226-231.
58. Raevskaya, A.E. et al. (2004) ‘Catalytic activity of CuS nanoparticles in hydrosulfide ions air oxidation,’ Journal of Molecular Catalysis A-chemical, 212(1-2), pp. 259-265.
59. Sagade, A.A. and Sharma, R. (2008) ‘Copper sulphide (Cu_xS) as an ammonia gas sensor working at room temperature,’ Sensors and Actuators B: Chemical, 133(1), pp. 135-143.
60. Wu, Y. et al. (2008) ‘Synthesis and photovoltaic application of Copper(I) sulfide nanocrystals,’ Nano Letters, 8(8), pp. 2551-2555.
61. Huang, Y. et al. (2009) ‘Preparation and characterization of CuS hollow spheres,’ Ceramics International, 35(2), pp. 905-907
62. Huang, Y. et al. (2009) ‘Preparation and characterization of CuS hollow spheres,’ Ceramics International, 35(2), pp. 905-907
63. Sagade, A.A. and Sharma, R. (2008b) ‘Copper sulphide (Cu_xS) as an ammonia gas sensor working at room temperature,’ Sensors and Actuators B: Chemical, 133(1), pp. 135-143.
64. Ku, G. et al. (2012) ‘Copper Sulfide Nanoparticles as a New Class of Photoacoustic Contrast Agent for Deep Tissue Imaging at 1064 nm,’ ACS Nano, 6(8), pp. 7489-7496.
65. Li, Y. et al. (2010) ‘Copper sulfide nanoparticles for photothermal ablation of tumor cells,’ Nanomedicine, 5(8), pp. 1161-1171.
66. Ramadan, S. et al. (2012) ‘Hollow Copper Sulfide Nanoparticle-Mediated Transdermal Drug delivery,’ Small, 8(20), pp. 3143-3150.
67. Zhou, M. et al. (2010) ‘A chelator-free multifunctional [64Cu] CuS nanoparticle platform for simultaneous micro-PET/CT imaging and photothermal ablation therapy,’ Journal of the American Chemical Society, 132(43), pp.15351-15358.
68. Ramadan, S. et al. (2012) ‘Hollow Copper Sulfide Nanoparticle-Mediated Transdermal Drug delivery,’ Small, 8(20), pp. 3143-3150
69. Villars, P. and Calvert, L.D. (1985) ‘Pearson’s Handbook of Crystallographic Data for Intermetallic Phases Vol.3,’ ASM International, Metals Park, OH.

70. Chen, C.C. et al. (1997) ‘Size Dependence of structural metastability in semiconductor nanocrystals,’ Science, 276(5311), pp. 398-401.
71. Banerjee, R. et al. (2000) ‘Effect of the size-induced structural transformation on the band gap in CdS nanoparticles,’ Journal of Physics: Condensed Matter, 12(50), pp. 10647-10654.
72. Li, Y. et al. (1998) ‘Nonaqueous synthesis of CDS Nanorod semiconductor,’ Chemistry of Materials, 10(9), pp. 2301-2303.
73. Wang, Q. et al. (2005) ‘Synthesis of single crystalline CdS nanorods by a PVP-assisted solvothermal method,’ Materials Letters, 59(21), pp. 2625-2629.
74. Gao, X., Chan, W.C.W. and Nie, S. (2002) ‘Quantum-dot nanocrystals for ultrasensitive biological labeling and multicolor optical encoding,’ Journal of Biomedical Optics, 7(4), p. 532.
75. Zhao, F. et al. (2006) ‘Selectively hydrothermal and solvothermal growth of CdS nanospheres and nanorods: a facile way to tune finely optical properties,’ Journal of Materials Science, 41(5), pp. 1449-1454.
76. Chen, M. et al. (2006) ‘Synthesis of CdS nanoplates by PAA-assisted hydrothermal approach,’ Materials Letters, 60(29-30), pp. 3842-3845.
77. Braun, P.V. et al. (1999) ‘Nanostructure Templating in Inorganic Solids with Organic Lyotropic Liquid Crystals,’ Journal of the American Chemical Society, 121(32), pp. 7302-7309.
78. Reiß, P. et al. (2004) ‘Luminescent ZnSe nanocrystals of high color purity,’ Materials Chemistry and Physics, 84(1), pp. 10-13.
79. Neikov, O.D. et al. (2008) Handbook of Non-Ferrous Metal Powders: Technologies and Applications.
80. Cheng, C. and Chen, Y. (2009) ‘Low temperature synthesis of ZnSe nanowires by self-catalytic liquid-solid growth,’ Materials Chemistry and Physics, 115(1), pp. 158-160.
81. Yang, J. et al. (2007) ‘Synthesis, nonlinear optical properties and photoluminescence of ZnSe quantum dots in stable solutions,’ Materials Letters, 61(7), pp. 1541-1543.
82. Feng, B. et al. (2014) ‘ZnSe nanoparticles of different sizes: Optical and photocatalytic properties,’ Materials Science in Semiconductor Processing, 27, pp. 865-872.

83. Hanada, T. (2009) ‘Basic properties of ZNO, GAN, and related materials,’ in Advances in materials research (Berlin), pp. 1-19.
84. “Zinc oxide,” [Online]. Available: https://en.wikipedia.org/wiki/Zinc_oxide. [Accessed 28 January 2024].
85. B. Zeghbroeck, ‘Semiconductor Fundamentals,’ [Online]. Available: https://ecee.colorado.edu/~bart/book/book/chapter2/ch2_2.htm. [Accessed 16 February 2023]
86. Özgür, Ü. et al. (2005) ‘A comprehensive review of ZnO materials and devices,’ Journal of Applied Physics, 98(4).
87. Cava, R.J. (1990) ‘Structural chemistry and the local charge picture of copper oxide superconductors,’ Science, 247(4943), pp. 656-662.
88. Tranquada, J.M. et al. (1995) ‘Evidence for stripe correlations of spins and holes in copper oxide superconductors,’ Nature, 375(6532), pp. 561-563.
89. Kumar, V. et al. (2013) January ‘Copper oxide based low-cost thin film solar cells,’ In 2013 IEEE 5th international nanoelectronics conference (INEC), pp. 443-445.
90. Yecheskel, Y. et al. (2013) ‘Catalytic degradation of brominated flame retardants by copper oxide nanoparticles,’ Chemosphere, 93(1), pp. 172-177.
91. Aslani, A. and Oroojpour, V. (2011) ‘CO gas sensing of CuO nanostructures, synthesized by an assisted solvothermal wet chemical route,’ Physica B: Condensed Matter, 406(2), pp. 144-149.
92. Wang, X. et al. (1999) ‘Thermal conductivity of nanoparticle - fluid mixture,’ Journal of Thermophysics and Heat Transfer, 13(4), pp. 474-480.
93. Ishio, S. et al. (2012) ‘L10 FePt thin films with [0 0 1] crystalline growth fabricated by SiO_2 addition-rapid thermal annealing and dot patterning of the films,’ Journal of magnetism and magnetic materials, 324(3), pp.295-302.
94. Xu, J. et al. (1999) ‘Preparation and characterization of CuO Nanocrystals,’ Journal of Solid State Chemistry, 147(2), pp. 516-519.
95. Namburu, P.K. et al. (2007) ‘Viscosity of copper oxide nanoparticles dispersed in ethylene glycol and water mixture,’ Experimental Thermal and Fluid Science, 32(2), pp. 397-402.

96. Chowdhuri, A. et al. (2004) ‘Response speed of SnO_2-based H_2S gas sensors with CuO nanoparticles,’ Applied Physics Letters, 84(7), pp. 1180-1182.
97. Jammi, S. et al. (2009) ‘CuO nanoparticles Catalyzed C-N, C-O, and C-S Cross-Coupling Reactions: scope and Mechanism,’ The Journal of Organic Chemistry, 74(5), pp. 1971-1976.
98. Zhang, D. et al. (2005) ‘Cu nanoparticles derived from CuO electrodes in lithium cells,’ Nanotechnology, 16(10), pp. 2338-2341.
99. Dar, M.A. et al. (2008) ‘Structural and magnetic properties of CuO nanoneedles synthesized by hydrothermal method,’ Applied Surface Science, 254(22), pp. 7477-7481.
100. Yin, M. et al. (2005) ‘Copper oxide nanocrystals,’ Journal of the American Chemical Society, 127(26), pp. 9506-9511.
101. Zhou, K. et al. (2006) ‘Synthesis, characterization and catalytic properties of CuO nanocrystals with various shapes,’ Nanotechnology, 17(15), pp. 3939-3943.
102. Chang, H. et al. (2005) ‘Rheology of CuO nanoparticle suspension prepared by ASNSS,’ Rev. Adv. Mater. Sci, 10(2), pp.128-132.
103. Battez, A.H. et al. (2008) ‘CuO, ZrO2 and ZnO nanoparticles as antiwear additive in oil lubricants,’ Wear, 265(3-4), pp. 422-428.
104. Battez, A.H. et al. (2010) ‘Friction reduction properties of a CuO nanolubricant used as lubricant for a NiCrBSi coating,’ Wear, 268(1-2), pp. 325-328.
104. Pan, X. et al. (2010) ‘Mutagenicity evaluation of metal oxide nanoparticles by the bacterial reverse mutation assay,’ Chemosphere, 79(1), pp. 113-116.
106. Stoimenov, P.K. et al. (2002) ‘Metal oxide nanoparticles as bactericidal agents,’ Langmuir, 18(17), pp. 6679-6686.
107. Ren, G. et al. (2009) ‘Characterization of copper oxide nanoparticles for antimicrobial applications,’ International Journal of Antimicrobial Agents, 33(6), pp. 587-590.
108. Bandyopadhyay, A. (2020) ‘A review on role of tetra-rings in graphene systems and their possible applications,’ Reports on Progress in Physics, 83(5), pp. 056501.
109. Husnah, M. et al. (2017) ‘A modified Marcano method for improving electrical properties of reduced graphene oxide (rGO),’ Materials Research Express, 4(6), p. 064001.

110. Ganesan, K. et al. (2020) ‘Green synthesis of Copper oxide nanoparticles decorated with graphene oxide for anticancer activity and catalytic applications,’ Arabian Journal of Chemistry, 13(8), pp. 6802-6814.
111. Chang, C.-W. (2006) ‘Electrical and thermal transport measurements on nano-structuredmaterials,’ PhDT [Preprint]. http://ui.adsabs.harvard.edu/abs/2006PhDT244C/abstract.
112. Buseck, P.R. et al. (1992) ‘Fullerenes from the Geological Environment,’ Science, 257(5067), pp. 215-217.
113. Kumar, S. (2023) ‘Carbon based nanomaterial for removal of heavy metals from wastewater: a review,’ International Journal of Environmental Analytical Chemistry, 103(19), pp. 7961-7978.
114. Tong, Z. et al. (2007) ‘Impact of fullerene (C60) on a soil microbial community,’ Environmental Science & Technology, 41(8), pp. 2985-2991.
115. Mauter, M.S. and Elimelech, M. (2008) ‘Environmental applications of Carbon-Based nanomaterials,’ Environmental Science & Technology, 42(16), pp. 5843-5859.
116. Sokolov, V. I. (1999) ‘Chemistry of fullerenes, novel allotropic modifications of carbon,’ Russian Chemical Bulletin, 48(7), pp. 1197-1205.
117. Diederich, F. and Whetten, R.L. (1992) ‘Beyond C60: the higher fullerenes,’ Accounts of Chemical Research, 25(3), pp. 119-126.
118. Ettl, R. et al. (1991) ‘Isolation of C76, a chiral (D2) allotrope of carbon,’ Nature, 353(6340), pp. 149-153.
119. Ulloa, E. (2013) ‘Fullerenes and their Applications in Science and Technology,’ Introduction to nanotechnology, 4138296.
120. Pal, S.L. et al. (2011) ‘Nanoparticle: An overview of preparation and characterization,’ Journal of applied pharmaceutical science, (Issue), pp. 228-234.
121. Popov, V.N. (2004) ‘Carbon nanotubes: properties and application,’ Materials Science and Engineering: R: Reports, 43(3), pp. 61-102.
122. Eatemadi, A. et al. (2014) ‘Carbon nanotubes: properties, synthesis, purification, and medical applications,’ Nanoscale research letters, 9, pp. 1-13.

123. Makgabutlane, B. et al. (2022) ‘Plastic-fly ash waste composites reinforced with carbon nanotubes for sustainable building and construction applications: A review,’ Results in Chemistry, 4, p. 100405.
124. Brock, S.L. (2004) ‘Nanostructures and Nanomaterials: Synthesis, Properties and Applications by Guozhang Cao (University of Washington),’ Imperial College Press (distributed by World Scientific): London, 434, pp. 78.
125. Singh, J. et al. (2018) ‘‘Green’ synthesis of metals and their oxide nanoparticles: applications for environmental remediation,’ Journal of Nanobiotechnology, 16(1).
126. Wang, A. et al. (2014) ‘In situ synthesis of copper nanoparticles within ionic liquid-in-vegetable oil microemulsions and their direct use as high efficient nanolubricants,’ RSC Advances, 4(85), pp. 45251-45257.
127. Gawande, M.B. et al. (2016) ‘Cu and Cu-based nanoparticles: synthesis and applications in catalysis,’ Chemical reviews, 116(6), pp. 3722-3811.
128. Bronikowski, M.J. (2006) ‘CVD growth of carbon nanotube bundle arrays,’ Carbon, 44(13), pp. 2822-2832.
129. Mayne, M. et al. (2001) ‘Pyrolytic production of aligned carbon nanotubes from homogeneously dispersed benzene-based aerosols,’ Chemical Physics Letters, 338(2-3), pp. 101-107.
130. Nikolaev, P. et al. (1999) ‘Gas-phase catalytic growth of single-walled carbon nanotubes from carbon monoxide,’ Chemical Physics Letters, 313(1-2), pp. 91-97.
131. Lee, C.J., Park, J. and Yu, J.A. (2002) ‘Catalyst effect on carbon nanotubes synthesized by thermal chemical vapor deposition,’ Chemical Physics Letters, 360(3-4), pp. 250-255.
132. Prášek, J. et al. (2011) ‘Methods for carbon nanotubes synthesis-review,’ Journal of Materials Chemistry, 21(40), p. 15872.
133. Chrzanowska, J. et al. (2015) ‘Synthesis of carbon nanotubes by the laser ablation method: Effect of laser wavelength,’ Physica Status Solidi (B) Basic Solid State Physics, 252(8), pp. 1860-1867.
134. Brodie, B.C. (1859) ‘XIII. On the atomic weight of graphite,’ Philosophical Transactions of the Royal Society of London, 149, pp. 249-259.

135. Novoselov, K.C. et al. (2004) ‘Electric field effect in atomically thin carbon films,’ Science, 306(5696), pp. 666-669.
136. Staudenmaier, L. (1898) ‘Verfahren zur darstellung der graphitsäure. Berichte der deutschen,’ chemischen Gesellschaft, 31(2), pp.1481-1487.
137. Gao, W. (2012) ‘Graphite oxide: Structure, reduction and applications (Doctoral dissertation, Rice University),’ pp. 6-10.
138. Papageorgiou, D.G. et al. (2015) ‘Graphene/elastomer nanocomposites,’ Carbon, 95, pp. 460-484.
139. Dan, L. (2017) ‘A Highly Effective Copper Nanoparticle Coupled with RGO for Electrochemical Detection of Heavy Metal Ions,’ International Journal of Electrochemical Science, 12(11), pp. 10933-10945.
140. Eda, G. and Chhowalla, M. (2010) ‘Chemically derived graphene oxide: towards Large-Area Thin-Film electronics and optoelectronics,’ Advanced Materials, 22(22), pp. 2392-2415.
141. Choi, W. et al. (2010) ‘Synthesis of Graphene and its applications: a review,’ Critical Reviews in Solid State and Materials Sciences, 35(1), pp. 52-71.
142. Tsou, C.H. et al. (2015) ‘Effect of microstructure of graphene oxide fabricated through different self-assembly techniques on 1-butanol dehydration,’ Journal of Membrane Science, 477, pp. 93-100.
143. Naficy, S. et al. (2014) ‘Graphene oxide dispersions: tuning rheology to enable fabrication,’ Materials Horizons, 1(3), pp. 326-331.
144. Liu, Y. and Feng, J. (2017) ‘An attempt towards fabricating reduced graphene oxide composites with traditional polymer processing techniques by adding chemical reduction agents,’ Composites Science and Technology, 140, pp. 16-22.
145. Liu, J. et al. (2018) ‘Nanoresolution patterning of hydrogenated graphene by electron beam induced C-H dissociation,’ Nanotechnology, 29(41), p. 415304.
146. Liu, J. et al. (2018) ‘Experimental observation of size-dependent behavior in surface energy of gold nanoparticles through atomic force microscope,’ Applied Physics Letters, 113(8).

147. Fukuma, T. (2009) ‘Subnanometer-Resolution frequency modulation atomic force microscopy in liquid for biological applications,’ Japanese Journal of Applied Physics, 48(8), pp. 08JA01.
148. El Badawi, N. et al. (2014) ‘Novel carbon nanotube-cellulose acetate nanocomposite membranes for water filtration applications,’ Desalination, 344, pp.79-85.
149. Xu, Y. et al. (2010) ‘In situ chemical fabrication of polyaniline/multi-walled carbon nanotubes composites as supports of Pt for methanol electrooxidation,’ Science China Chemistry, 53(9), pp. 2006-2014.
150. Xu, D. et al. (2014) ‘Preparation and Characterization of MnO2/acid-treated CNT Nanocomposites for Energy Storage with Zinc Ions,’ Electrochimica Acta, 133, pp. 254-261.
151. Murakami, H. et al. (2000) ‘Field emission from well-aligned, patterned, carbon nanotube emitters,’ Applied Physics Letters, 76(13), pp. 1776-1778.
152. Moreland, J.F. et al. (2004) ‘The disparate thermal conductivity of carbon nanotubes and diamond nanowires studied by atomistic simulation,’ Microscale Thermophysical Engineering, 8(1), pp. 61-69.
153. Xu, J. and Fisher, T.S. (2006) ‘Enhancement of thermal interface materials with carbon nanotube arrays,’ International Journal of Heat and Mass Transfer, 49(9-10), pp. 1658-1666.
154. Lebedeva, M.A. et al. (2016) ‘Stabilising the lowest energy charge-separated state in a {metal chromophore-fullerene} assembly: a tuneable panchromatic absorbing donor-acceptor triad,’ Chemical Science, 7(9), pp. 5908-5921.
155. Fowler, P. W., and Ceulemans, A. (1995) ‘A highly water soluble C60 - NVP Copolymer: Electron deficiency of the fullerenes, ‘J. Phys. Chem., 99, pp. 508-510.
156. Shanbogh, P.P. and Sundaram, N.G. (2015) ‘Fullerenes revisited,’ Resonance, 20(2), pp. 123-135.
157. Beg, S. et al. (2010) ‘Advancement in carbon nanotubes: basics, biomedical applications and toxicity,’ Journal of Pharmacy and Pharmacology, 63(2), pp. 141-163.
158. Coughlan, C. et al. (2017) ‘Compound Copper Chalcogenide nanocrystals,’ Chemical Reviews, 117(9), pp. 5865-6109.

159. Cui, J. et al. (2015) ‘Near-Infrared Plasmonic-Enhanced solar energy harvest for highly efficient photocatalytic reactions,’ Nano Letters, 15(10), pp. 6295-6301.
160. Alivisatos, A.P. (1996) ‘Semiconductor clusters, nanocrystals, and quantum dots,’ science, 271(5251), pp. 933-937.
161. Li, J. and Zhang, J.Z. (2009) ‘Optical properties and applications of hybrid semiconductor nanomaterials,’ Coordination Chemistry Reviews, 253(23-24), pp. 3015-3041.
162. Soloviev, V.N. et al. (2000) ‘Molecular limit of a bulk semiconductor: Size dependence of the “band gap” in CdSe cluster molecules,’ Journal of the American Chemical Society, 122(11), pp. 2673-2674.
163. Xin, S.H. et al. (1996) ‘Formation of self-assembling CdSe quantum dots on ZnSe by molecular beam epitaxy,’ Applied physics letters, 69(25), pp. 3884-3886.
164. Ajayan, P.M. (1999) ‘Nanotubes from carbon,’ Chem. Rev., 99, pp. 1787-1799.
165. Georgakilas, V. et al. (2015) ‘Broad family of carbon nanoallotropes: classification, chemistry, and applications of fullerenes, carbon dots, nanotubes, graphene, nanodiamonds, and combined superstructures,’ Chemical Reviews, 115(11), pp. 4744-4822.
166. Karousis, N. et al. (2010) ‘Current progress on the chemical modification of carbon nanotubes,’ Chemical Reviews, 110(9), pp. 5366-5397.
167. Mondal, P. et al. (2013) ‘Enhanced catalytic performance by copper nanoparticle-graphene based composite,’ RSC Advances, 3(16), pp. 5615.
168. Panda, U.C. et al. (2010) ‘Application of factor analysis in geochemical speciation of heavy metals in the sediments of a lake system-Chilika (India): a case study,’ Journal of Coastal Research, 26(5), pp. 860-868.
169. El-Sherif, I.Y. et al. (2008) ‘Biosorption of cadmium and nickel by Nile water algae,’ Journal of Applied Sciences Research, 4(4), pp. 391-396.
170. Bazrafshan, E. et al. (2006) ‘Removal of cadmium from industrial effluents by electrocoagulation process using iron electrodes,’ Iranian Journal of Environmental Health Science & Engineering, 3(4), pp. 261-266.

171. Elsherief, A.E. (2003) ‘Removal of cadmium from simulated wastewaters by electrodeposition on spiral wound steel electrode,’ Electrochimica Acta, 48(18), pp. 2667-2673.
172. Wong, E.H. et al. (2007) ‘The electrochemical detection of cadmium using surface-immobilized DNA,’ Electrochemistry Communications, 9(4), pp. 845-849.
173. Chailapakul, O. et al. (2008) ‘Fast and simultaneous detection of heavy metals using a simple and reliable microchip-electrochemistry route: An alternative approach to food analysis,’ Talanta, 74(4), pp. 683-689.
174. Singh, S. et al. (2011) ‘Potential of metal extractants in determination of,’ Advanced studies in biology, 3(5), pp. 239-246.
175. Lokhande, R.S. et al. (2011) ‘Toxicity study of heavy metals pollutants in waste water effluent samples collected from Taloja industrial estate of Mumbai, India,’ Resources and Environment, 1(1), pp. 13-19.
176. Michalski, R. et al. (2018) ‘Time and spatial variability in the concentrations of selected metals in water and bottom sediments of Pławniowice and Dzierżno Małe reservoirs (Poland),’ Journal of Environmental Science and Health, Part A, 53(3), pp. 230-237.
177. Kluska, M. et al. (2014) ‘Analysis of selected compounds in the surface water of lake Oleckie Wielkie,’ Oceanological and Hydrobiological Studies, 43, pp. 131-137.
178. Siudek, P. et al. (2016) ‘Atmospheric deposition of mercury in central Poland: sources and seasonal trends,’ Atmospheric research, 170, pp. 14-22.
179. Valko, M.M.H.C.M., et al. (2005) ‘Metals, toxicity and oxidative stress,’ Current medicinal chemistry, 12(10), pp. 1161-1208.
180. Sumner, E.R. et al. (2005) ‘Oxidative protein damage causes chromium toxicity in yeast,’ Microbiology, 151(6), pp. 1939-1948.
181. Poręba, R. et al. (2011) ‘Environmental and occupational exposure to lead as a potential risk factor for cardiovascular disease,’ Environmental Toxicology and Pharmacology, 31(2), pp. 267-277.
182. Joseph, C.L.M. et al. (2005) ‘Blood lead level and risk of asthma,’ Environmental Health Perspectives, 113(7), pp. 900-904.

183. Ruparelia, J. et al. (2008) ‘Potential of carbon nanomaterials for removal of heavy metals from water,’ Desalination, 232(1-3), pp. 145-156.
184. Brown, M.J. et al. (2011) ‘Association between children’s blood lead levels, lead service lines, and water disinfection, Washington, DC, 1998-2006,’ Environmental research, 111(1), pp. 67-74.
185. Burki, T.K. (2012) ‘Nigeria’s lead poisoning crisis could leave a long legacy,’ The Lancet, 379(9818), p. 792.
186. Beier, E.E. et al. (2013) ‘Heavy metal lead exposure, osteoporotic-like phenotype in an animal model, and depression of Wnt signaling,’ Environmental health perspectives, 121(1), pp. 97-104.
187. Liu, D. et al. (2010) ‘Bioaccumulation of lead and the effects of lead on catalase activity, glutathione levels, and chlorophyll content in the leaves of wheat,’ Communications in Soil Science and Plant Analysis, 41(8), pp. 935-944.
188. Chiba, M. et al. (1996) ‘Indices of Lead-Exposure in blood and urine of Lead-Exposed workers and concentrations of major and trace elements and activities of SOD, GSH-PX and catalase in their blood.,’ Tohoku Journal of Experimental Medicine, 178(1), pp. 49-62.
189. Rossi, E. (2008) ‘Low level environmental lead exposure-a continuing challenge,’ The Clinical Biochemist Reviews, 29(2), p. 63.
190. Ragan, P. and Turner, T. (2009) ‘Working to prevent lead poisoning in children: Getting the lead out,’ JAAPA, 22(7), p. 40.
191. ATSDR., (1999). International Occupational Safety and Health Information Centre. pp. 1-6.
192. Salem, H.M. et al. (2000) ‘September. Heavy metals in drinking water and their environmental impact on human health,’ In Int Conference on the Environ Hazards Mitigation, Cairo Univ Egypt, pp. 542-56.
193. Baum, C. et al. (2002) ‘Evaluation of Agro-industrial by Products a nutrient Source for Plant Growth,’ A Journal Archives of Agronomy and Soil Science, 4, pp. 445-460.
194. World Health Organization. (2004) ‘Guidelines for drinking-water quality (Vol. 1), ‘World Health Organization.

195. Ragan, P. and Turner, T. (2009b) 'Working to prevent lead poisoning in children: Getting the lead out,' JAAPA, 22(7), p. 40.
196. Assessment, U.G.M. (2013) 'Sources, emissions, releases and environmental transport,' UNEP Chemicals Branch, Geneva, Switzerland, 42.
197. Li, R. et al. (2017) 'Mercury pollution in vegetables, grains and soils from areas surrounding coal-fired power plants,' Scientific Reports, 7(1).
198. Satoh, H. (2000) 'Occupational and environmental toxicology of mercury and its compounds.,' Industrial Health, 38(2), pp. 153-164.
199. TA, G. and B. J.D. (1990) 'Principles of clinical toxicology,' 2nd ed. New york: Raven press. from areas surrounding coal-fired power plants. Scitific Reports,7:46545.
200. Chen, J. et al. (2020) 'Inhibition of tyrosinase by mercury chloride: spectroscopic and docking studies,' Frontiers in pharmacology, 11, p. 81.
201. USEPA, Treatment technologies for mercury in soil, waste, and water. 2007, United States Environmental Protection Agency (USEPA).
202. Genchi, G. et al. (2020) 'The effects of cadmium toxicity,' International Journal of Environmental Research and Public Health, 17(11), p. 3782.
203. Järup, L. et al. (1998) 'Mortality and cancer incidence in Swedish battery workers exposed to cadmium and nickel,' Occupational and Environmental Medicine, 55(11), pp. 755-759.
204. Jin, Y.J. et al. (2003) 'Cadmium is a mutagen that acts by inhibiting mismatch repair,' Nature Genetics, 34(3), pp. 326-329.
205. Wieland, M. et al. (2009) 'Mechanism of Cadmium-Mediated inhibition of MSH2-MSH6 function in DNA mismatch repair,' Biochemistry, 48(40), pp. 9492-9502.
206. Pellizzari, E.D. and Clayton, C.A. (2006) 'Assessing the measurement precision of various arsenic forms and arsenic exposure in the National Human Exposure Assessment Survey (NHEXAS),' Environmental Health Perspectives, 114(2), pp. 220-227.
207. Hughes, M.F. (2006) 'Biomarkers of Exposure: A Case Study with Inorganic Arsenic,' Environmental Health Perspectives, 114(11), pp. 1790-1796.
208. Garelick, H. et al. (2008) 'Arsenic pollution sources,' in Reviews of Environmental Contamination and Toxicology, pp. 17-60.

209. Ravenscroft, P. et al. (2009) 'Arsenic pollution: a global synthesis,' Choice Reviews Online, 47(02), pp. 47-0826.
210. Carapella Jr, S.C. (2000) ‘Arsenic and arsenic alloys,’ Kirk-Othmer Encyclopedia of Chemical Technology.
211. Windholz, M. (1990) ‘The Merck Index: an encyclopedia of chemicals, drugs, and biologicals,’ Annals of Internal Medicine, 113(6), p. 487.
212. Hung, D.Q. et al. (2004) ‘Analytical methods for inorganic arsenic in water: a review,’ Talanta, 64(2), pp. 269-277.
213. Komorowicz, I. and Barałkiewicz, D. (2011) ‘Arsenic and its speciation in water samples by high performance liquid chromatography inductively coupled plasma mass Spectrometry-Last decade review,’ Talanta, 84(2), pp. 247-261.
214. Gibbon-Walsh, K. et al. (2010) ‘Arsenic speciation in natural waters by cathodic stripping voltammetry,’ Analytica Chimica Acta, 662(1), pp. 1-8.
215. Gupta, D.K. et al. (2017b) ‘Arsenic Contamination from Historical Aspects to the Present,’ in Springer eBooks, pp. 1-12.
216. Lee, C.H. et al. (2006) ‘Defective β1-integrins expression in arsenical keratosis and arsenic-treated cultured human keratinocytes,’ Journal of cutaneous pathology, 33(2), pp.129-138.
217. Di Bona, K.R. et al. (2010) ‘Chromium is not an essential trace element for mammals: effects of a “low-chromium” diet,’ Journal of Biological Inorganic Chemistry, 16(3), pp. 381-390.
218. USEPA, 1998. IRIS Chromium. <http://www.epa.gov/ncea/iris/subst/0144.htm>, July 26, 2023.
219. Deng, Y. et al. (2019) ‘The effect of hexavalent chromium on the incidence and mortality of human cancers: A Meta-Analysis based on published epidemiological cohort studies,’ Frontiers in Oncology, 9.
220. De Flora, S. et al. (2008) ‘Lack of genotoxic effects in hematopoietic and gastrointestinal cells of mice receiving chromium(VI) with the drinking water,’ Mutation Research/Reviews in Mutation Research, 659(1-2), pp. 60-67.
221. Valko, M.M.H.C.M. et al. (2005) ‘Metals, toxicity and oxidative stress,’ Current medicinal chemistry, 12(10), pp. 1161-1208.

222. Sanilkumar, R. and Muthu, A.K. (2013) ‘Evaluation of in-vivo Antioxidant Activity of Methanolic Extract of Triumfetta rotundifolia (Linn.) on Streptozotocin induced Oxidative Stress in Wistar Rats,’ Journal of Pharmaceutical Sciences and Research, 5(12), p. 249.
223. Dayan, A.D. and Paine, A.J. et al. (2001) ‘Mechanisms of chromium toxicity, carcinogenicity and allergenicity: review of the literature from 1985 to 2000,’ Human & experimental toxicology, 20(9), pp. 439-451.
224. Kumar Dey, S. and Roy, S. (2009) ‘Effect of chromium on certain aspects of cellular toxicity,’ Iranian Journal of Toxicology, 2(4), pp. 260-267.
225. Patlolla, A.K. et al. (2009) ‘Oxidative stress, DNA damage, and antioxidant enzyme activity induced by hexavalent chromium in Sprague-Dawley rats,’ Environmental Toxicology: An International Journal, 24(1), pp. 66-73.
226. Malik, L.A. et al. (2019) ‘Detection and removal of heavy metal ions: a review,’ Environmental Chemistry Letters, 17, pp. 1495-1521.
227. Wang, X. et al. (2021) ‘Methods, principles and applications of optical detection of metal ions,’ Chemical Engineering Journal, 417, pp. 129-125.
228. Malik, L.A. et al. (2019) ‘Detection and removal of heavy metal ions: a review,’ Environmental Chemistry Letters, 17(4), pp. 1495-1521.
229. Jothimuthu, P. et al. (2011) ‘Lab-on-a-chip sensor for detection of highly electronegative heavy metals by anodic stripping voltammetry,’ Biomedical microdevices, 13, pp. 695-703.
230. Pei, X. et al. (2014) ‘Disposable Copper-Based electrochemical sensor for anodic stripping voltammetry,’ Analytical Chemistry, 86(10), pp. 4893-4900.
231. Wanekaya, A.K. (2011) ‘Applications of nanoscale carbon-based materials in heavy metal sensing and detection,’ Analyst, 136(21), pp. 4383-4391.
232. Aragay, G. and Merkoci, A. (2012) ‘Nanomaterials application in electrochemical detection of heavy metals,’ Electrochimica Acta, 84, pp. 49-61.
233. Tchounwou, P.B. et al. (2012) ‘Heavy metal toxicity and the environment,’ Molecular, clinical and environmental toxicology: volume 3: environmental toxicology, pp. 133-164.
234. Borah, S.B.D. et al. (2015) ‘Heavy metal ion sensing in water using surface plasmon resonance of metallic nanostructures,’ Groundwater for Sustainable Development, 1(1-2), pp. 1-11.

235. Wang, X. (2012) ‘Nanomaterials as sorbents to remove heavy metal ions in wastewater treatment,’ Journal of Environmental and Analytical Toxicology, 02(07).
236. Vilela, D. et al. (2016) ‘Graphene-Based Microbots for Toxic Heavy Metal Removal and Recovery from Water,’ Nano Letters, 16(4), pp. 2860-2866.

CHAPTER 3

CHARACTERIZATION TECHNIQUES

3.1. Introduction

In this chapter, different characterization techniques used in this research study are briefly explained. The details and concepts of the FTIR, TEM, UV-vis, XRD, EDX and Raman are fully provided.

3.2. Fourier-transform infrared spectroscopy (FTIR)

A fundamental and essential characterization method, infrared (IR) spectroscopy is used to ascertain a material's chemical composition and the molecular bonds that hold its constituent parts together. An infrared (IR) spectrum is created by shining infrared (IR) light on a sample and calculating the amount of light absorbed at each energy level. Therefore, by identifying the individual components or groups of atoms that absorb in the infrared at specific frequencies, molecule structure can be determined using infrared spectroscopy. Before (I_0) and after (I) an IR beam interacts with the sample, its intensity is measured or determined as a function of the light frequency $\{W_i\}$ in the infrared experiment. Certain vibrational modes create oscillations that enable matter to link and exchange energy with an IR electromagnetic radiation beam that is impinging on it when their frequencies are in resonance.

Figure 3.1 depicts the basic components of an FTIR spectrometer. The light is split into two equal intensity beams by a center mirror. Upon recombining and being reflected by the central mirror, the beams go to two more mirrors before entering the sample and the detector. A moveable side mirror and a fixed side mirror are present. FTIR spectroscopy (FTIR 8000, Perkin-Elmer) was carried out to study different functional groups during preparation of Cu-based nanomaterials in RGO. The FTIR spectrometer used in this study is shown in Figure 3.2.

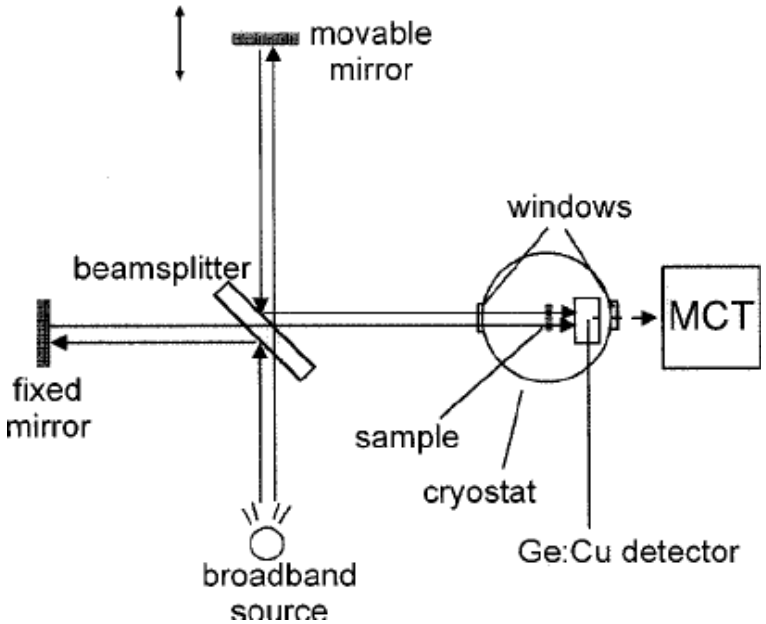

Figure 3. 1. Schematic diagram of a FTIR spectrometer [1].

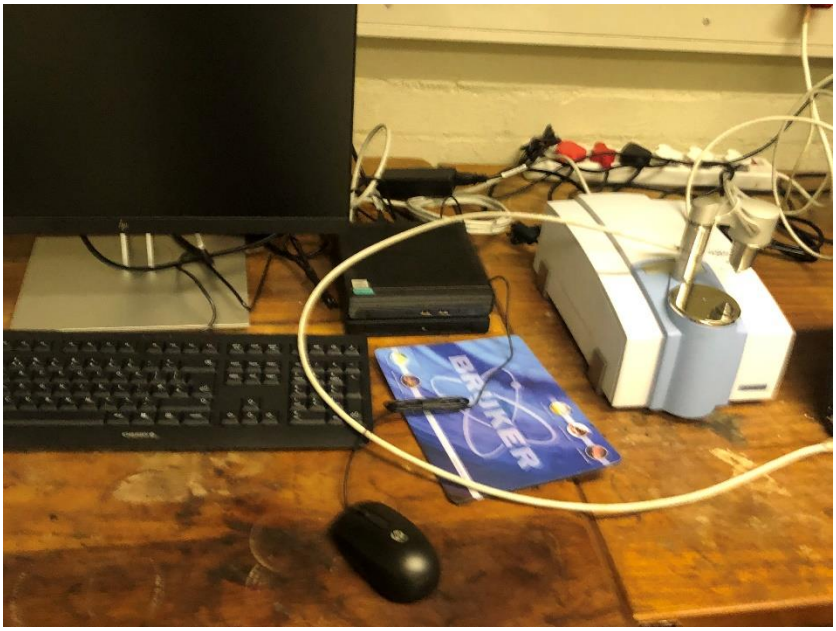

Figure 3. 2. The FTIR spectrometer used in this study.

3.3. Transmission electron microscopes (TEM)

Transmission electron microscopy involves the application of a consistent current density electron beam to a thin sample at energies typically ranging from 60 to 150 keV. High-energy electron beams are used to pass through an extremely thin specimen in the typical TEM mode. Since the electron beam and the sample interact electron-electron, the incident electron enters the thin specimen unscathed, elastically scattered, or inelastically scattered. If the diffracted electrons are unscattered or scattered, they can be focused using a series of electromagnetic lenses to generate an electron diffraction pattern.

Because the sample must be extremely thin for the electron transmission, TEM sample preparation is difficult and time-consuming. Support grids or films are coated with the dispersion of nanoparticles. In order to make nanoparticles resistant to the instrument vacuum and easier to handle, they are either embedded in plastic or fixed with a negative staining substance like uranyl acetate, phosphotungstic acid, or its derivatives.

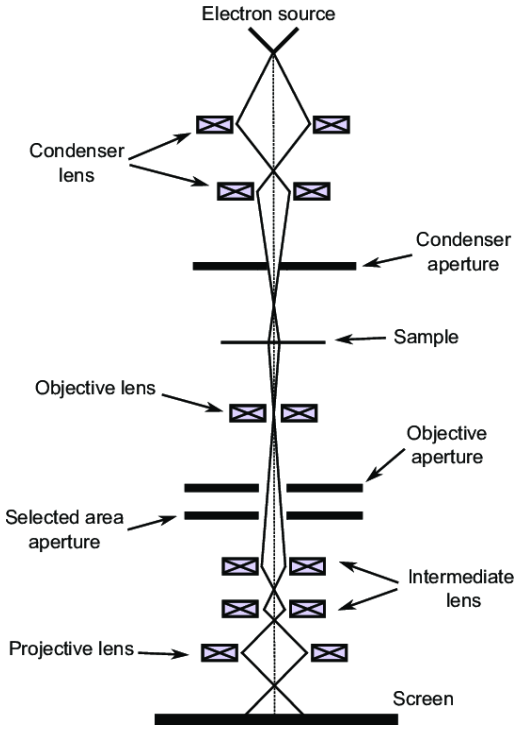

Figure 3. 3. Schematic diagram of transmission electron microscopy [2].

3.3. Energy dispersive X-ray spectroscopy (EDX)

Energy dispersive X-ray spectroscopy is an analytical instrument that is mostly employed in the field of chemical characterization. This type of spectroscopy relies on using light-matter interactions to examine a sample; in this case, X-ray analysis.

When the material to be analyzed is struck by high energy electron beams (in a TEM or SEM), X-rays are released. These X-rays can be identified, and the elemental composition of the specimen surface examined using a SiLi detector that has been calibrated with regard to cobalt metal emission (6.925 keV). The fundamental concept that each element in the Periodic Table has a unique electronic structure and, thus, a unique response to electromagnetic radiation is primarily in charge of its ability to be characterized.

3.5. Ultraviolet-visible (UV-Vis) Spectroscopy

UV-Vis spectroscopy is another rather simple and affordable characterization method that is widely used in the study of nanoscale materials. It measures how much light a sample reflects and compares that amount to how much light a reference substance reflects. This technique includes the sample absorbing part of the light and the light traveling through the sample to be analyzed. The sample must therefore be thin enough to allow for some light transmission. The material's valence electrons are activated from their ground states to higher energy excited states when they absorb visible or ultraviolet light.

The Beer-Lambert law is used to define absorbance when it is plotted as wavelength against absorbance in a spectrum:

$$A = -\log(\frac{I}{I0}) \qquad (3.1)$$

where I_0 is the incident light's intensity at a specific wavelength, I is the transmitted intensity, and A is the measured absorbance.

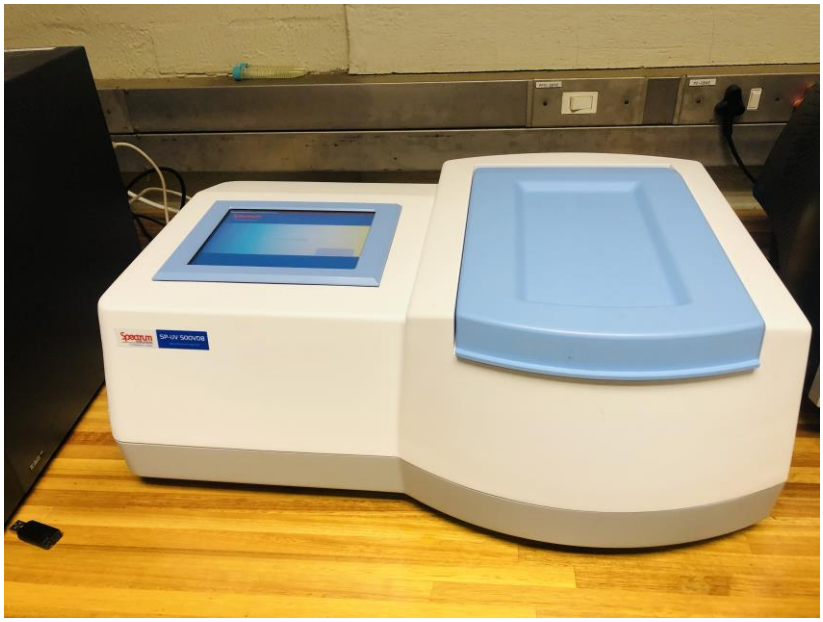

Figure 3. 4. UV-Vis spectrometer used in this research study.

3.6. X-ray diffraction (XRD)

X-ray diffraction is the fundamental method for learning about crystalline solids and their atomic structures. XRD usually yields data on the crystalline grain size, lattice parameters, phase type, and crystalline structure. The diffraction of X-rays from the material's crystalline plane at different angles is the fundamental XRD guideline. The crystalline plane and these diffraction models are related by Bragg's law (Figure 3.5)

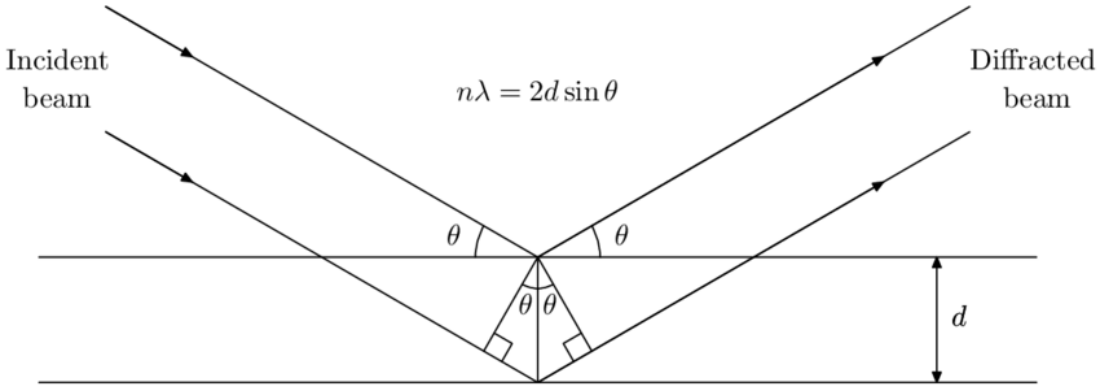

Figure 3. 5. Schematic diagram of Bragg's law [3].

Bragg's law for crystalline material diffraction: W. L. Bragg developed Braggs law, which states that the interatomic spacing is related to the X-ray wavelength and may be expressed as

$$n\lambda = 2d\,\sin\theta \tag{3.2}$$

Where θ is the angle between the diffracted wave and the atomic planes, λ is the wavelength of the X-ray beam and n is an integer value representing the order of the reflection and the wavelength path difference between waves scattered by neighboring atomic planes. The Scherrer equation is utilized to determine the crystalline grain size for a given sample by utilizing the widening of the most intense peak in an XRD measurement.

$$D = \frac{k\lambda}{\beta Cos\theta} \tag{3.3}$$

Where D is the particle size, β is the width at half maximum (FHWM) of the corresponding XRD peak, λ is the X-ray radiation wavelength in ångströms (Å), K is a constant that is very close to unity and is related to the crystallite shape and θ is the peak angle.

3.7. Raman spectroscopy

Raman spectroscopy explains that the interaction of light with materials can be accounted for by absorption, scattering, or even penetration of the material by photons. Molecules absorb photon energy and change from their ground state to an excited state. By detecting radiation losses from light, this process is quantified in absorption spectroscopy. The light that is scattered after molecules interact with it can be recognized by collecting light at an angle to the incoming light beam. When the incident light's frequency is increased to the fourth power, the scattering light's energy remains constant and increases in efficiency. When molecular vibrations are detected, Raman spectroscopy provides information about the physical form and chemical structure that is helpful in

identifying the substance. Raman and Krishnan made the first observation of this phenomena in 1928 [4].

Raman spectroscopy adheres to different selection principles and displays the vibrational information of a molecule in a manner comparable to that of infrared (IR) spectroscopy. For a vibrational mode to be Raman active, there must be a change in the polarizability during the vibration; in contrast, for a vibrational mode to be IR active, there must be a change in the dipole moment, which is strongly influenced by the symmetry of the molecule. The concept of mutual exclusion states that Raman active vibrations are often IR inactive for molecules having a center of symmetry and vice versa. However, because of the target molecules' excessively narrow Raman cross-section, which produces one Raman photon for every 106 to 1010 incident photons, the sensitivity of Raman spectroscopy is significantly lower than that of IR spectroscopy. Consequently, until the laser's creation as a monochromatic, high-power light source in the 1960s, the development of Raman spectroscopy was far slower than that of IR spectroscopy. The three main parts of a Raman spectrometer are the detector, sampling interface, and excitation laser (figure 3.6).

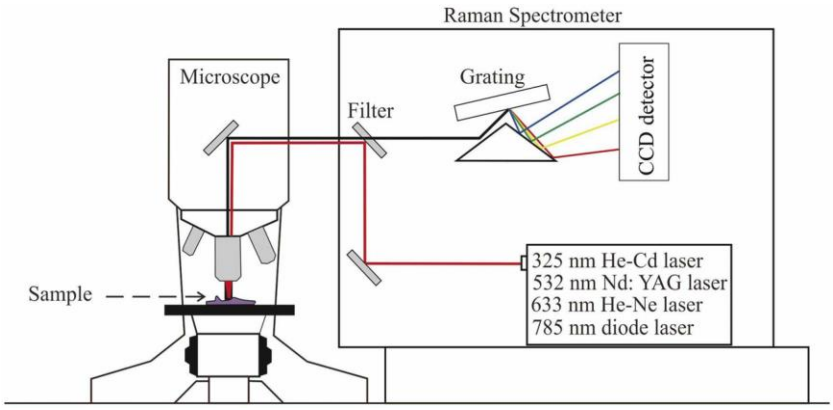

Figure 3. 6. A simple illustration of the modern Raman spectrometer [5].

REFERENCES

1. McCluskey, M.D. (2000) ‘Local vibrational modes of impurities in semiconductors,’ Journal of Applied Physics, 87(8), pp. 3593-3617.
2. Marturi, N. (2013) ’Vision and visual servoing for nanomanipulation and nanocharacterization in scanning electron microscope (Doctoral dissertation, ‘Université de Franche-Comté).
3. Sochi, T. (2010) ‘High Throughput Software for Powder Diffraction and its Application to Heterogeneous Catalysis,’ arXiv (Cornell University) [Preprint].
4. Singh, R. (2002) ‘CV Raman and the Discovery of the Raman Effect,’ Physics in Perspective, 4, pp. 399-420.
5. Chou, I. and Wang, A. (2017) ‘Application of laser Raman micro-analyses to Earth and planetary materials,’ Journal of Asian Earth Sciences, 145, pp. 309-333.

CHAPTER 4

METHODOLOGY AND ANALYTICAL PROCEDURES

4.1. Introduction

This chapter explores the materials and the methodical approach used to accomplish the objectives of this research. It includes detailed information on the procedure used for the preparations of graphene oxide (GO), reduced graphene oxide (RGO), Copper oxide nanoparticles (CuONPs), Copper sulfide nanoparticles (CuSNPs), CuO-Au-RGO nanocomposites and CuS-Au-RGO nanocomposites. There is also a brief explanation on the instrumentation and sample preparation.

4.2. Chemicals and instrumentation

4.2.1. Chemicals

All chemicals used in this project were purchased from Sigma Aldrich (South Africa), this includes graphite flakes, sodium nitrate ($NaNO_3$), 98% sulphuric acid (H_2SO_4), potassium permanganate ($KmnO_4$), hydrogen peroxide (H_2O_2), 5% hydrochloric acid (HCl), distilled water, ascorbic acid, copper chloride dihydrate ($CuCl_2.2H_2O$), cetyltrimethylammonium bromide (CTAB), glutathione (GSH), thioacetamide (TAA), dimethylformamide (DMF), and sodium hydroxide (NaOH).

4.2.2. Instrumentation

The UV-Vis spectra of GO, RGO, CuO, CuO-Au, CuO/RGO, CuO-Au/RGO, CuS, CuS-Au and CuS/RGO nanomaterials were captured using a Multiskan Go device (Thermo Fisher Scientific, Waltham, Massachusetts, USA). For the purpose of determining the particle size, shape, and morphology, transmission electron microscopy (TEM) pictures of the materials were captured on copper-coated grids using a 200 kV JEM-2100F Transmission Electron Microscope (JOEL USA Inc., Pleasanton, California, USA). Raman spectrometry investigations were conducted on gold-coated slides to investigate the chemical properties of the sensing platform. The PerkinElmer Raman Station 400 spectrometer (PerkinElmer Life and Analytical Services, Waltham, Massachusetts, USA)

was used to record the spectrums. Chronoamperometry (CA), square-wave voltammetry (SWV), and cyclic voltammetry (CV) were utilized to investigate the electrochemical activity of the sensing films. Using square-wave anodic stripping voltammetry (SWV-ASV), the various concentrations of Hg (II) were analytically measured. Metrohm Autolab B.V. PGSTA302N Potentiostat (Metrohm, Kanaalweg 29 G, Utrecht, The Netherlands) was used for all electrochemical measurements, and Nova 2.1 software was used to control it.

4.3. Synthetic procedures

4.3.1. Synthesis of graphene oxide

Graphene oxide was prepared using the modified Hummer's method [1]. Stepwise, a 0.5 g of graphite flakes, and 0.5 g (5.88 mmol) of $NaNO_3$ was mixed with 98 mL of H_2SO_4 in a 500 mL volumetric flask kept under an ice bath (<5 °C) with vigorous stirring for 4 h. Subsequently, 3 g (18.98 mmol) of potassium permanganate (KMnO4) was gradually added to the suspension and mixed for an additional hour. The ice bath was removed, and the mixture was stirred continuously for an hour at 35 °C. The mixture was then kept in a reflux system for 15 min with the temperature approximately at 98 °C. After 2 h, the mixture was allowed to cool at room temperature, followed by the addition of 100 mL of distilled water and stirred again for another hour. A 10 mL of hydrogen peroxide (H_2O_2) were added to the mixture to finish the reaction. After that, the mixture was repeatedly rinsed with distilled water and 5% HCl until the combination's pH reached 7 and a gel-like consistency formed. L.astly, the gel was dried overnight at 70 °C in an oven.

4.3.2. Reduction of graphene oxide

Reduced graphene oxide (RGO) was prepared using ascorbic acid as a reducing agent. A 0.04 g (0.23 mmol) of ascorbic acid was added into a 100 mL of GO dispersion. The mixture was then subjected to an ultrasonic treatment and placed for 30 minutes to obtain an rGO dispersion solution. The obtained RGO solution was then dried at 70 °C.

4.3.3. Preparation of copper based nanomaterials

4.3.3.1. Synthesis of copper sulfide (CuS) nanoparticles

CuS nanoparticles were prepared using a modified method by Tetyana et al. (2023) and Mofokeng et al. (2019) [2,3]. Copper chloride dihydrate ($CuCl_2.2H_2O$) was used as a copper source and thioacetamide (TAA) as a sulfur source with glutathione (GSH) used as a capping agent. Typically, a solution of the capping agent was prepared by adding 2.0 g (6.51 mmol) of GSH with 30 ml of dH_2O then introduced into a three-necked round-bottom flask and stirred at room temperature. Next, a solution of $CuCl_2.2H_2O$ (0.1 g/mL) was introduced dropwise into the flask. Next, dropwise additions of a 0.1 g/mL thioacetamide solution and a 1 M NaOH solution was added to the flask in order to bring the reaction's pH down to 9.0. To enhance particle growth, the mixture was then refluxed at a temperature of 90 °C under nitrogen gas for 60 min. Upon reaction completion, the mixture was washed with dH_2O and ethanol three times, and dried in an oven at 80 °C to obtain solid nanomaterials.

4.3.3.2. Synthesis of copper oxide (CuO) nanoparticles

CuO nanoparticles were synthesised using a co-precipitation method. First, a 1.7 g (9.97 mmol) of $CuCl_2.2H_2O$ was dissolved in a 100 mL of dH_2O and stirred continuously. next, a 1.8 g (4.94 mmol) of CTAB was added into the Cu precursor solution. A 1 M solution of NaOH was added dropwise until the pH of the reaction reached 14. Finally, the reaction was heated at 80 °C for 3 h forming a black precipitate. After three rounds of washing with dH2O and ethanol, the dark precipitate was dried in an oven at 80 °C for 12 hours. the product was further calcined at 500 °C for 4 hours to remove any impurities.

4.3.3.3. Preparation of CuS-Au and CuO-Au nanoparticles

A 100 mg of the as-synthesized CuO or CuS nanoparticles was dispersed in a 10 mL distilled water by ultrasonication for 4 h. Next, a 10 mL of $HauCl_4$ solution (1×10^{-2} M) was added into the as-prepared dispersion solution. The solution was stirred for 2 h, and the precipitate was washed with dH_2O to remove the extra $HauCl_4$. After ultrasonicating the precipitate for one hour in 10 ml of water, a 4.4 g (24.98 mmol) of ascorbic acid was added

and the mixture was agitated for 4 hours. The reddish wine colored precipitate was dried in an oven at 80 °C for 12 hours.

4.3.4. Preparation of CuO/RGO, CuS/RGO, CuO-Au/RGO and CuS-Au/RGO nanocomposites

4.3.4.1. Synthesis of CuO/RGO and CuS/RGO nanocomposites

A 0.08 g of RGO was dispersed in 40 mL of DMF for 2 hours under sonication. Next, 1 mg of the as-prepared CuO or CuS nanoparticles was added to the DMF-dispersed RGO solution and stirred for another 2 hours. The precipitate was washed with dH_2O three times and dried in an oven at 80 °C.

4.3.4.2. Synthesis of CuO-Au/RGO nanocomposites

CuO-Au/RGO nanocomposites were prepared using a one-step synthesis method. Typically, a 0.1 g of the as-prepared graphene oxide was dispersed in a 200 mL of dH_2O by ultrasonication for 2 h. Next, a 1.53 g (8.97 mmol) of $CuCl_2.2H_2O$ was added into the GO dispersion solution followed by the addition of 5 mL of $HauCl_4$ ($1x10^2$ M) solution under vigorous stirring. A 6 g (34.07 mmol) of ascorbic acid were added to the mixture after 60 minutes, and it was stirred for 4 hours. The precipitate was dried in an oven at 70 °C after being centrifuged and repeatedly washed with deionized water.

4.3.4.3. Synthesis of CuS/Au/RGO

A 1 mg of the as-synthesized CuS/Au nanoparticles was added to a 40 mL of DMF-dispersed RGO solution (2mg/mL). The mixture was then stirred for 2 hours in room temperature. The precipitate was then washed with dH_2O several times and dried in an oven at 70 °C.

4.4. Fabrication of CuS-Au/RGO/GCE sensor

CuS-Au/RGO nanocomposite was immobilized on the glassy-carbon electrode surface in order to prepare the sensor. In short, the working electrode surface of GCE was drop-casted with 5 uL of CuS-Au/RGO nanocomposite. The nanocomposite was left to absorb at room temperature for 24 hrs.

4.5. Preparation of Hg(II) and Cr(III) standard samples

The mercury (II) and chromium (III) stock solutions were made by dissolving the respective compounds in a sodium chloride and phosphate buffer (pH 2.6). The appropriate volumes of the stock solutions were further diluted with phosphate buffer solution to build up the necessary concentrations in order to prepare various concentrations of mercury (II) and chromium (III).

REFERENCES

1. Zaaba, N.I. et al. (2017) 'Synthesis of Graphene Oxide using Modified Hummers Method: Solvent Influence,' Procedia Engineering, 184, pp. 469-477.

2. Mofokeng, T.P. et al. (2019) 'Synthesis, characterization and cytotoxicity of alanine-capped CuS nanoparticles using human cervical carcinoma HeLa cells,' Analytical Biochemistry, 580, pp. 36-41.

3. Tetyana, P. et al. (2023) 'Synthesis, characterization, and electrochemical evaluation of copper sulfide nanoparticles and their application for Non-Enzymatic glucose detection in blood samples,' Nanomaterials, 13(3), p. 481.

CHAPTER 5

Results and discussion

5.1 Introduction

This chapter provides an overview of the produced copper based nanoparticles on RGO's experimental characterization. A presentation and discussion of the XRD, UV-Vis, FT-IR, Raman, EDX and TEM results.

5.2. Characterization of Graphene oxide (GO) and reduced graphene oxide (RGO)

5.2.1. Optical properties

Graphene oxide (GO) was prepared using a modified Hummer's method [1]. After successfully synthesizing GO, it was reduced via chemical reduction method, where ascorbic acid, which has the ability to function as a reducing agent and protecting agent was employed. UV-Vis spectroscopy analysis was used to track the transition of GO to RGO. Figure 5.1 shows the absorption spectra of an aqueous GO and RGO dispersions. The maximum absorption peak appearing at approximately 235 nm signify the successfully formation of GO. The observed maximum peak attributes to $\pi \rightarrow \pi^*$ transition of the aromatic C=C bonds [2]. In addition to the maximum peak observed, a shoulder appearing at approximately 300 nm was also observed, which is due to the $n \rightarrow \pi^*$ transition of the C=O bonds [3]. The UV-Vis also confirmed the successful reduction of GO (RGO).

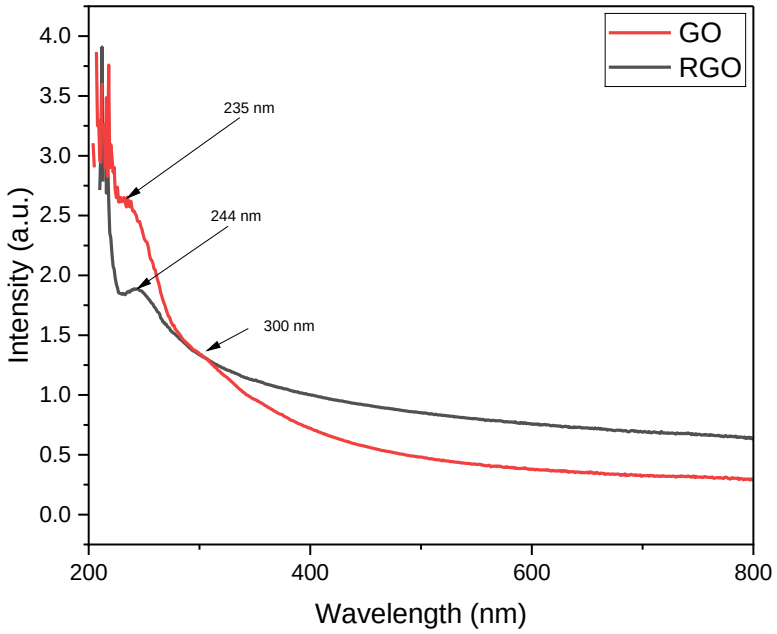

Figure 5. 1. The UV-Vis absorption spectra of graphene oxide (GO) and reduced graphene oxide (RGO).

The spectrum for RGO depicted a maximum absorption peak at approximately 244 nm, which is red-shifted from 235 nm. Besides the peak red-shifts, the shoulder peak observed in the absorption spectrum of GO disappeared in the RGO spectrum. Both the absorption red-shift from 235 nm to 244 nm and the disappearance of the shoulder peak in the RGO spectrum indicates the restoration of electronic conjugation within the graphene sheets, and an increase in the delocalized electrons [4, 5].

Plank's Law was used to estimate the energy related to the inferred electronic transition in GO and RGO given by:

$$\Delta E = hv = h\left(\frac{c}{\lambda max}\right) \tag{5.1}$$

Interpolated from the UV-Vis absorption bands, the change in energy of the light absorbed by GO and RGO was found to be 8.46 x 10^{-34} J and 8.15 x 10^{-28} J respectively. The bandgaps of both GO and RGO were estimated using Tauc's plot, equation 5.1.:

$$(ahv)^2 = A(hv - Eg) \tag{5.2}$$

Where A is the absorption constant, v is the frequency, E_g is the energy gap, h is Planck's constant and α is the absorption coefficient. The bandgaps of the as-prepared GO and RGO are 3.92 eV and 3.64 eV as shown in Figure 5.2.

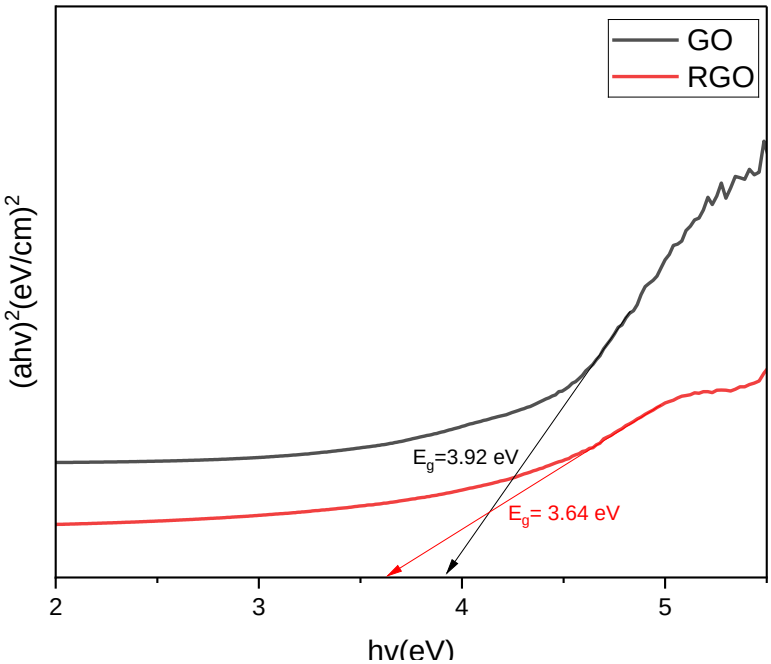

Figure 5. 2. Tauc plots of graphene oxide and reduced graphene oxide.

The decrease in bandgap from 3.92 eV to 3.64 eV is due to the removal of some oxygen containing functional groups [6]. Therefore, by adjusting its oxygen concentration, reduced graphene oxide can exhibit characteristics which are similar to those of a semi-metal or semiconductor. It is worth noting that materials displaying a bandgap of approximately 3 eV are extremely adaptable and can be applied in various fields [7].

5.2.2. Surface and structural characterization of GO and RGO

5.2.2.1 Fourier transform infrared (FT-IR) spectroscopy

The bonding interactions in GO and RGO were examined using FT-IR spectroscopy. The successful oxidation of the graphite was validated by the FT-IR spectra that was recorded and the GO spectrum that was produced (Figure 5.3). Several functional groups were

noted, including O-H, C-OH, COOH, and C-O. The O-H stretching mode is responsible for a wide peak in the IR spectra of GO that is located between 3500 cm^{-1} and 2500 cm^{-1}. The peak at approximately 1727 cm^{-1} is attributed to the carboxyl group's C=O stretch. The peak at 1625 cm^{-1} and 1039 cm^{-1} correspond to the C=C and C-OH respectively. High main peak intensities in GO indicate the presence of a significant quantity of oxygen-containing groups following the oxidation process.

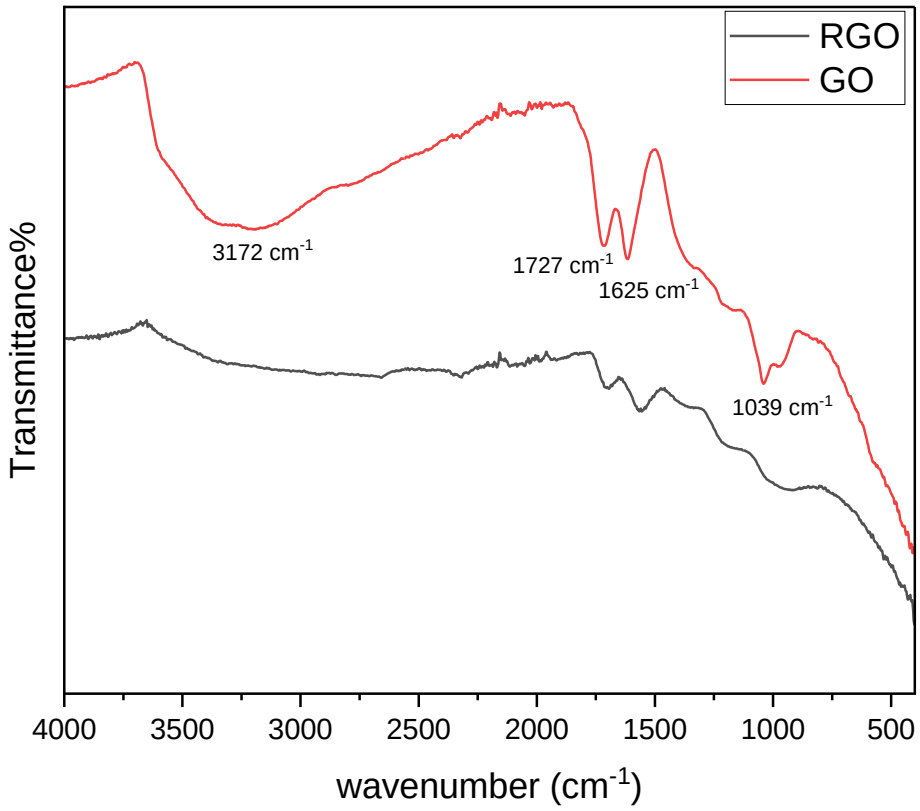

Figure 5. 3. FT-IR spectrum of GO and RGO.

FT-IR spectroscopy was also used to characterize the reduction of GO. It can be seen in Figure 5.3, all of the peak intensities corresponding to the reduced graphene oxide's oxygen-containing functionalities were lower than the graphene oxide's peak intensities, and some practically vanished. This demonstrated that ascorbic acid was able to successfully reduce graphene oxide. Some of the peaks, however, disappeared,

indicating that ascorbic acid did not completely eliminate GO and that certain functional groups that included oxygen were still intact.

5.2.2.2 Raman spectroscopy

Raman spectroscopy is one of the most effective methods for analyzing the structure and electron conjugation state of carbon materials [8]. Raman spectra for GO and RGO are shown in Figure 5.4. Both spectra depict two prominent peaks corresponding to the D and G bands. The Raman peak for D band is ascribed to the disorder crystal structure and signified the presence of sp^3 carbon. In the case of the G band, the peak is ascribed to the in-phase vibrations of ordered crystal structure which is correlated to the sp^2 carbon. The presence of the stretching C-C bond in all sp^2 carbon systems also contributes to the G vibration band [9, 10]. In the GO spectrum (Figure 5.4), the D and G bands are centered at 1355 cm^{-1} and 1600 cm^{-1}, respectively. The D and G bands in the Raman spectrum of RGO were located respectively at 1358 cm^{-1} and 1612 cm^{-1}. The D and G bands for reduced graphene oxide spectrum have slightly but significantly shifted to lower wavenumbers as compared to similar bands for graphene oxide. The slight and significant shift of those peaks is attributed to the removal of oxygen-containing functional groups experienced during the reduction process.

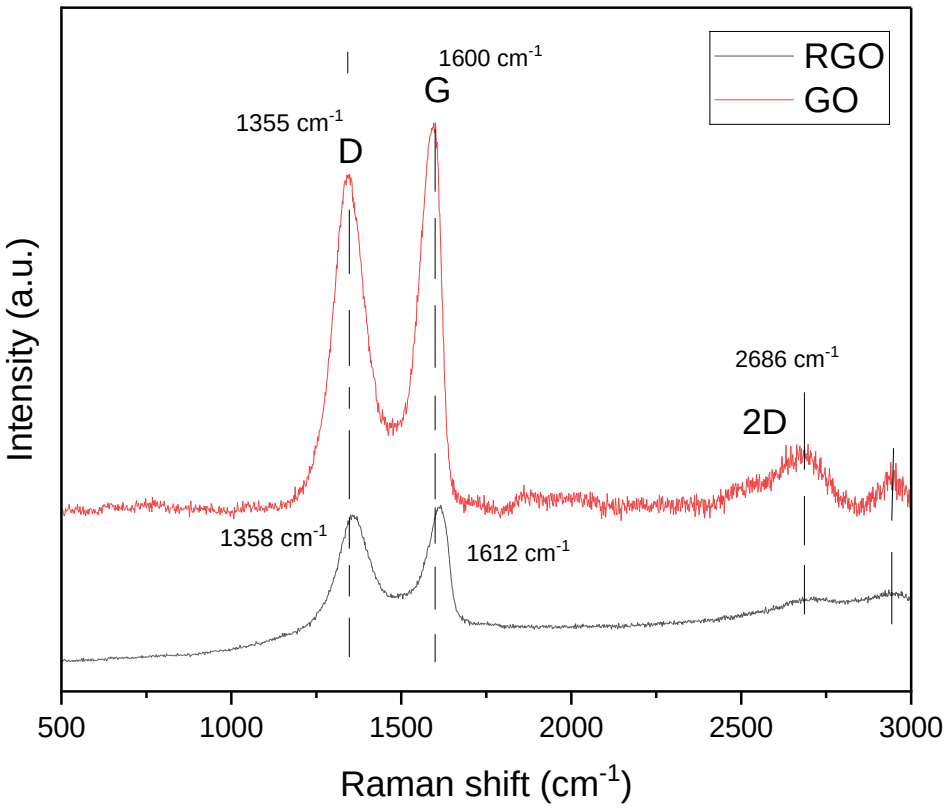

Figure 5. 4. Raman spectra for GO and RGO.

In addition to the two prominent bands observed for both GO and RGO, broad peaks attributed to a 2D bands were also observed at approximately 2686 cm^{-1} and 2696 cm^{-1}, respectively. Due to its extreme sensitivity to the stacking of graphene layers, the 2D band can be used to discern the layers of graphene, whether they are monolayer, double layer, or multilayer [11]. Structurally, the D and G bands of RGO are known to display less intense peaks than those of GO [12, 13]. Additionally, in an sp^3/sp^2 hybrid network of carbon atoms, the intensity ratio of the D band and G band (I_D/I_G) reveals the degree of oxidation and the size of sp^2 ring clusters. The (I_D/I_G) intensity ratio of GO is 0.86, while that of chemically reduced graphene oxide is 0.95. The obtained results signify that more sp^2 domains are created during the reduction process of GO, and that there is a high defect concentration in RGO than in GO [14-16].

5.2.3. X-ray diffraction analysis of GO and RGO

In order to assess the structural information of graphene oxide and reduced graphene oxide, one crucial characteristic is the separation between the layers, which plays a significant role in their XRD patterns which are different. Figure 5.5 depict the XRD patterns of graphene oxide, before reduction, and after reduction by the employment of ascorbic acid. In the XRD pattern for graphene oxide, a sharp peak appearing at 2θ value of 10.85°, corresponding to the (001) crystalline plane is observed.

The existence of the above sharp peak confirms that graphite was successfully and fully oxidized to graphene oxide. The reduction of GO by ascorbic acid led to the disappearance of the observed GO peak. A new broad peak which was not observed in the GO XRD pattern was observed at the 2θ value of 26.34°, corresponding to (002) plane. Stacking of stacks in short range order is responsible for the spreading of this RGO peak [17].

The interplanar distances (d-spacing) from the XRD diffraction major peaks of both GO and RGO are 0.86 nm and 0.35 nm, respectively. It can be seen from the values that the d-spacing for GO is higher as compared to the d-spacing for RGO. This is attributed to the existence of the oxygen functional groups such as epoxy, hydroxyl and carboxyl. The lower RGO d-spacing is evidence of the successful removal of oxygen functional groups. The obtained results agree well with other reports [18, 19, 20].

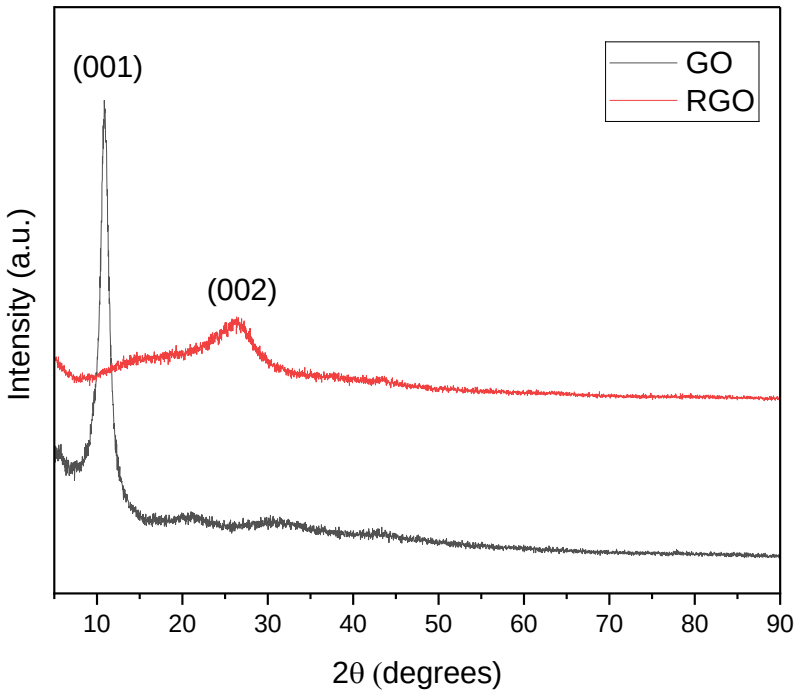

Figure 5. 5. XRD patterns of RGO and GO.

5.3. Characterization of Copper oxide (CuO), CuO-Au, CuO/RGO and CuO-Au/RGO

5.3.1. Optical properties

The UV-Vis spectroscopy was employed to investigate the optical properties of the as-synthesized copper oxide nanoparticles and the as-synthesized nanocomposites. Figure 5.6 shows the absorption spectra of the following nanocomposites: copper oxide (CuO), copper oxide-gold (CuO-Au), copper oxide/reduced graphene oxide (CuO/RGO), and copper oxide-gold/reduced graphene oxide (CuO-Au/RGO). All spectra depict a sharp peak with a maximum absorption appearing at approximately 253 nm, which is the characteristic band of CuO. The observed peaks are blue shifted as compared to bulk CuO. The presence of the CuO peak which is blue shifted, is due to quantum confinement effect by the reduced size of nanoparticles. The appearance of a single sharp band in the spectrum of CuO is an indication of the successful formation of mainly CuO, instead of a mixture of CuO and Cu_2O [21, 22].

It was noted that the absorption curves for both CuO/RGO and CuO-Au/RGO nanocomposites depicted a small, but significant shift to higher wavelength as compared to those for CuO and CuO-Au nanomaterials. The small, but significant shift is attributed

to the extension of conjugation in the CuO/RGO and CuO-Au/RGO nanocomposites [23]. In the absorption spectrum of CuO-Au/RGO nanocomposite (inset), the appearance of a broad band ranging from approximately 480 - 850 nm is observed. The broad band is attributed to the presence of gold nanoparticles in the as-synthesized nanocomposites [24].

The optical bandgap energies (E_g, eV) of CuO nanoparticles, CuO-Au, CuO/RGO and CuO-Au/RGO nanocomposites were determined from the absorption spectra using equation 5.1. Figure 5.6b shows the Tauc plots of CuO nanoparticles, CuO-Au, CuO/RGO and CuO-Au/RGO nanocomposites. The optical bandgap energies for CuO nanoparticles and CuO-Au nanocomposite were recorded as 3.33 and 3.41 eV respectively. The observed bandgap of CuO nanoparticles using the Tauc relation was higher than the equivalent value for bulk CuO (2.1 eV) [25]. However, upon the addition of CuO and CuO-Au nanomaterials on the RGO surface to produce CuO/RGO and CuO-Au/RGO nanocomposites, the bandgaps were reduced to 3.29 and 3.31 eV respectively (Figure 5.6b). Table 5.1 shows the absorption edge and band gap values for CuO, CuO-Au, CuO/RGO and CuO-Au/RGO nanocomposites. This demonstrates how aggregation and composite production cause bandgap to decrease as particle size increases. Photons only become absorbed in semiconductor materials when their lowest energy, or bandgap energy (E_g), is high enough to drive an electron from the valence band to the conducting band. The bandgap of CuO/RGO and CuO-Au/RGO decreases as a result of the optical bandgap shifting to a higher wavelength due to the rise in surface charge between CuO, CuO-Au and RGO [26].

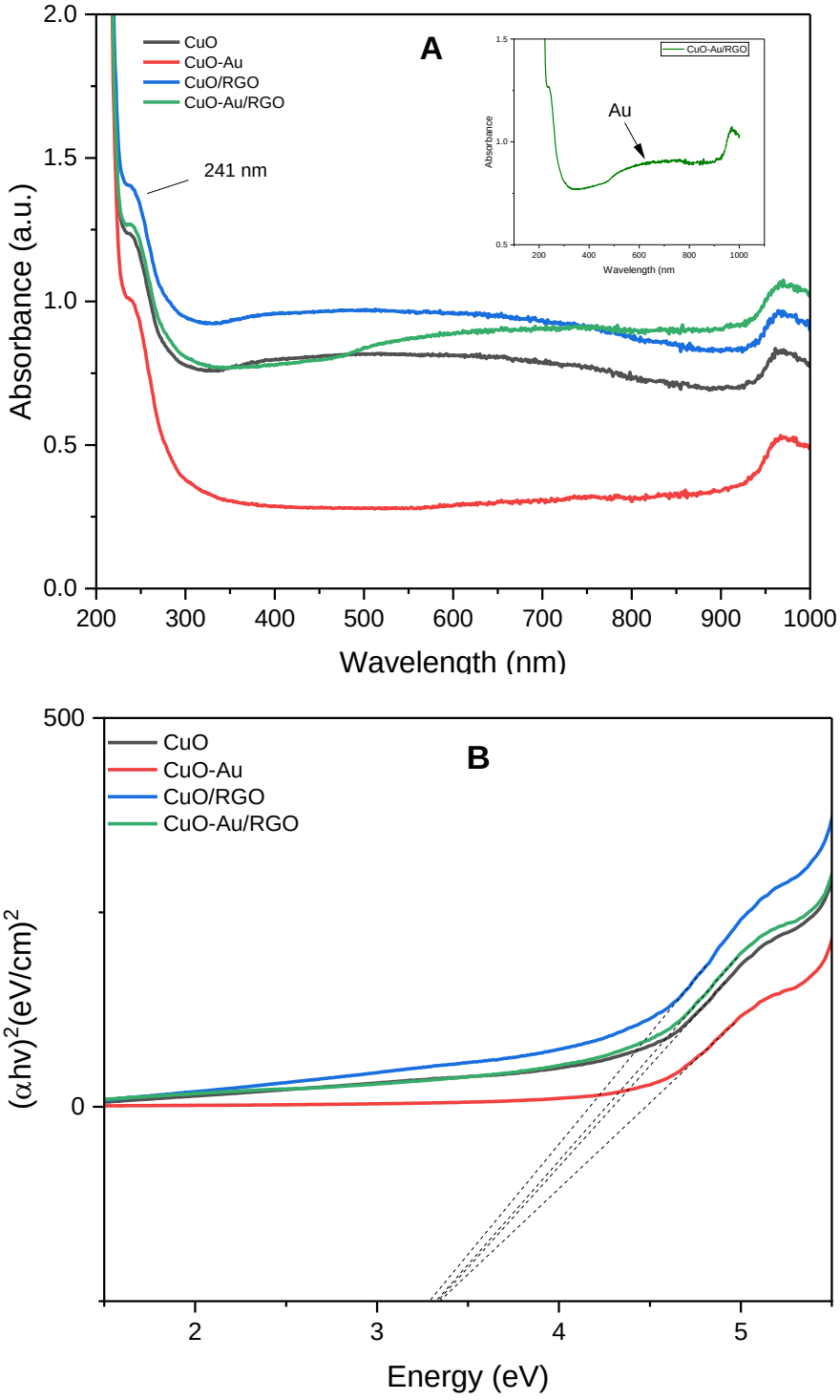

Figure 5. 6. Absorption spectra (A) and Tauc plots (B) of CuO, CuO-Au, CuO/RGO and CuO-Au/RGO nanomaterials.

Table 5.1. The absorption and band edges from the UV-Vis absorption spectra of CuO, CuO-Au, CuO/RGO and CuO-Au/RGO nanomaterials.

Sample	Absorption edge (nm)	Band Gap (eV)
CuO	239	3.33
CuO-Au	239	3.41
CuO-RGO	241	3.29
CuO-Au/RGO	241	3.31

5.3.2. The Spectroscopy Studies of CuO, CuO-Au, CuO/RGO and CuO-Au/RGO

5.3.2.1. Fourier transform infrared (FT-IR) spectroscopy

The FT-IR spectra of the as-synthesized CuO, CuO/RGO and CuO-Au/RGO were acquired in order to identify the different functional groups. The widened peak located at around 3500 cm^{-1} in the CuO FT-IR spectra is caused by O-H stretching vibrations. CuO, CuO/RGO, CuO-Au and CuO-Au/RGO's absorption peak at 487, 510 and 607 cm^{-1} are caused by Cu-O stretching vibration. The obtained results are in agreement with previously published report by Dehaj and Mohiabadi [27].

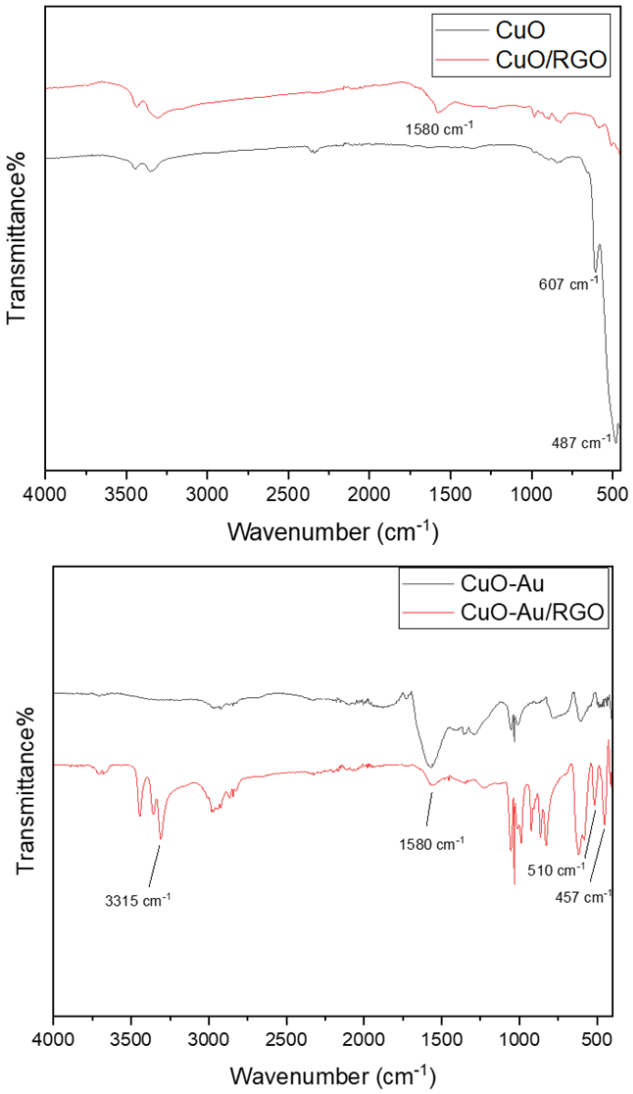

Figure 5. 7. FT-IR spectra of CuO (a), CuO/RGO (a), CuO-Au (b) and CuO-Au/RGO (b) nanocomposites.

The signal at 882 cm^{-1}, which confirms the effective synthesis of the CuO-Au/RGO nanocomposite, is caused by the Cu-OH vibration [28]. However, the peak at roughly 1580 cm^{-1}, which indicates the presence of RGO in CuO/RGO and CuO-Au/RGO nanocomposites.

5.3.2.2 Raman spectroscopy

The CuO, CuO-Au, CuO/RGO, and CuO-Au/RGO Raman spectra are shown in Figure 5.8 below. Graphene's Raman spectra is typically characterized by two primary vibrational modes, G and D. The hexagonal sp^2 carbon atoms' E_{2g} phonon first-order scattering gives birth to the G band, while the breathing mode of k-point phonons of A_{1g} symmetry causes the D band [29].

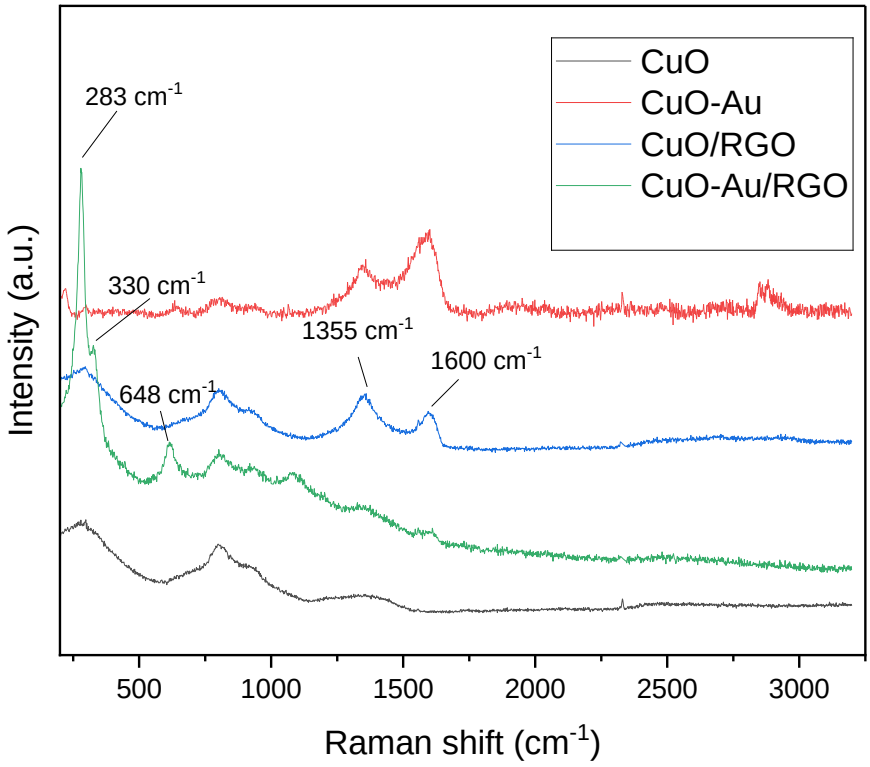

Figure 5. 8. Raman spectra of CuO, CuO-Au, CuO/RGO and CuO-Au/RGO nanocomposites.

In the spectral range that was chosen for CuO/RGO nanocomposites, two significant peaks that correspond to the G band (~ 1600 cm^{-1}) and D band (~ 1355 cm^{-1}) are clearly visible. The I_D/I_G ratio for CuO/RGO and CuO-Au/RGO nanocomposites are 1.11 and 1.63 respectively. Both show an increased I_D/I_G ratio related to that of GO (~0.86) and RGO (~ 0.95), indicating a reduction in the reduced graphene oxide spatially ordered

crystal structure and in-plane sp^2 domain size [30]. The high I_D/I_G ratio value suggests that the as-prepared RGO contains a significant number of defects. The monoclinic CuO structure is responsible for three optical Raman bands in the Raman spectra of the CuO/RGO and CuO-Au/RGO nanocomposites, which are situated at 283 cm^{-1} (A_g), 330 cm^{-1} (Bg), and 648 cm^{-1} (B_{2g}). The A_g and B_g modes of the monoclinic CuO structure, respectively, indicate the movement of oxygen atoms in the b-direction and perpendicular to the b-axis.

5.3.3. The X-ray analysis of CuO, CuO-Au, CuO/RGO and CuO-Au/RGO nanocomposite

The X-ray diffraction patterns of the as-synthesized CuO, CuO-Au, CuO/RGO and CuO-Au/RGO nanocomposites are shown in Figure 5.9. In the XRD pattern for CuO, all the diffraction peaks are similar and indexed according to the standard JCPDS data (Card No. 45-0937) for monoclinic CuO. No additional peaks due to impurities presence of any secondary copper (Cu) or cuprous oxide (Cu_2O) phases were observed, showing the single phase CuO formation. The obtained peaks for CuO are broad due to quantum size effect. It is known from literature that the broadness of XRD peaks signify that the as-synthesized nanomaterials are small in size. The typical diffraction peaks of the CuO nanoparticles are located at 2θ = 32.7°, 35.7°, 38.9°, 48.9°,53.7°, 58.4°, 61.7°, 66.3° and 68.2°. These peaks correspond to the (110), (002), (111), (-202), (020), (202), (-113), (-311), and (220) planes of CuO that have a monoclinic structure, respectively. According to the XRD pattern of CuO-Au, the Au peaks are observed at 2θ=42.3° and 43.3° corresponding to (111) and (200) crystal planes of face-centered cubic form of gold. The XRD patterns for both CuO/RGO and CuO-Au/RGO depicted a small but significant peak located at 2θ = 25.3°, corresponds to (002) plane. The presence of this crucial peak result from water molecules and oxygenated functional groups being inserted into the graphene layer [31].

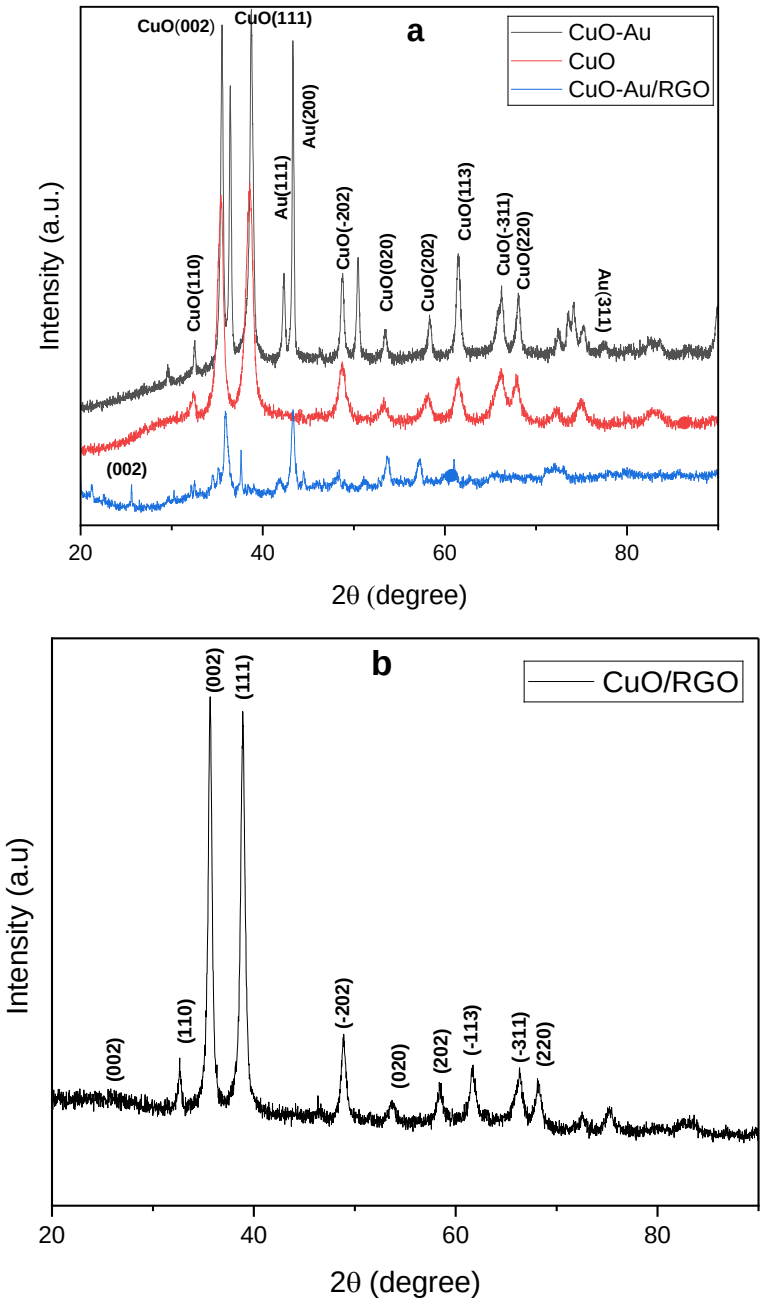

Figure 5. 9. The XRD patterns of of (a) CuO, CuO-Au, CuO-Au/RGO, and (b) CuO/RGO nanocomposites.

5.3.4. Microscopy and Elemental analysis of CuO, CuO-Au, CuO/RGO and CuO-Au/ RGO

5.3.4.1 Transmission electron microscopy (TEM) and Energy-dispersive X-ray spectroscopy (EDX)

Transmission electron microscopy (TEM) examination was used to determine the size and shape of the CuO, CuO-Au, CuO/RGO and CuO-Au/RGO nanocomposites (Figure 5.10). The TEM images of CuO and CuO/RGO nanoparticles (Figure 5.10(a)) depict spherical-like shaped nanoparticles, with some signs of agglomeration. Both CuO and CuO/RGO have the average diameter of 46.53 nm and 28.33 nm respectively. Evidence of spherical nanoparticles, with an average diameter of 11.77 nm was also observed in the TEM image of CuO-Au as shown in Figure 5.10(b). The software used for the determination of nanoparticles is imagej. Signs of aggregation was also observed in the TEM image.

The TEM images of both CuO/RGO and CuO-Au/RGO depict the uniform dispersion of spherical CuO and CuO-Au on the graphene oxide surface as seen in Figures 5.10 (c) and (d). However, the above is clearly seen in the TEM image of CuO-Au/RGO nanocomposite. The nanoparticles, which are uniformly decorated on the graphene sheet as indicate above are estimated to have an average diameter of 16.09 nm.

In comparison between the TEM images of CuO-Au (Figure 5.10 (c)) and CuO-Au/RGO (Figure 5.10 (d)), CuO-Au nanocomposite shows higher level of aggregation compared to CuO-Au/RGO nanocomposite. The stabilizing effect of the functional groups on the reduced graphene oxide is associated with the reduction of aggregation. Graphene oxide has been repeatedly reported to possess a variety of functional groups such as carbonyl, carboxyl, hydroxyl, alkoxy, and epoxy groups. The conjugated carbon skeleton's surface is mostly home to hydroxyl and epoxy groups, which are largely eliminated during the chemical reduction process with ascorbic acid [32]. However, the edge functionalities (-COOH, -C=O, and -OH) remain in place and could serve as locations for metal or/and metal oxide nanoparticle stabilization.

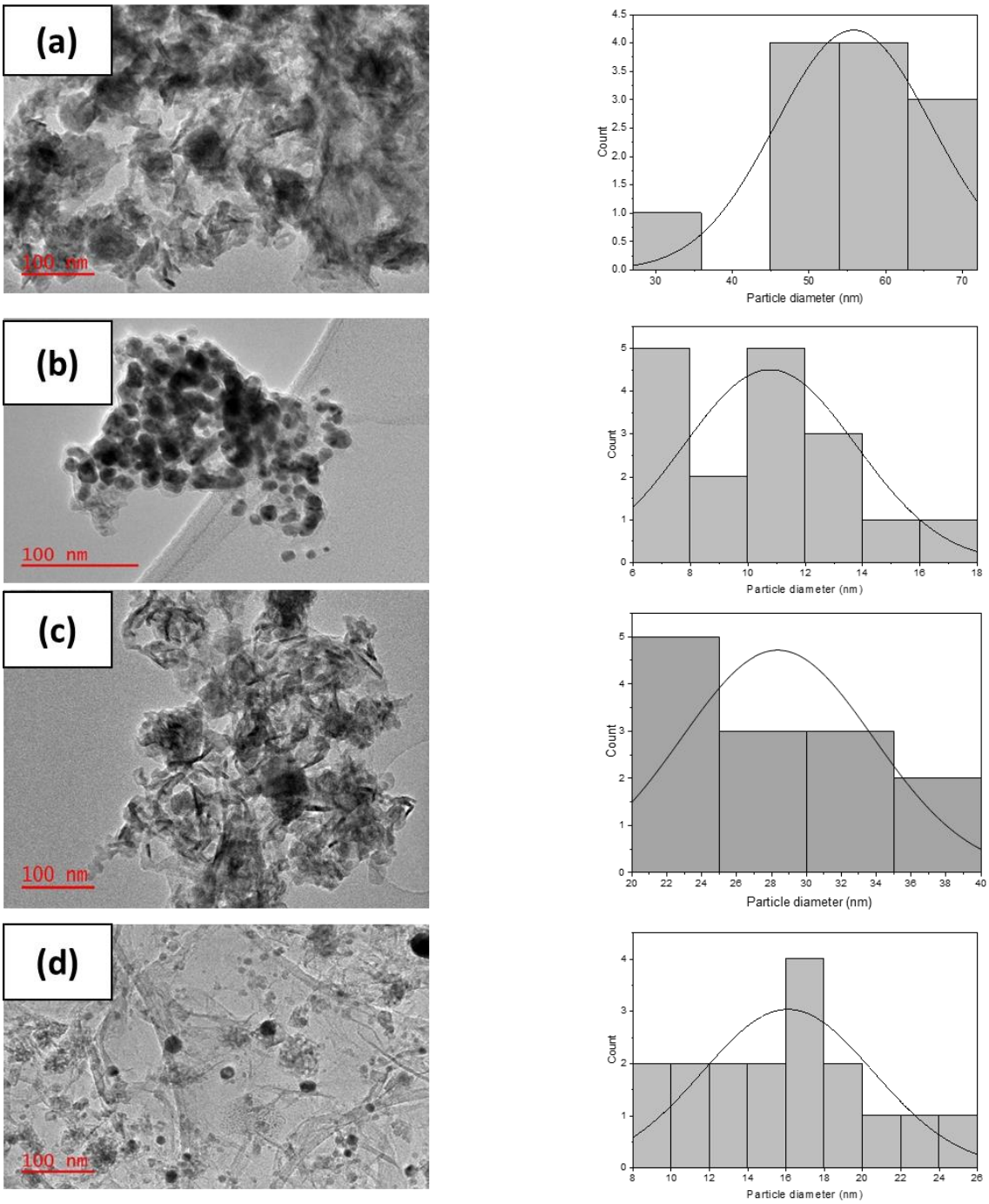

Figure 5. 10. TEM images and size distributions of (a) CuO, (b) CuO-Au, (c) CuO/RGO and (d) CuO-Au/RGO at 100 nm.

The elemental analysis for CuO, CuO-Au, CuO/RGO and CuO-Au/RGO nanocomposites (Figure 5.11) were investigated using the energy-dispersive X-ray (EDX) spectrometer. The EDX spectra of CuO and CuO/RGO represented in Figures 5.11 (a) and (b), respectively, confirm the presence of elemental copper (Cu) and oxygen (O) signals. Except the presence of the carbon (C) peak observed in all EDX spectra, no peaks due to impurities were observed. The carbon peak emanates from the grids used, where it was employed during coating process. These results confirm that the as-synthesized nanomaterials consist of highly pure copper oxide nanoparticles. The presence of a gold (Au) peak, adding to the already existing Cu, O and C peaks, was observed in the EDX spectrum of CuO-Au/RGO nanocomposites (Figure 5.11 (c)). These results agree well with the XRD results, displaying the successful formation CuO-Au nanocomposite decorated RGO.

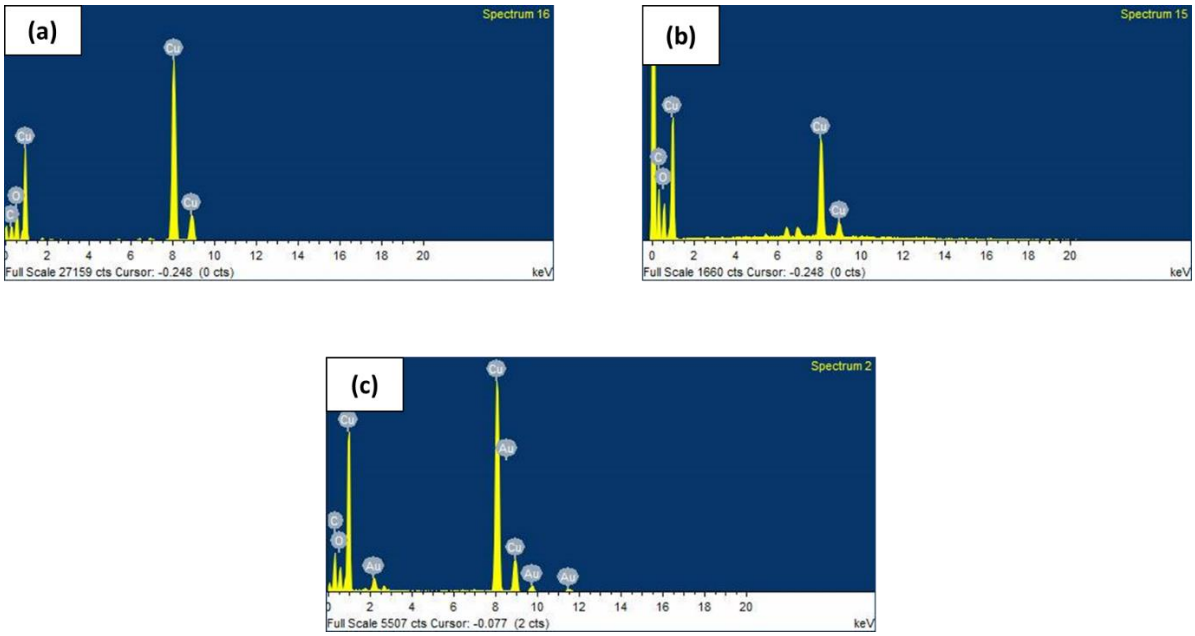

Figure 5. 11. The energy-dispersice X-ray of (a) CuO, (b) CuO/RGO and (c) CuO-Au/RGO nanocomposites.

5.4. Characterization of CuS nanoparticles, CuS-Au, CuS/RGO and CuS-Au/RGO nanocomposites

5.4.1. Optical properties

There are several reports on the stable phases of copper sulfide, ranging from sulfur-rich covellite (CuS) to chalcocite (Cu_2S). Each stable phase has unique optical characteristics. The characteristic near-IR absorption band of covellite (CuS), for example, diminishes with increasing sulfur content, progressing from covellite to degenite ($Cu_{1.8}S$) to djurleite ($Cu_{1.9}S$) [33]. Figure 5.12 shows absorption spectra of CuS nanoparticles, CuS-Au and CuS/RGO nanocomposites.

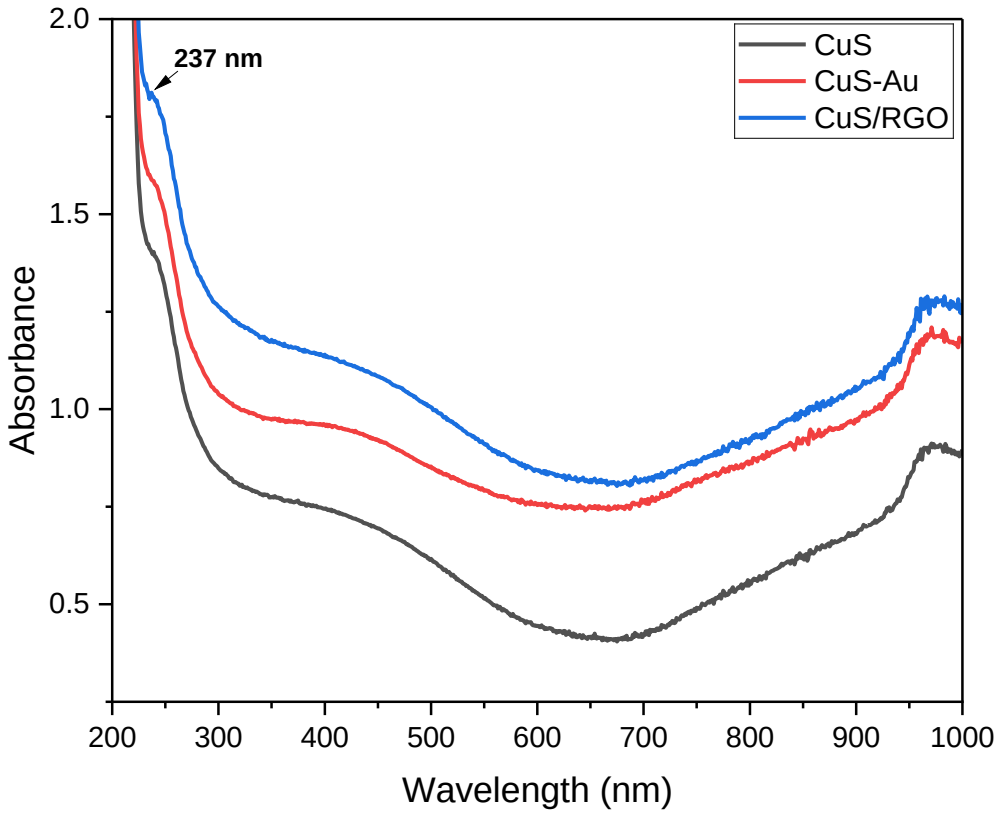

Figure 5. 12. Absorption spectra of CuS, CuS-Au and CuS/RGO nanocomposites.

CuS has a blue-shifted absorption spectrum compared to bulk (1022 nm), which is caused by the quantum confinement phenomenon [34-36]. The presence of an intense LSPR

absorption in the NIR was confirmed by UV-Vis-NIR spectra, with a peak located in the anticipated 900-1000 nm region (Figure 5.13). Interestingly, Luther et al. previously observed a little red shift in the LSPR absorption in response to the decrease in NP size [37]. Figure 5.13. Shows the Tauc plots for CuS, CuS-Au and CuS/RGO nanocomposite. The bandgaps were estimated using equation 5.2. The bandgap of CuS, CuS-Au and CuS/RGO nanocomposite are 3.75, 3.59 and 3.39 eV respectively.

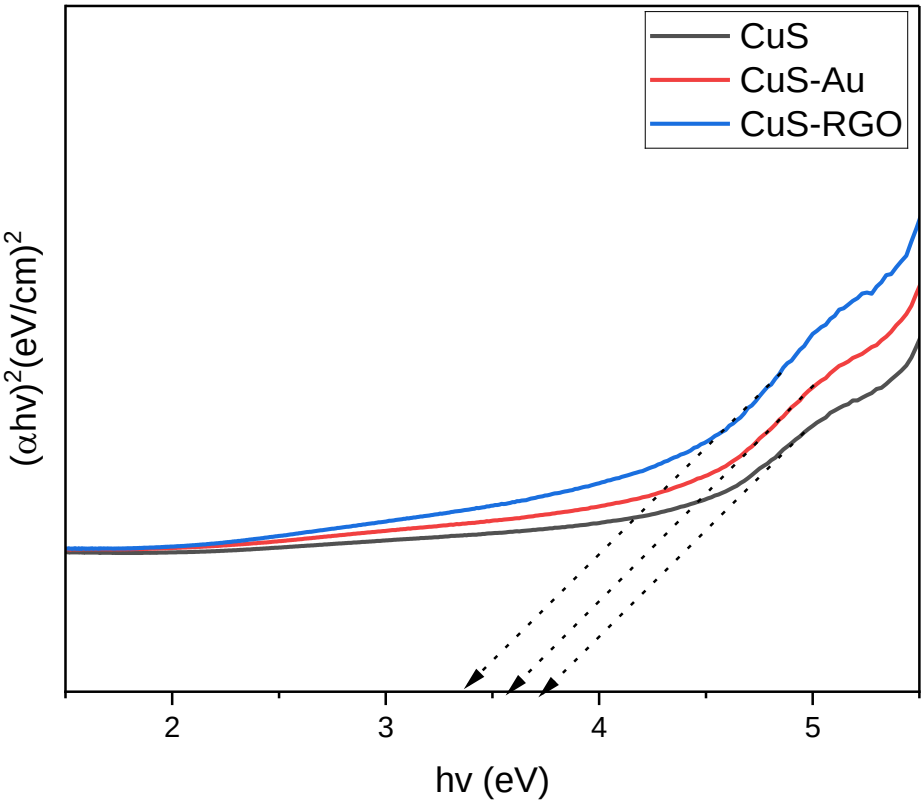

Figure 5. 13. Tauc plots of CuS, CuS-Au and CuS/RGO.

The absorption band edge and band gap values for CuS, CuS-Au and CuS/RGO nanocomposite are demonstrated in Table 5.2.

Table 5.2. The absorption and band edges from the UV-Vis absorption spectra of CuS, CuS-Au and CuS/RGO.

Sample	Absorption edge (nm)	Band Gap (eV)
CuS	971	3.75
CuS-Au	973	3.59
CuS-RGO	974	3.39

5.4.2. Raman spectroscopy analysis of CuS, CuS-Au, CuS-RGO and CuS-Au-RGO

Figure 5.14 depicts the Raman spectra of the CuS nanoparticles, CuS-Au and CuS/RGO nanocomposites. In the Raman spectrum of CuS, a strong and sharp peak appearing at 475 cm^{-1}, corresponding to the A_{1g} mode is observed [38]. Evidence of the presence of CuS peak mode was also observed in the Raman spectra of both CuS-Au, CuS/RGO, CuS-Au/RGO nanocomposites. The presence of CuS peak signifies the successful assembly between CuS and Au, and CuS and RGO. The Raman spectra of CuS/RGO showed two separate peaks in addition to the CuS peak, which were caused by the D and G bands, which are positioned at 1348 and 1598 cm-1, respectively. The existence of CuS peak in the Raman spectrum of CuS/RGO, which matches that of the original CuS, suggest that the lattice atoms of CuS were aligned in the periodic array. The hexagonal graphitic layer's flaws and disorganization are responsible for the D band. The vibration of carbon atoms with sp^2 bonds in a two-dimensional hexagonal lattice is responsible for the G band [39, 40].

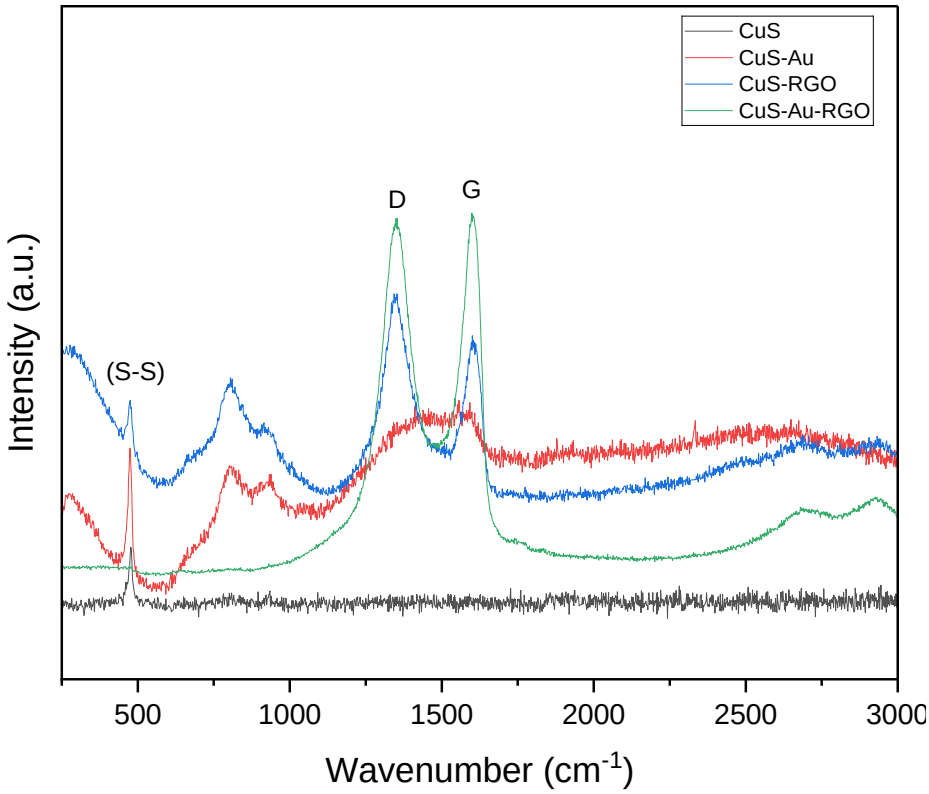

Figure 5. 14. Raman spectra of CuS, CuS-Au and CuS/RGO.

The I_D/I_G ratio was used to measure structural disorder for CuS-RGO. I_D/I_G ratio for CuS-RGO was found to be 1.19 which is slightly above that of RGO (~0.95), indicating a higher defect concentration and reduction of in-plane sp^2 domain size and spatially ordered crystal structure of RGO.

5.4.3 The X-ray analysis of CuS, CuS-Au and CuS/RGO

X-ray diffraction was used to analyze the crystallinity and phase composition of the as-synthesized CuS, CuS-Au and Cu/-RGO nanocomposite (Figure 5.15). The diffraction peaks in the patterns of both CuS and CuS/RGO belong to the hexagonal crystal system of CuS (JCPDS-06-0464) [41]. The distinctive diffraction peaks of pure CuS, appearing at 27.4, 27.6, 29.4, 31.5, 32.5, 47.8, 52.6, and 59.5, correspond to the (100), (101), (102), (103), (106), (110), (108) and (116) planes, respectively. CuS crystalline with a covellite phase is confirmed by the obtained results.

No traces of CuO peaks were observed. This is a confirmation that the as-synthesized nanomaterial is pure CuS. The peaks from 15-22 degrees are due to impurities, no wonder they are not indexed. All the characteristic peaks due to CuS were also observed in the XRD pattern for CuS/RGO. This is an indication that RGO was successfully decorated with CuS nanoparticles. The existence of a small but significant peak at 2θ = 25.3°, corresponding to (002) plane, further confirms the presence of RGO in the product. In addition to the CuS peaks, the XRD pattern for CuS-Au nanocomposite displayed four diffraction peaks appearing at 38.98°, 44.98°, 65.24°, and 78.15° corresponding to (111), (200), (220) and (311). The four peaks correspond to the distinctive Au peaks and are in good agreement with JCPDS-04-0784 [42].

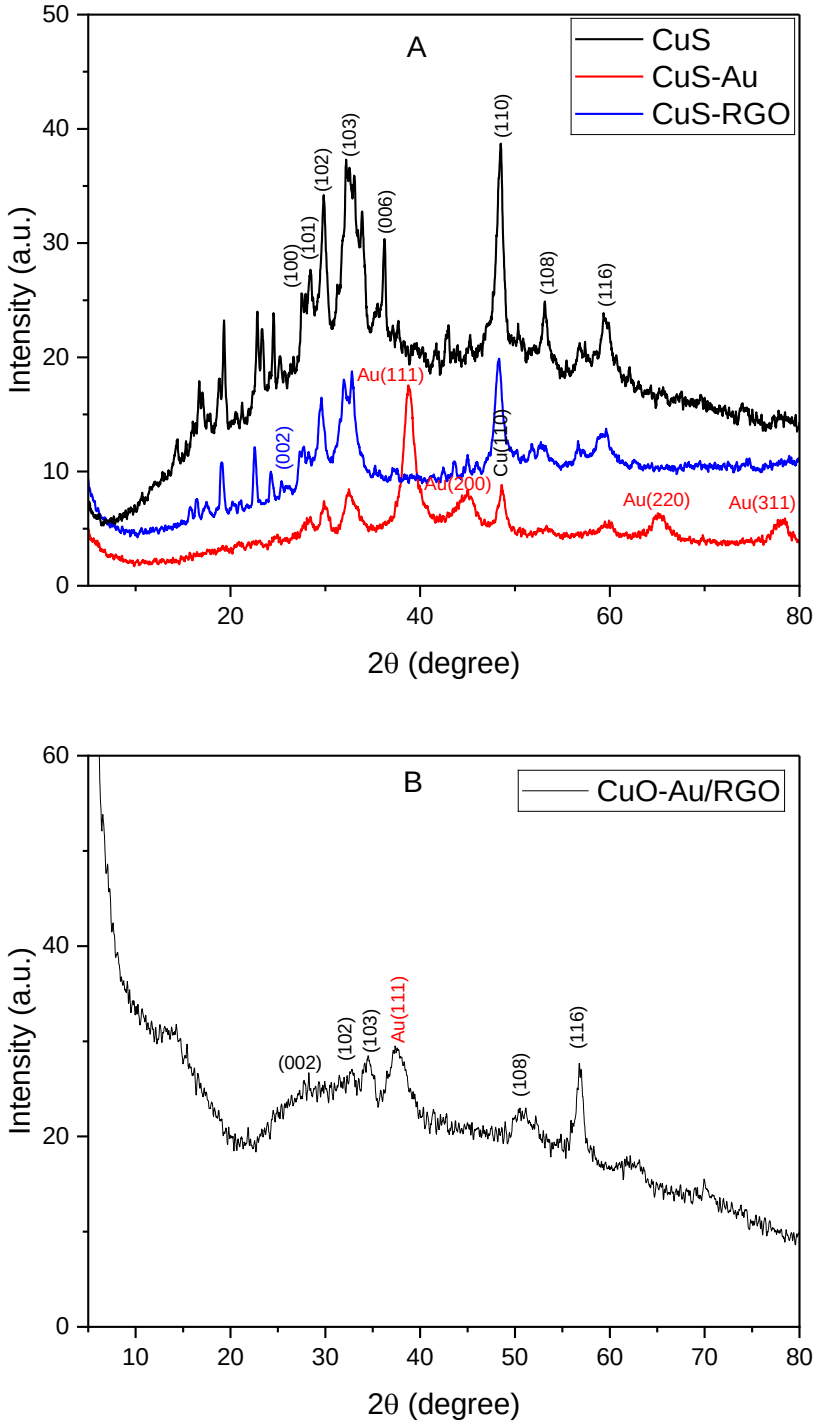

Figure 5. 15. XRD pattern of (a) CuS, CuS-Au, CuS/RGO and (b) CuS-Au/RGO.

5.4.4. Microscopy and Elemental analysis of CuS, CuS-Au, CuS/RGO and CuS-Au/RGO

TEM micrographs of CuS, CuS-Au and CuS/RGO nanocomposite synthesized are displayed in Figure 5.16, together with their corresponding particle-size distribution histograms. It is evident from the CuS TEM image (Figure 5.16a) that the particles have a homogeneous, spherical-like shaped morphology with an average diameter of 18 nm. Signs of particles aggregation were also observed. Figure 5.16b shows TEM images of CuS decorated with Au nanoparticles. It is easier to distinguish between the two heterodimer nanoparticles because of the darker appearance of the gold nanoparticles on the surface of CuS nanoparticles as compared to the CuS surface due to the higher atomic number of gold (Figure 5.16b). According to the corresponding particle distribution, the Au-CuS nanoparticles had a mean diameter ranging from 10.0 nm to 30.0 nm and average diameter of 17.67 nm. Figure 5.16c shows TEM images of the loaded CuS on RGO sheets. The particle diameters range from 15 to 45 nm, with an average diameter of 31.84 nm. The CuS cluster were dispersed on both sides of RGO's sheet-like structure. The size distribution for the prepared CuS-Au/RGO nanocomposite was evaluated between 15 and 45 nm (Figure 5.16d). The As-synthesized nanocomposite has a measured average diameter of 32.66 nm.

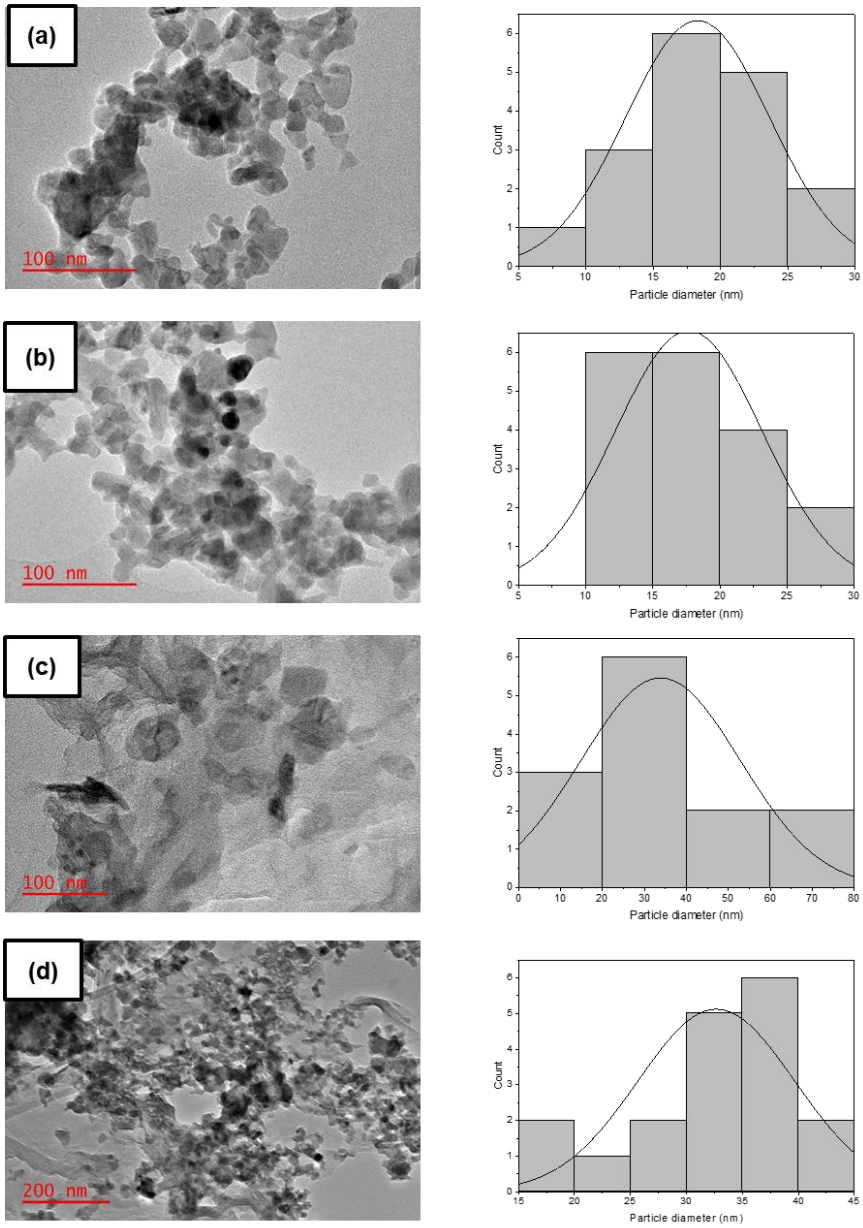

Figure 5.16. TEM images and size distribution of CuS, CuS-Au, CuS/RGO and CuS-Au/RGO nanocomposite.

EDX analysis is displayed in Figure 5.17 to verify the presence of the CuS shell and Au NPs. The successful growth of CuS nanoparticles was indicated by the strong S and Cu signals that were observed (Figure 5.17a). Figure 5.17b shows a strong Au signal, further confirming the presence of Au on the surface of CuS nanoparticles.

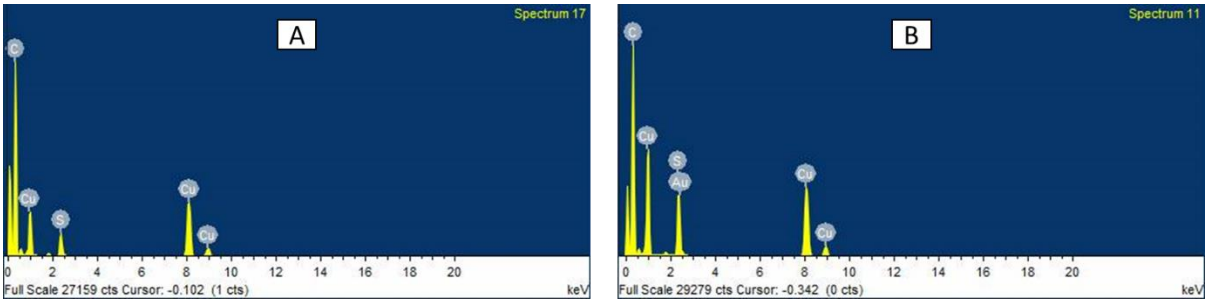

Figure 5. 17. EDX spectra of (a) CuS and (b) CuS-Au nanoparticles.

REFERENCES

1. Zaaba, N.I. et al. (2017) 'Synthesis of Graphene Oxide using Modified Hummers Method: Solvent Influence,' Procedia Engineering, 184, pp. 469-477.
2. De Silva, K.K.H. et al. (2018) 'Progress of reduction of graphene oxide by ascorbic acid,' Applied Surface Science (Print), 447, pp. 338-346.
3. Marcano, D.C. et al. (2010) 'Improved synthesis of graphene oxide,' ACS Nano, 4(8), pp. 4806-4814.
4. Gurunathan, S. et al. (2013) 'Microbial reduction of graphene oxide by Escherichia coli: A green chemistry approach,' Colloids and Surfaces. B, Biointerfaces, 102, pp. 772-777.
5. Li, D. et al. (2008c) 'Processable aqueous dispersions of graphene nanosheets,' Nature Nanotechnology, 3(2), pp. 101-105.
6. Mathkar, A. et al. (2012) 'Controlled, stepwise reduction and band gap manipulation of graphene oxide,' the Journal of Physical Chemistry Letters, 3(8), pp. 986-991.
7. Granqvist, C.G. (2007) 'Transparent conductors as solar energy materials: A panoramic review,' Solar Energy Materials & Solar Cells/Solar Energy Materials and Solar Cells, 91(17), pp. 1529-1598.
8. Tuinstra, F. and Koenig, J.L. (1970) 'Raman spectrum of graphite,' the Journal of Chemical Physics, 53(3), pp. 1126-1130.

9. Kudin, K.N. et al. (2007) ‘Raman spectra of graphite oxide and functionalized graphene sheets,’ Nano Letters (Print), 8(1), pp. 36-41.
10. Ferrari, A.C. and Robertson, J. (2000) ‘Interpretation of Raman spectra of disordered and amorphous carbon,’ Physical Review. B, Condensed Matter, 61(20), pp. 14095-14107
11. Thakur, S. and Karak, N. (2012) ‘Green reduction of graphene oxide by aqueous phytoextracts,’ Carbon, 50(14), pp. 5331-5339.
12. Lee, A.Y. et al. (2020) ‘Raman study of D* band in graphene oxide and its correlation with reduction,’ Applied Surface Science, 536, p. 147990.
13. Dresselhaus, M.S. et al. (2010) ‘Perspectives on Carbon Nanotubes and Graphene Raman Spectroscopy,’ Nano Letters, 10(3), pp. 751-758.
14. Gurunathan, S. et al. (2012) ‘Oxidative stress-mediated antibacterial activity of graphene oxide and reduced graphene oxide in Pseudomonas aeruginosa,’ International Journal of Nanomedicine, pp. 5901.
15. Sutar, D.S. et al. (2012) ‘Spectroscopic studies of large sheets of graphene oxide and reduced graphene oxide monolayers prepared by Langmuir-Blodgett technique,’ Thin Solid Films (Print), 520(18), pp. 5991-5996.
16. Yang, D. et al. (2009) ‘Chemical analysis of graphene oxide films after heat and chemical treatments by X-ray photoelectron and Micro-Raman spectroscopy,’ Carbon, 47(1), pp. 145-152.
17. Yang, Y. (2015) ‘One-pot synthesis of reduced graphene oxide/zinc sulfide nanocomposite at room temperature for simultaneous determination of ascorbic acid, dopamine and uric acid,’ Sensors and Actuators. B, Chemical, 221, pp. 750-759.
18. Habte, A.T. and Ayele, D.W. (2019) ‘Synthesis and Characterization of Reduced Graphene Oxide (rGO) Started from Graphene Oxide (GO) Using the Tour Method with Different Parameters,’ Advances in Materials Science and Engineering, 2019, pp. 1-9.
19. Zhuo, Q. et al. (2013) ‘Large-scale synthesis of graphene by the reduction of graphene oxide at room temperature using metal nanoparticles as catalyst,’ Carbon, 52, pp. 559-564.

20. Krishnamoorthy, K. et al. (2013) ‘The chemical and structural analysis of graphene oxide with different degrees of oxidation,’ Carbon, 53, pp. 38-49.
21. Abboud, Y. et al. (2013b) ‘Biosynthesis, characterization and antimicrobial activity of copper oxide nanoparticles (CONPs) produced using brown alga extract (Bifurcaria bifurcata),’ Applied Nanoscience, 4(5), pp. 571-576.
22. Rahman, A. et al. (2010b) ‘SYNTHESIS OF COPPER OXIDE NANO PARTICLES BY USING Phormidium cyanobacterium,’ Indonesian Journal of Chemistry, 9(3), pp. 355-360.
23. Dutta, S. et al. (2016b) ‘Highly efficient photocatalytic activity of CuO quantum dot decorated rGO nanocomposites,’ Journal of Physics. D, Applied Physics, 49(31), pp. 315107.
24. Dhara, K. et al. (2015b) ‘Single step synthesis of Au-CuO nanoparticles decorated reduced graphene oxide for high performance disposable nonenzymatic glucose sensor,’ Journal of Electroanalytical Chemistry, 743, pp. 1-9.
25. Bhaumik, A. et al. (2014) ‘Significant enhancement of optical absorption through nano-structuring of copper based oxide semiconductors: possible future materials for solar energy applications,’ Physical Chemistry Chemical Physics/PCCP. Physical Chemistry Chemical Physics, 16(22), pp. 11054-11066.
26. Dhineshbabu, N.R. et al. (2015) ‘Study of structural and optical properties of cupric oxide nanoparticles,’ Applied Nanoscience (Heidelberg. Internet), 6(6), pp. 933-939.
27. Dehaj, M.S. and Mohiabadi, M.Z. (2019) ‘Experimental study of water-based CuO nanofluid flow in heat pipe solar collector,’ Journal of Thermal Analysis and Calorimetry, 137(6), pp. 2061-2072.
28. Alves, D.C.B. et al. (2015) ‘Copper nanoparticles stabilized by reduced graphene oxide for CO2 reduction reaction,’ Materials for Renewable and Sustainable Energy, 4(1).
29. Ferrari, A.C. et al. (2006) ‘Raman spectrum of graphene and graphene layers,’ Physical Review Letters, 97(18).

30. Gao, H. et al. (2012) ‘High-performance asymmetric supercapacitor based on graphene hydrogel and nanostructured MnO2,’ ACS applied materials & interfaces, 4(5), pp.2801-2810.
31. Jamatia, R. et al. (2017) ‘Graphite oxide: a metal free highly efficient carbocatalyst for the synthesis of 1,5-benzodiazepines under room temperature and solvent free heating conditions,’ Green Chemistry (Print), 19(6), pp. 1576-1585.
32. Zainuddin, M.F. et al. (2018) ‘Synthesis of reduced Graphene Oxide (rGO) using different treatments of Graphene Oxide (GO),’ IOP Conference Series: Materials Science and Engineering, 358, pp. 012046.
33. Leidinger, P. et al. (2011) ‘Nanoscale copper sulfide hollow spheres with phase-engineered composition: covellite (CuS), digenite (Cu1.8S), chalcocite (Cu2S),’ Nanoscale, 3(6), pp. 2544.
34. Serrano, T. and Gómez, I. (2014) ‘One pot synthesis of PbS/Cu2S core-shell nanoparticles and their optical properties,’ Revista mexicana de física, 60(1), pp.14-21.
35. Zaini, M.S. et al. (2020) ‘Quantum Confinement effect and photoenhancement of photoluminescence of PBS and PBS/MNS quantum dots,’ Applied Sciences, 10(18), pp. 6282.
36. Sanderson, W.M. et al. (2020) ‘Excitation Energy Dependence of Photoluminescence Quantum Yields in Semiconductor Nanomaterials with Varying Dimensionalities,’ ˜the œJournal of Physical Chemistry Letters, 11(9), pp. 3249-3256.
37. Luther, J.M. et al. (2011b) ‘Localized surface plasmon resonances arising from free carriers in doped quantum dots,’ Nature Materials, 10(5), pp. 361-366.
38. Li, X. et al. (2018) ‘CuS nanoplatelets arrays grown on graphene nanosheets as advanced electrode materials for supercapacitor applications,’ Journal of Materials Science & Technology, 34(12), pp. 2342-2349.
39. Tao, H.C. et al. (2014) ‘One-pot facile synthesis of CuS/graphene composite as anode materials for lithium ion batteries,’ Journal of Physics and Chemistry of Solids, 75(11), pp.1205-1209.

40. Ling, F. et al. (2013) ‘Reduced Graphene Oxide Wrapped FeS Nanocomposite for Lithium-Ion Battery Anode with Improved Performance,’ ACS Applied Materials & Interfaces, 5(11), pp. 5330-5335.
41. Liu, H. et al. (2018) ‘CuS/MnS composite hexagonal nanosheet clusters: Synthesis and enhanced pseudocapacitive properties,’ Electrochimica Acta, 271, pp. 425-432.
42. Zhang, X. et al. (2016) ‘Synthesis of high quality CuO nanoflakes and CuO-Au nanohybrids for superior visible light photocatalytic behavior,’ RSC Advances, 6(85), pp. 81607-81613.

CHAPTER 6

Results and discussion

6.1. Electrochemical properties of the Cu-based nanomaterials in RGO sensing films

6.1.1. Cyclic voltammetry analysis

Cyclic voltammetry is utilized to do an extensive examination of the surface characteristics of both modified and unmodified electrodes. The CV tests were carried out using both modified and unmodified electrodes in a solution of 5 mM $K_3[Fe(CN)_6]/K_4[Fe(CN)_6]$ and 0.1 M KCl. In Figure 6.1, the quasi-reversible cyclic voltammetric signals of the six modified electrodes and the bare electrode are displayed. Higher current densities were observed at the interface of the electrodes modified with RGO containing materials in comparison to the non-RGO containing materials and bare GCE. CuO-Au-RGO/GCE has the highest oxidation peak current when compared to CuO/GCE, CuO-Au/GCE, CuO-RGO/GCE, GO/GCE, RGO/GCE and bare GCE. CuO-Au-RGO/GCE has good electrochemical performance, mostly due to its wide surface area, high porosity, and highly conductive matrix. These aspects are important to take into account. The defects and oxygenated functional groups in the RGO formed during oxidation/reduction enhancing RGO's electrochemical catalytic activity [1, 2]. Further enhancing RGO's processability and facilitating its functionalization and modification are these oxygenated functional groups [3, 4], which could enhance the electrochemical performance even more. It can also be observed that the Au loading on the RGO sheets increases the redox peak current. The higher quantity of AuNPs is considered to be responsible for the improved electrochemical surface area and conductivity. Furthermore, it is discovered that the RGO modified electrode's peak-to-peak separation (ΔEp) is less than the GO electrode's, indicating a faster rate of electron transport. Which then increases due to the loading of CuONPs on the RGO sheet in RGO-CuO due to the over-shadowing of some functional groups but improved upon the loading of AuNPs in CuO-Au-RGO. Further confirming the impact of AuNPs on the electrochemical catalytic activity on the modified electrode. Both CuO-Au and Cu-Au-RGO show multiple reversible redox processes. This is due to the second electron transfer becoming less thermodynamically

favorable causing the peak to peak separation (ΔEp) to reach a maximum value of just over 140 mV. At that moment, the wave splits into two waves that can be resolved, each with a ΔEp=57mV [5, 6]. The i_a/i_c ratio and ΔEp data for CuO/GCE, CuO-Au/GCE, CuO-RGO/GCE, GO/GCE, RGO/GCE, CuO-Au-RGO/GCE and bare GCE are illustrated in Table 1 below. The i_a/i_c ratio for all the electrodes except the bare electrodes is close to 1, indicating a great reversibility for all of them.

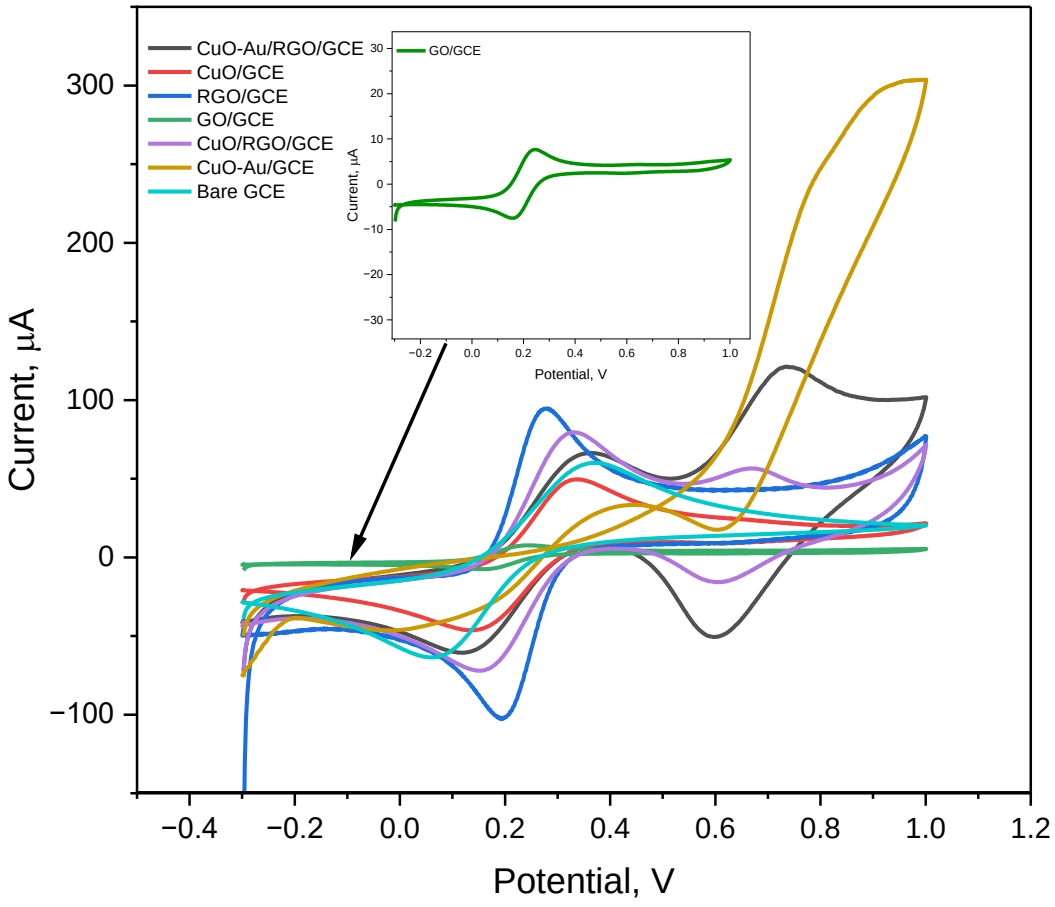

Figure 6. 1. Cyclic voltammograms of CuO-Au-RGO/GCE, CuO-RGO/GCE, CuO-Au/GCE, CuO/GCE, RGO/GCE, GO/GCE and bare GCE in 5mM $K_4[Fe(CN)_6]/K_3[Fe(CN)_6$ in 0.1 M NaCl at 50 mV/s.

Table 6. 1. The i_a/i_c ratio and ΔEp data for CuO-Au-RGO, CuO-RGO, CuO-Au, CuO and bare GCE.

Material	I_a (μA)	I_c (μA)	E_a (V)	E_c (V)	I_a/I_c	ΔE_p (V)
Bare	3.91	0.63	0.37	0.06	6.21	0.31
GO	10.15	10.01	0.24	0.16	1.01	0.08
RGO	103.30	107.26	0.27	0.20	0.96	0.07
CuO	14.51	55.84	0.34	0.14	0.26	0.20
CuO/Au	-	-	-	-	-	-
CuO/RGO	81.87	77.14	0.33	0.15	1.06	0.18
CuO-Au-RGO	61.67	67.3	0.36	0.12	0.92	0.24

In a 5 mM $K_3[Fe(CN)_6]/K_4[Fe(CN)_6]$ redox probe containing 0.1 M of NaCl, cyclic voltammetry measurements of GO, RGO, CuS, CuS-Au, CuS-RGO, CuS-Au-RGO-modified GCE, and bare GCE were also performed at a fixed scan rate of 50 mVs^{-1} within a potential window of -0.3 and 1 V as shown in Figure 6.2. Due to the presence of CuSNPs and RGO on the surface of the GCE, the modified GCE with CuS-RGO displayed a larger peak to peak separation (ΔE_p) and peak current ratio (i_a/i_c) compared to GO/GCE, RGO/GCE, CuS/GCE, CuS-Au/GCE and CuS-Au-RGO/GCE. Further confirming the effect of RGO in promoting electron transfer process at the GCE surface, and also a result of the sulfur atoms added by the capping ligand and the CuS nanoparticles. Negatively charged sulfur atoms have also been shown to improve electrochemical properties [7].

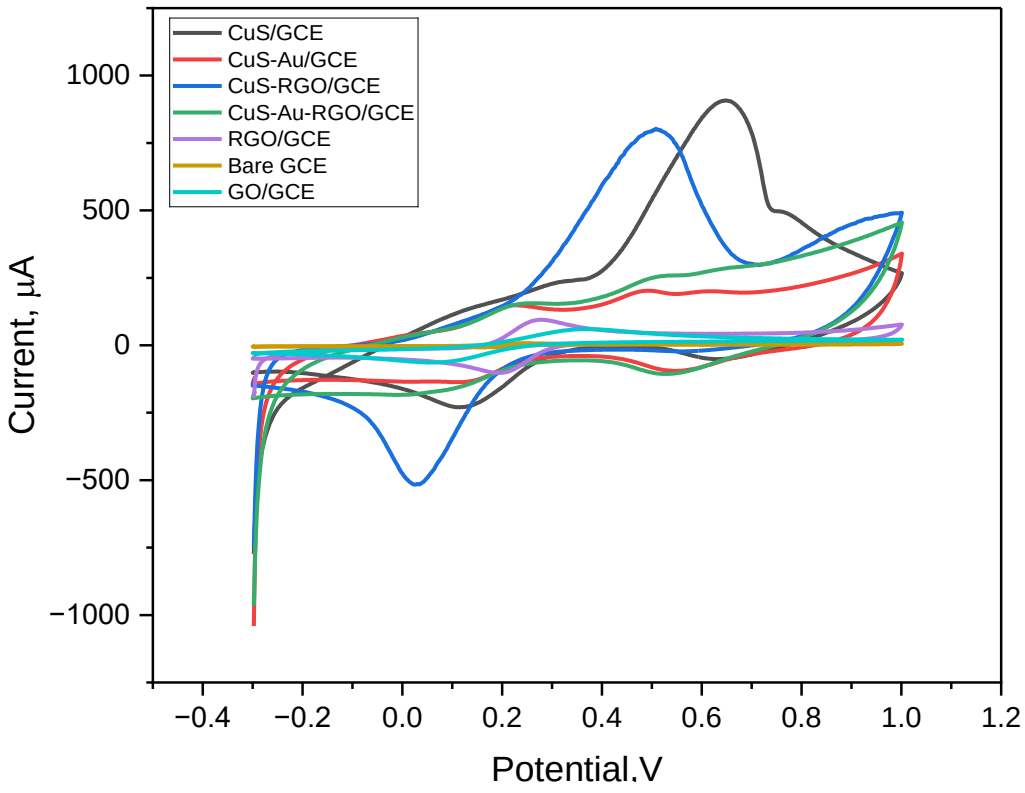

Figure 6. 2. Cyclic voltammograms of CuS-Au-RGO, CuS-RGO, CuS-Au, CuS and bare GCE in 5mM $K_4[Fe(CN)_6]/K_3[Fe(CN)_6$ in 0.1 M NaCl at 50 mV/s.

Table 6. 2. The i_a/i_c ratio and ΔEp data of Cus-Au-RGO, Cus-RGO, Cus-Au, Cus and bare GCE.

Material	I_a (µA)	I_c (µA)	E_a (V)	E_c (V)	I_a/I_c	ΔE_p (V)
Bare	3.91	0.63	0.37	0.06	6.21	0.31
GO	10.15	10.01	0.24	0.16	1.01	0.08
RGO	103.30	107.26	0.28	0.20	0.96	0.07
CuS	480.00	223.14	0.65	0.12	2.15	0.53
CuS/Au	142	143	0.21	0.13	0.99	0.08
CuS/RGO	709.1	535.8	0.51	0.03	1.32	0.48
CuS-Au-RGO	250	180.48	0.51	0.02	1.38	0.48

6.1.2. Electrochemical impedance spectroscopy (EIS)

Electrochemical impedance spectroscopy (EIS) investigations were carried out to investigate the electrochemical kinetics of the CuO-Au-RGO, CuO-RGO, CuO-Au, CuO and bare GCE at the electrode/electrolyte interface. EIS was recorded using the 5 mM

$[Fe(CN)_6]^{3-}/[Fe(CN)_6]^{4-}$ redox probe. Figure 5 shows the Randles equivalent circuit of CuO-Au-RGO/GCE, CuO-RGO/GCE, CuO-Au/GCE, CuO/GCE and bare GCE, together with the Nyquist plots for each. Table 3 also shows the fitted comparable circuit module parameters. The diameter of the semicircle in the Nyquist plot is known to provide information on the interface's charge transfer resistance (Rct), and the EEC is used to find its value [8]. A lower arc radius is associated with a higher efficiency of charge immigration across the electrode-electrolyte interface, and the behavior of electron-transfer resistance on the electrode surface can be reflected in the arc radius at higher frequencies, and the diffusion process is represented by the liner portion at lower frequencies [9, 10, 11]. All of the materials' semicircles, as shown in Figure 6.3(a), are smaller than GO/GCE and bare GCE, suggesting a low electron transfer resistance on its surface. Which may account for their improved electrochemical characteristics. Figure 6.2 also illustrates that the Rct for RGO/GCE (53.6 Ω) is less than that of GO/GCE (25204.0 Ω), which is displayed in Table 3. Indicating the excellent conductivity of the RGO. The arc radius grew upon Addition of CuO within the RGO sheets, suggesting that pure CuO inhibited electron transfer, resulting in the increase of the Rct from 53.6 Ω to 682.3 Ω of CuO/RGO/GCE. This can be attributed to the CuONPs' semiconductivity. The CuO/RGO composite possessed a low electron transfer resistance (682.3 Ω) on its electrode surface compared to GO/GCE, CuO/GCE, CuO-Au/GCE, CuO-Au-RGO/GCE and bare GCE, this can be attributed to the high conductivity of RGO. CuO/Au possessed the highest Rct value of 14452.0 Ω. Suggesting electron transfer inhibition at the electrode and surface area blockage [12]. Thus, indicating low conductivity and low electron transfer. Upon the introduction of RGO in CuO-Au to form Cu-Au-RGO, the Rct decreased from 14452.0 Ω to 1713.9 Ω. Which means the conductivity improved upon the addition of RGO. Additionally, The Rs value for CuO-Au-RGO/GCE is lower than that of CuO-Au/GCE and CuO-RGO/GCE, demonstrating an enhanced $[Fe(CN)6]^{3-}/[Fe(CN)6]^{4-}$ redox process electrocatalytic activity on its electrode surface [13,14]. Equation (6.1) below was used to calculate the surface coverage (θ) as showed in Table 3 [15].

$$\theta = 1 - \frac{R_{ct\,(Bare)}}{R_{ct\,(modified)}} \tag{6.1}$$

Where R_{ct} (Bare) is charge transfer resistance for Bare GCE and R_{ct} (modified) is charge transfer resistance for CuO-Au-RGO/GCE, CuO-RGO/GCE, CuO-Au/GCE, CuO/GCE, RGO/GCE and GO. RGO/GCE had the largest surface coverage (θ) with a value of 30.53 compared to CuO-Au-RGO/GCE, CuO-RGO/GCE, CuO-Au/GCE, CuO/GCE, GO/GCE and bare GCE, indicating a high surface concentration of the electroactive species and better electrocatalytic performance [16,17]. CuO-RGO/GCE had a larger suface coverage compared to CuO/GCE, indicating a large surface concentration which can also be attribute to RGO.

The Bode plots (figure 6.3b) shows a decrease in the phase angle from 59º for bare Electrode to 18º for CuO-RGO/GCE, indicating that CuO-RGO/GCE has a good conductive behavior compared to others. CuO/GCE has a phase angle of 52º which reduced to 32º for CuO-Au-RGO/GCE due to the addition of RGO to CuO/Au nanohybrids materials. According to a report by Molina et al. (2013), a phase angle close to 0º showed that the samples behaved as conducting materials, while a value close to 90º showed that the samples acted as insulating materials [18]. The results are consistent with the results obtained from the CV and the Nyquist plot.

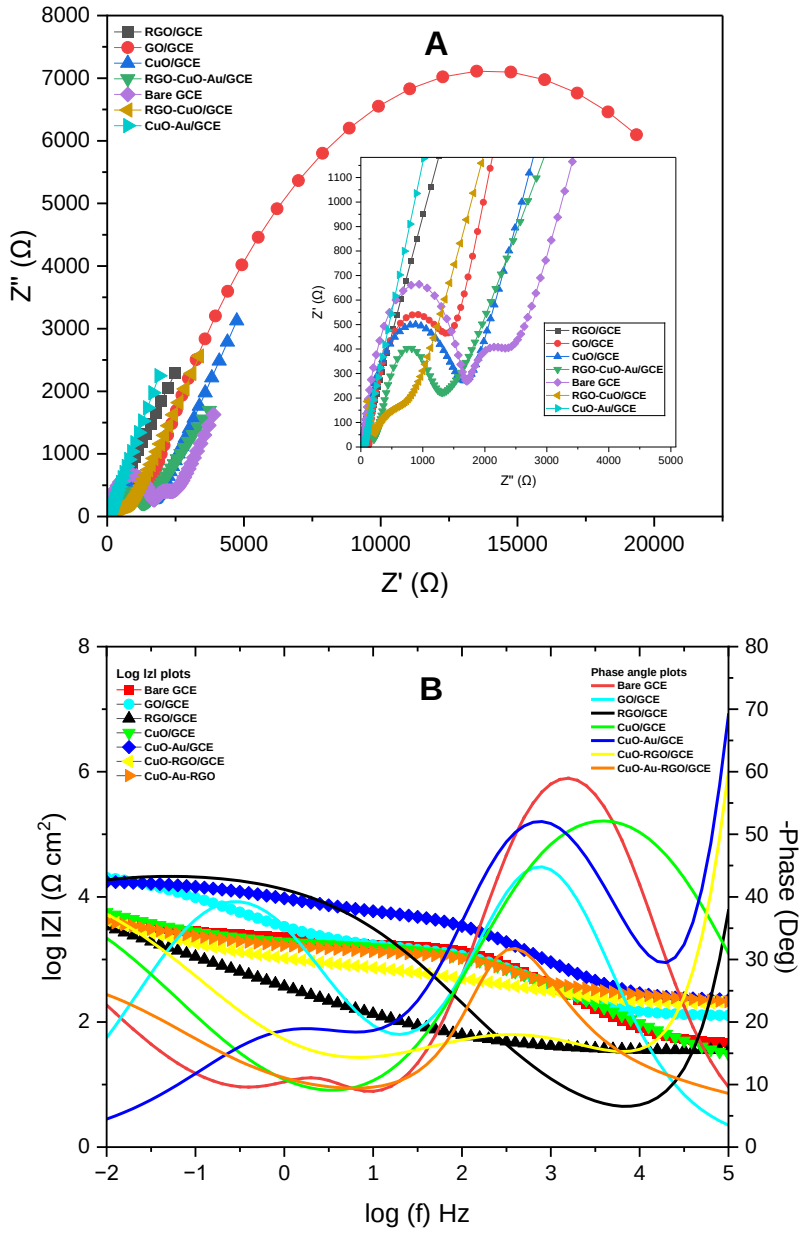

Figure 6. 3. Nyquist (A) and Bode (B) plots of CuO-Au-RGO/GCE, CuO-RGO/GCE, CuO-Au/GCE, CuO/GCE and bare GCE in 5mM $K_4[Fe(CN)_6]/K_3[Fe(CN)_6$ in 0.1 M NaCl.

Table 6. 3. EIS data of the CuO-Au-RGO/GCE, CuO-RGO/GCE, CuO-Au/GCE, CuO/GCE and bare GCE in $[Fe(CN)_6]^{3-}/[Fe(CN)_6]^{4-}$.

Materials	R_s (Ω)	CPE (μF)	R_{ct} (Ω)	θ
Bare	43.9	1.64	1690.3	-
GO	123.9	120.72	25204.0	0.93
RGO	13.5	0.0033	53.6	30.53
CuO	17.7	5.53	1618.3	0.04
CuO/Au	152.0	4.76	14452.0	0.88
CuO/RGO	224.7	107.71	682.3	1.48
CuO-Au-RGO	137.3	1.53	1713.9	0.01

*R_s is electrolyte resistance; CPE is constant phase element; R_{ct} is the charge transfer resistance; θ is the surface coverage;

Figure 6.4 below depicts the Bode (a) and Nyquist plots for CuS-Au-RGO/GCE, CuS-RGO/GCE, CuS-Au/GCE, CuS/GCE, GO/GCE, RGO/GCE and bare GCE. The Rct values (Table 4) were obtained by fitting the EIS data to the Randle's equivalent circuit. Compared to CuS-Au-RGO/GCE, CuS-RGO/GCE, CuS-Au/GCE, CuS/GCE, GO/GCE and bare GCE, RGO/GCE shows the lowest Rct value (53.6Ω), which indicates larger electron transfer. GO/GCE shows the lowest Rct value, which can be attributed to its insulating characteristic. The disturbed sp^2 structure was associated with the insulating property of graphene oxide [19]. Furthermore, it could be observed from figure 6.4(a) that CuS-RGO/GCE and CuS-Au-RGO/GCE have a smaller semicircle than both CuS/GCE and CuS-Au/GCE. This can also be confirmed by their Rct values which are 233.57 Ω for CuS-RGO/GCE and 67.19 Ω for CuS-Au-RGO/GCE. The high Rct in CuS/GCE and CuS-Au/GCE can be attributed to the semiconducting characteristic of CuS nanoparticles. The CuS-Au-RGO, CuS-RGO, CuS-Au, CuS, RGO, GO and modified GCE interfaces' electrochemical surface characteristics were assessed in relation to the Bare GCE's charge transfer resistance. The surface coverage (θ) of CuS-Au-RGO/GCE, CuS-RGO/GCE, CuS-Au/GCE, CuS/GCE, RGO/GCE, GO/GCE and bare GCE were obtained using Equation (6.1). Compared to CuS-RGO/GCE (6.24), CuS-Au/GCE (2.88) and CuS/GCE (3.76), CuS-Au-RGO (24.12) has a larger electrochemical surface coverage as anticipated due to its large surface area. Figure 6.4(b) presents the Bode plots of the

CuS-Au-RGO/GCE, CuS-RGO/GCE, CuS-Au/GCE, CuS/GCE, GO/GCE, RGO/GCE and bare GCE.

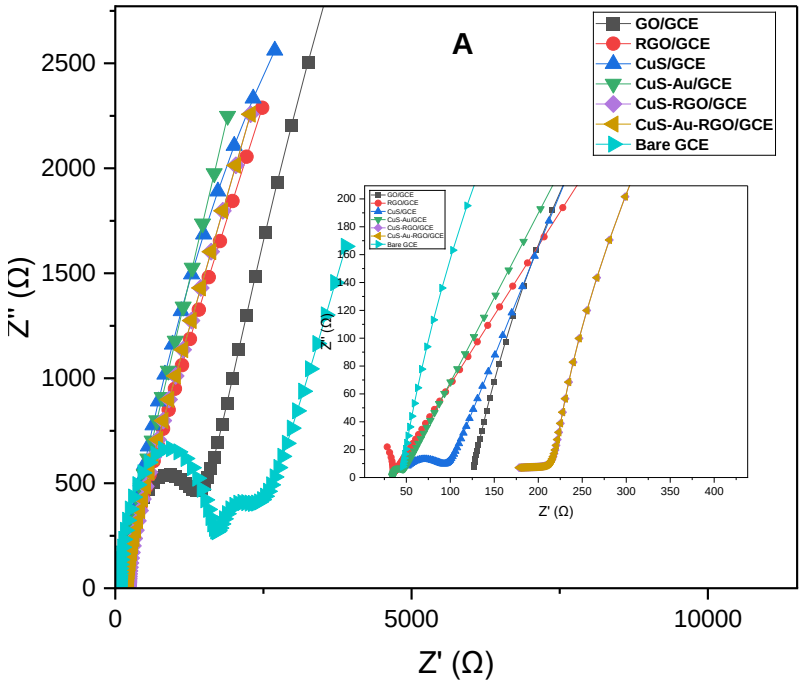

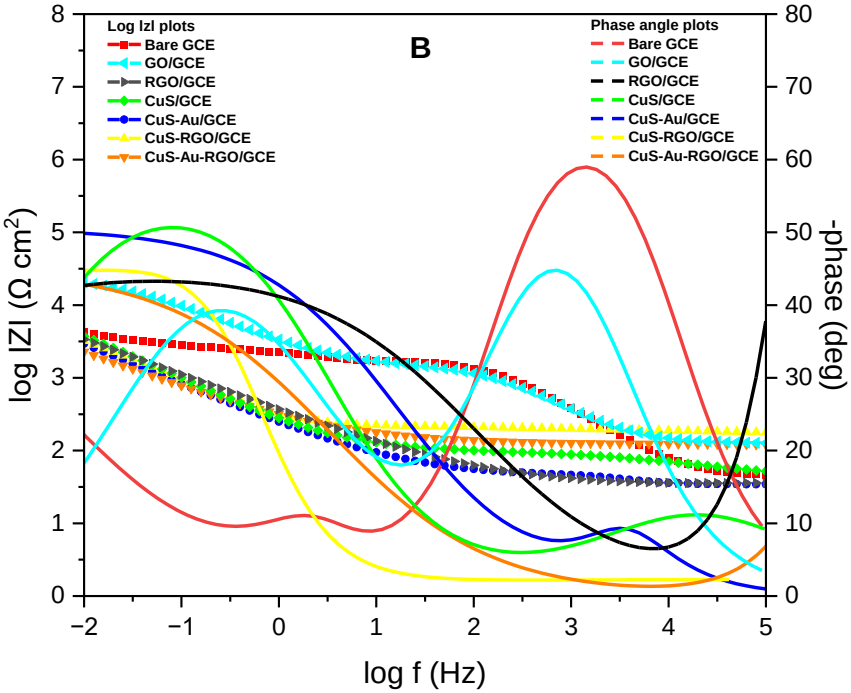

Figure 6. 4. Nyquist (A) and Bode (B) plots of CuS-Au-RGO/GCE, CuS-RGO/GCE, CuS-Au/GCE, CuS/GCE, GO/GCE, RGO/GCE and bare GCE in 5mM $K_4[Fe(CN)_6]/K_3[Fe(CN)_6$ in 0.1 M NaCl.

The Bode plots show a decrease in the absolute phase angle from 59º for the bare GCE to 42º for CuS-Au-RGO/GCE. This indicates an increase in conductivity at the CuS-Au-RGO/GCE interface. The phase angle changed from 51º for CuS/GCE to 45 º for CuS-RGO/GCE. This is because of the reduced graphene oxide layer that increased the electroactivity and conductivity of of CuS-RGO/GCE. These results are consistent with the results obtained from the CVs and Nyquist plot.

Table 6. 4. EIS data of the CuS-Au/RGO/GCE, CuS-RGO/GCE, CuS-Au/GCE, CuS/GCE and bare GCE in $[Fe(CN)_6]^{3-}/[Fe(CN)_6]^{4-}$.

Material	R_s (Ω)	CPE (µF)	R_{ct} (Ω)	θ
Bare	43.9	1.64	1690.3	-
GO	123.9	120.72	25204.0	0.93
RGO	13.5	0.0033	53.6	30.53
CuS	-205.56	474.74	354.85	3.76
CuS/Au	490.72	0.14	435.62	2.88
CuS/RGO	91.686	1.53	233.57	6.24
CuS-Au-RGO	150.2	0.01	67.19	24.16

*R_s is electrolyte resistance; CPE is constant phase element; R_{ct} is the charge transfer resistance; θ is the surface coverage

6.2. Scan rates studies of CuS-Au/RGO-Modified Electrodes

This study's goal was to track the ideal scan rate required to ensure the highest response and fair stability of CuS-Au/RGO sensor film onto glassy carbon electrode. Adsorption or diffusion can drive material oxidation and reduction reactions; both depend on scan rates [20]. As stated in the preceding sections, CuS-Au/RGO nanocomposites exhibited a remarkable electrochemical behavior when compared to other nanocomposites and nanomaterials hence they were employed for the electrochemical detection of Cr^{3+} and Hg^{2+}. The Cyclic voltammograms of the CuS-Au/RGO/GCE sensing film are displayed in Figure 6.5. The redox behavior of the Au/RGO/GCE modified electrode at different scan rates was investigated. The scan rate was varied from 0.03 to 0.15 V s^{-1} at a potential

window between -0.5 and 1.0 V. Cathodic and anodic peak currents increased when scan rates increased from 0.005 to 0.06 V/s, shown in Figure 6.6 A. Shifts in the reduction and oxidation potentials were also noted.

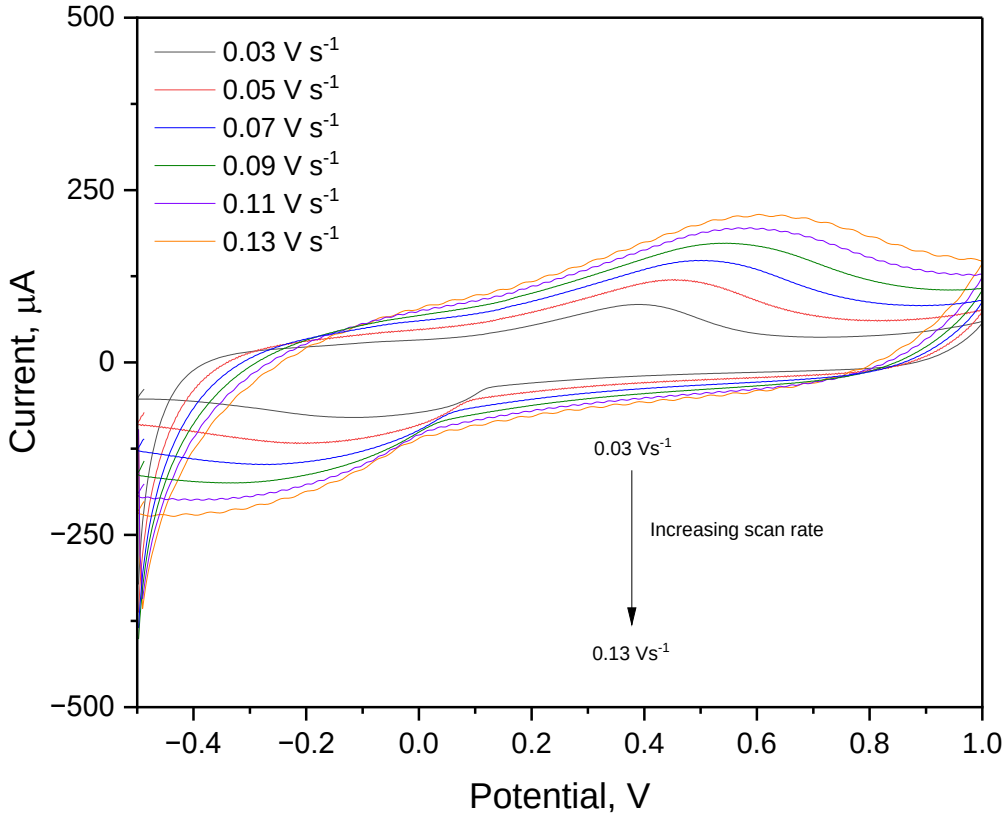

Figure 6. 5. Cyclic voltammograms of the CuS-Au/RGO/GCE at different scan rates (0.03 to 0.15 V S^{-1}).

At high scan rates, the anodic currents switched to substantially more positive potential values, whereas the cathodic currents shifted toward bigger negative potentials. Increased potential differences are frequently the outcome of these shifts in the cathodic and anodic potentials. This behavior is explained by the heterogeneous electron transfer kinetics at the electrode surface, which point to a quasi-reversible redox system.

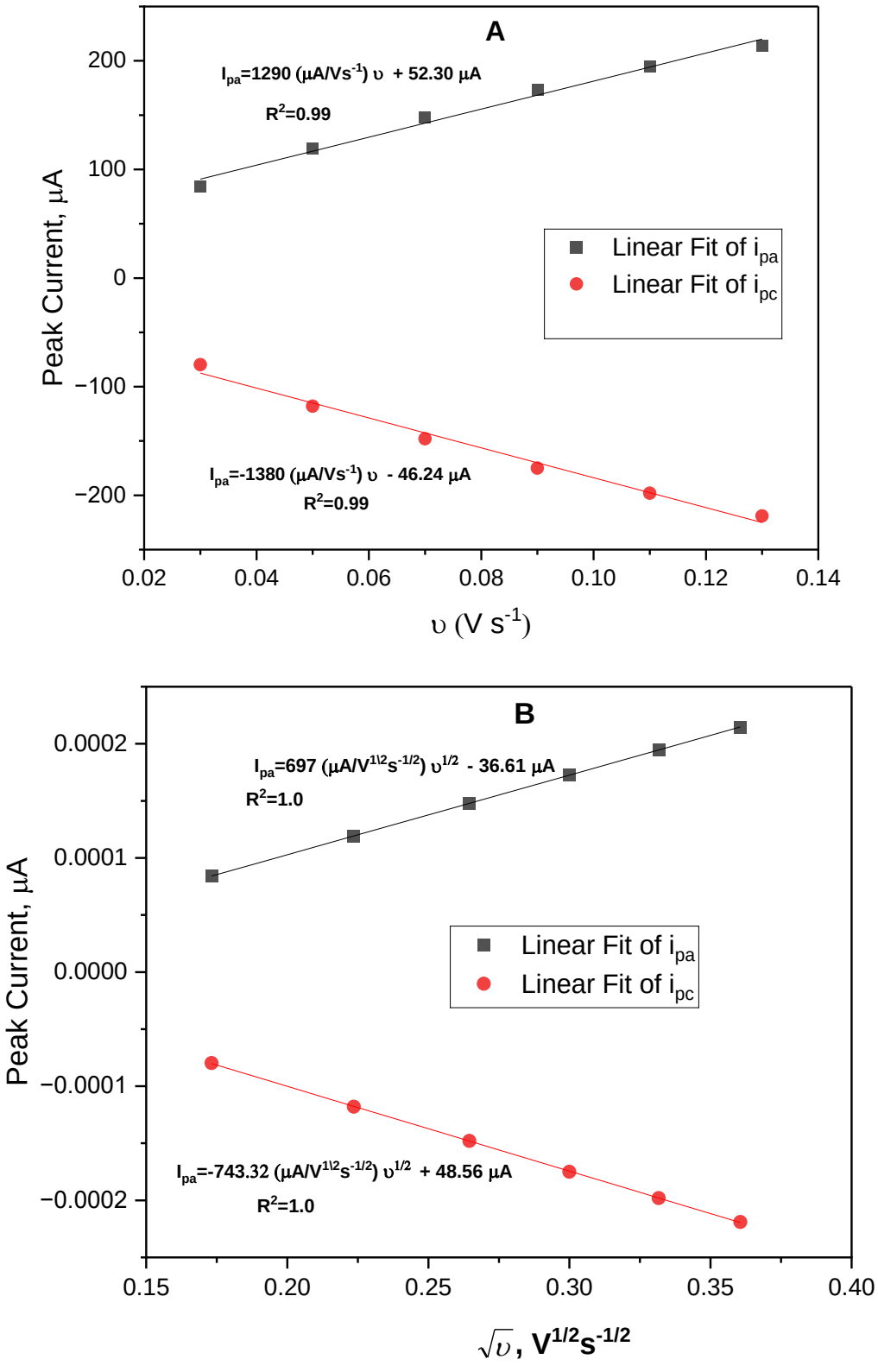

Figure 6. 6. Linear plots of peak currents (i_p) versus (A) Scan rate and (B) square root of scan rate.

Excellent linear relationships that matched the linear equations were found when both redox peak currents Vs scan rate (Figure 6.6a) and redox peak currents Vs square root of scan rate (Figure 6.6b) were compared. Equation 6.2 was used to calculate the electro-active layer surface concentration (Γ) magnitudes.

$$i_p = \frac{n^2 F^2 A}{4RT} \Gamma v \tag{6.2}$$

The peak current for either the cathodic or anodic process is represented by the i_{pc} parameter in Eq. 2. n is the number of electrons moved throughout the redox process; F is the faraday's constant expressed in C/mol. The parameters A denotes the working electrode surface's geometric area in centimeters, Γ denotes surface concentration, v denotes scan rate, R denotes ideal gas constant, and T denotes temperature in kelvin.

Figure 6.6a depicts the scan rate-dependent electrochemical behaviors of the CuS-Au/RGO film modified GCE. An $R^2 > 0.85$ for the linear plots indicates that an electrochemical reaction is an adsorption-controlled process [21]. For the oxidation process at the CuS-Au/RGO modified electrode surface, the R^2 of the plot of i_{pa} vs. $v^{0.5}$ was 0.99. Shifts in the oxidative anodic potential were also noted when scan rates increased, suggesting quicker redox kinetics at moderately increased scan rates [22]. The oxidation processes were estimated to have a surface concentration of 1.93 x 10^{-8} mol/cm^2. But 2.07 x 10^{-8} mol/cm^{-2} surface concentration was determined for the cathodic process. The indication of a very thin coating adsorbed on the electrode surface is given by the low magnitude of the surface concentration. In the second layer of the electrode, thinner films modify the electrode interface and speed up electron transport reactions.

The oxidation reaction peak obeys the Randles-Sevcik relationship. The computed diffusion co-efficient (D), which was determined using Equation 6.3 below, was roughly 1.3 x 10^{-8} cm^2 s^{-1} and 1.5 x 10^{-8} cm^2 s^{-1} for the anodic and cathodic processes respectively. This result demonstrates that the reaction was diffusion-controlled [23]. According to Liu et al. (2014), a lower diffusion coefficient indicates a quicker electron transport between the electrolyte and the electrode contact [24].

$$i_p = (2.69 \times 10^5) n^{\frac{3}{2}} A C D^{\frac{1}{2}} v^{\frac{1}{2}} \quad (6.3)$$

6.3. The effect of pH on the electrochemical properties of CuS-Au/RGO/GCE sensor platform

Evaluation of the pH's impact on anodic peak currents was done in order to optimize the techniques for Hg (ll) and Cr(III) detection using the CuS-Au/RGO/GCE. Cyclic voltammograms and the impact of pH on the anodic peak currents are displayed in Figure 6.7a, b. higher electro-activity, which was attained at pH 6.17, is responsible for the highest peak current response.

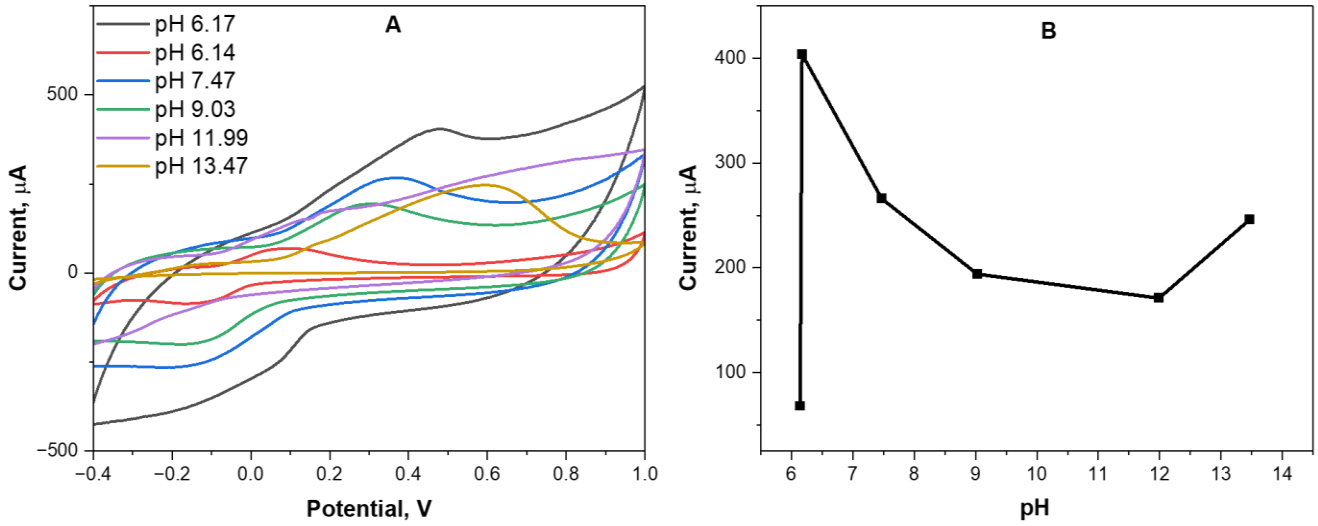

Figure 6. 7. (A) Cyclic voltammogram of CuS-Au/RGO sensing platform at different pH (6.17, 6.14, 7.47, 9.03, 11, 99, and 13.47). (B) The plot of peak current against pH.

Additionally, as pH increased from pH of 6.17 to 11.99, the anodic peak currents values decreased (Figure 6.7). This finding suggests that the oxidation process on the CuS-Au/RGO/GCE surface involved protons between these pH values [25, 26]. At the pH 11.99, the current responses started increasing from 171 to 246 µA, corresponding to the pH of 11.99 and 13.47 respectively. The acidic conditions have also been reported to be suitable for the detection of mercury (II) and chromium (III) [27, 28].

6.4. Stability of the CuS-Au/RGO nanocomposites on the electrode surface

The stability of CuS-Au/RGO nanocomposites sensing film modified onto the glassy carbon electrodes (GCEs) was investigated using the cyclic voltammetry. The stability of the nanocomposites on the GCE surfaces was assessed within the potential window between 0.6 V to 1V-. At a pH of 6.17, ten voltammetry scans were used in order to examine the electrochemical characteristics of CuS-Au/RGO nanocomposites film adhered onto the electrode surface 0.1 M phosphate buffer solution with pH of 6.17 was used as the electrolyte. Stability, sensitivity, and repeatability are among the crucial sensor properties [29]. In Figure 6.8, the electrochemical redox reaction of CuS-Au/RGO nanocomposites was investigated using the CV approach to ascertain the stability of the sensor.

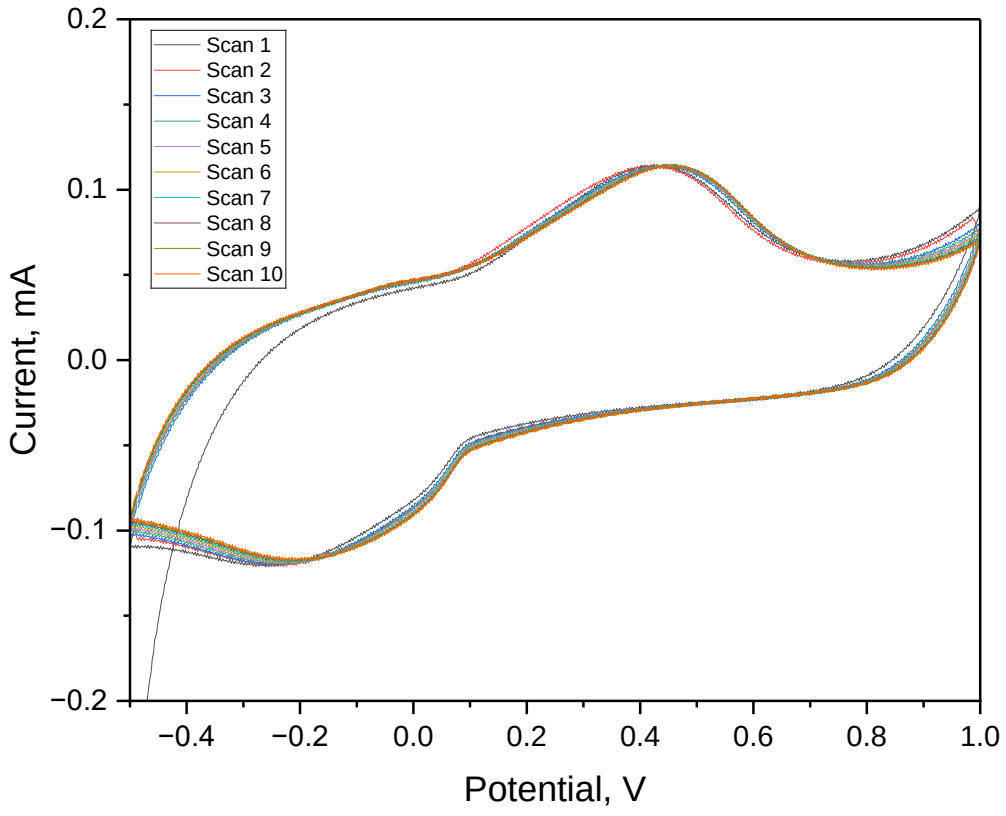

Figure 6. 8. The cyclic voltammogram signals of CuS-Au/RGO modified GCEs after 10 consecutive scans.

The CuS-Au/RGO nanocomposites remained remarkably stable on the electrode surface even after ten cycles, as evidenced by their unaltered peak currents and potentials in relation to the increased number of scans. Since the stability of material onto the electrode is thought to be one of the main limitations in electrochemical sensing, CuS-Au-RGO will be preferred for the detection of Cr(III) and Hg (II) heavy metal ions. This result suggests that CuS-Au/RGO nanocomposites were less affected by the environmental and redox conditions [30].

6.5. SWV-ASV for the detection of H (II) ang Cr(III) using CuS-Au/RGO/GCE sensing films

Due to its increased sensitivity for monitoring the low-level detection of organic contaminants, prescription medications, toxic metal ions, etc., the square-wave anodic stripping methodology is seen to be somewhat superior to the traditional CV methods. Consequently, the square-wave anodic stripping voltammetry (SWV-ASV) technique was utilized to electrochemically detect Hg (II) and Cr(III) utilizing CuS-Au/RGO/GCE. The optimized detection conditions were established as follows; an operating potential range of 1.0 to -1.0 V in optimized 0.1 M PBS (pH = 6.9) electrolyte solution and a deposition time of 300 s. Various concentrations of Hg (II) (0 to 10 ppb) and Cr(III) (0 - 100 ppb) concentrations were employed as described. Figure 6.9a illustrates a sharp anodic peak that results from an increased oxidation peak current when Hg (II) concentration varies from lower to higher. The CuS-Au/RGO/GCE sensor's square-wave responses and corresponding linear calibration plots at various Hg (II) concentrations are shown by the highest peak current response.

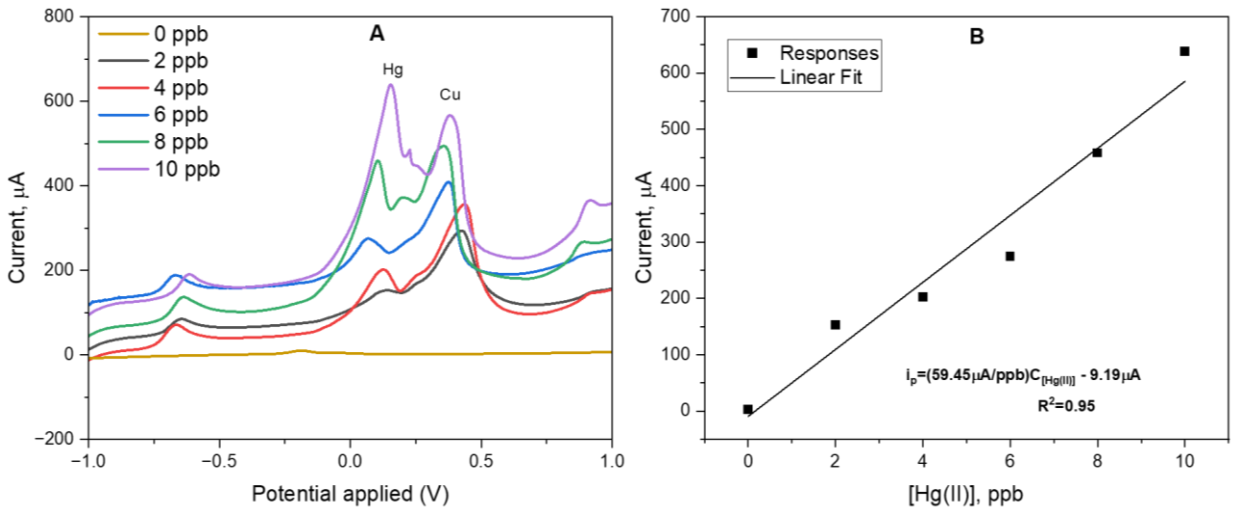

Figure 6. 9. (A) The square-wave anodic stripping voltammetry curves of CuS-Au/RGO modified GCE at different concentration of Hg^{2+} from 2-10 ppb in phosphate buffer solution, at the optimal conditions (i.e. pH =6.9) in 1M NaCl. (B) The corresponding linear calibration plot of the sensor.

According to figure 6.9a, the stripping of Hg (II) caused the oxidation peak to arise at 0.15 V for the first concentration of Hg (II), which is equivalent to 2 ppb. The peak is attributed to Hg (0) oxidizing to Hg (II). The highest current response (639 µA) was due to Hg (II) concentration of 10 ppb. Another sharp oxidation peak appears around 0.48 V which is attributed to Cu (II) ions from the supporting material. The peak can be differentiated by how the current intensity of its response peaks remains the same with increasing concentration of Hg(II), whilst the amplification of the current intensity at 0.15 V {characteristic Hg(II) peak responses} is amplified in relation to the increase in the concentration of Hg(II). As seen in Figure 6.9b, CuS-Au/RGO/GCE revealed an excellent linear response in the examined range of 0-10 ppb Hg (II) with correlation coefficient R^2 = 0.95 and the linear regression equation was i_p= (59.45µA/ppb) $C_{[Hg\ (II)]}$ - 9.19 µA. The limit of detection was determined using $3.3(\frac{\sigma}{S})$, where σ the standard deviation of the peak currents and S is the slope of the calibration plot. The calculated limit of detection of the sensing platform was 2 ppb. Hg (II) has a 2 ppb regulatory limit set by the World Health Organization. The designed sensor was capable of detecting Hg (II) standard

concentrations both above and below the WHO limit. Subsequently, the developed sensor showed a linear response from (2- 10) ppb of Hg (II), this is the dynamic linear range of the developed CuS-Au/RGO/GCE sensor. A sensitivity of 59.45µA/ppb was obtained indicating the good electrochemical response of the sensor towards different concentrations of the Hg (II).

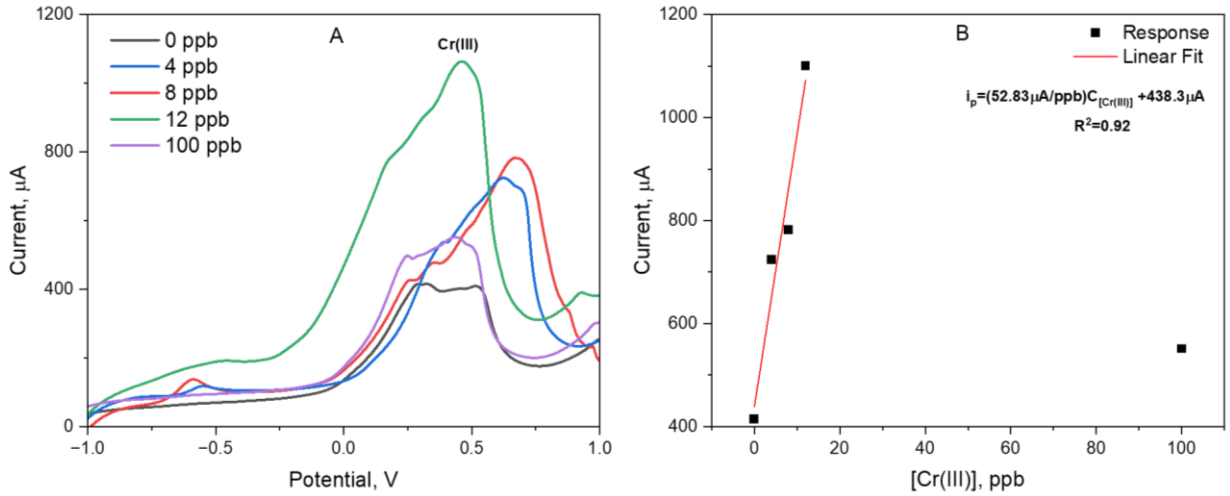

Figure 6. 10. (A) The square-wave anodic stripping voltammetry (SWV-ASV) curves of CuS-Au/RGO modified GCE at different concentration of Cr^{3+} from 2-10 ppb in phosphate buffer solution, at the optimal conditions (i.e. pH =6.9) in 1M NaCl. (B) The corresponding linear calibration plot of the sensor.

The SWV-ASV method was also used to verify the electrochemical responses of the CuS-Au/RGO-modified electrodes at different Cr(III) concentrations (0-100 ppb) (Figure 6.10a, b). The SWV-ASV electrochemical measurements were performed at a potential range between -1 to 1 V, in optimized 0.1 M PBS (pH = 6.9) electrolyte solution at the optimized deposition time of 300 s. The oxidation peaks current at 0.62 V corresponding to the oxidation of Cr (0) to Cr(III) increased in proportion to the increase concentration of Cr(III). The SWV-ASV curves produced at various Cr(III) concentrations are displayed in Figure 6. 10a.The linear response was only obtained at the concentration from (0-8) ppb of Cr(III) then after, the height of peak current and the concentration of Cr(III) were non-linearly correlated at concentration above 8 ppb.

As seen by the calibration plot in Figure 6.10b, a significant decrease of electrochemical activity was noted for concentrations of Cr(III) around 100 ppb. This can be explained by the occurrence of an insulator layer at high Cr(III) concentrations on the electrode surface, which causes the activity to decrease. CuS-Au/RGO/GCE demonstrated an outstanding linear response (at 0.62 V) in the studied range as shown in Figure 6.10b {0-8 ppb of Cr(III)} with a correlation coefficient of $R^2 = 0.92$. The computed limit of detection (LOD), based on the 3σ criterion, was ~2 ppb Cr(III), along with 52.83 µA/ppb sensitivity and the dynamic linear range of (0-8 ppb) of Cr(III) The calculated limit of detection is 50 times less than the permissible limit of Cr(III) in drinking water which is set at 100 ppb [31].

REFERENCES

1. Liu, D. and Long, Y.T. (2015) 'Superior catalytic activity of electrochemically reduced graphene oxide supported iron phthalocyanines toward oxygen reduction reaction,' ACS applied materials & interfaces, 7(43), pp. 24063-24068.
2. Chen, C.M. et al. (2012) 'Structural evolution during annealing of thermally reduced graphene nanosheets for application in supercapacitors,' Carbon, 50(10), pp. 3572-3584
3. Kang, S.M. et al. (2010) 'Simultaneous reduction and surface functionalization of graphene oxide by Mussel-Inspired chemistry,' Advanced Functional Materials, 21(1), pp. 108-112.
4. Kulakova, I.I. and Lisichkin, G.V. (2020) 'Chemical modification of graphene,' Russian Journal of General Chemistry, 90, pp.1921-1943.
5. Bard, A.J. et al. (2022) 'Electrochemical methods: fundamentals and applications,' John Wiley & Sons.
6. Elgrishi, N. et al. (2017) 'A practical Beginner's guide to cyclic voltammetry,' Journal of Chemical Education, 95(2), pp. 197-206.
7. Madhuvilakku, R. et al. (2018) 'Sensitive and selective non-enzymatic detection of glucose by monodispersed NiO @ S-doped hollow carbon sphere hybrid nanostructures,' Analytica Chimica Acta, 1042, pp. 93-108.

8. Giordano, L. et al. (2016) ‘pH dependence of OER activity of oxides: Current and future perspectives,’ Catalysis Today, 262, pp. 2-10.
9. Mao, Z. et al. (2017) ‘Novel g-C3N4/CoO nanocomposites with significantly enhanced visible-light photocatalytic activity for H2 evolution,’ ACS applied materials & interfaces, 9(14), pp.12427-12435.
10. Kan, X. et al. (2012) ‘Imprinted electrochemical sensor for dopamine recognition and determination based on a carbon nanotube/polypyrrole film,’ Electrochimica Acta, 63, pp. 69-75.
11. Hwang, I. and Yong, K. (2015) ‘Counter electrodes for Quantum-Dot-Sensitized solar cells,’ ChemElectroChem, 2(5), pp. 634-653.
12. Functionalized Electrochemical Aptasensor for Sensing of Ochratoxin A in Cereals Supported by in Silico Adsorption Studies
13. Savariraj, A.D. et al. (2014) ‘CuS nano flakes and nano platelets as counter electrode for quantum dots sensitized solar cells,’ Electrochimica Acta, 149, pp. 364-369.
14. Raj, C.J. et al. (2013) ‘Surface reinforced platinum counter electrode for quantum dots sensitized solar cells,’ Electrochimica Acta, 103, pp. 231-236.
15. Ndangili, P.M. et al. (2011) ‘Impedimetric response of a Label-Free genosensor prepared on a 3-Mercaptopropionic acid capped gallium selenide nanocrystal modified gold electrode,’ International Journal of Electrochemical Science, 6(5), pp. 1438-1453.
16. Madhuvilakku, R. et al. (2018b) ‘Sensitive and selective non-enzymatic detection of glucose by monodispersed NiO @ S-doped hollow carbon sphere hybrid nanostructures,’ Analytica Chimica Acta, 1042, pp. 93-108.
17. Raza, W. and Ahmad, K. (2018) ‘A highly selective Fe@ZnO modified disposable screen printed electrode based non-enzymatic glucose sensor (SPE/Fe@ZnO),’ Materials Letters, 212, pp. 231-234.
18. Molina, J. et al. (2013) ‘Chemical and electrochemical study of fabrics coated with reduced graphene oxide,’ Applied Surface Science, 279, pp. 46-54.

19. Molina, J., Fernández, J.C., Inés, J.C., et al. (2013) 'Electrochemical characterization of reduced graphene oxide-coated polyester fabrics,' Electrochimica Acta, 93, pp. 44-52.
20. Tratnyek, P.G. et al. (2001) 'Visualizing redox chemistry: probing environmental oxidation- reduction reactions with indicator dyes,' The Chemical Educator, 6(3), pp.172-179.
21. Laviron, E. (1979) 'General expression of the linear potential sweep voltammogram in the case of diffusionless electrochemical systems,' Journal of Electroanalytical Chemistry and Interfacial Electrochemistry, 101(1), pp. 19-28
22. Gu, T. et al. (2013) 'Dual-signal anodic stripping voltammetric determination of trace arsenic(III) at a glassy carbon electrode modified with internal-electrolysis deposited gold nanoparticles,' Electrochemistry Communications, 33, pp. 43-46.
23. Bu, J. et al. (2019) 'Co-spray printing of LiFePO 4 and PEO-Li 1.5 Al 0.5 Ge 1.5 (PO 4) 3 hybrid electrodes for all-solid-state Li-ion battery applications,' Journal of Materials Chemistry A, 7(32), pp.19094-19103.
24. Liu, F. et al. (2014) 'Time of flight electrochemistry: diffusion coefficient measurements using interdigitated array (IDA) electrodes,' Journal of The Electrochemical Society, 161(13), pp. 3015-3019.
25. Breslin, C.B. et al. (2018) 'Electrochemical detection of Cr(VI) with carbon nanotubes decorated with gold nanoparticles,' Journal of Applied Electrochemistry, 49(2), pp. 195-205.
26. Wang, X. et al. (2018) 'Paper-Based sensor chip for heavy metal ion detection by SWSV,' Micromachines, 9(4), p. 150.
27. Balasurya, S. et al. (2020) 'Colorimetric detection of mercury ions from environmental water sample by using 3-(Trimethoxysilyl)propyl methacrylate functionalized Ag NPs-tryptophan nanoconjugate,' Journal of Photochemistry and Photobiology. B, Biology, 207, p. 111888.
28. Prabhakaran, D.C. et al. (2020) 'Electrochemical detection of Cr(VI) and Cr(III) ions present in aqueous solutions using bio-modified carbon paste electrode: a voltammetric study,' International Journal of Environmental Analytical Chemistry, 102(9), pp. 2053-2073.

29. Rajasekhar, C. et al. (2020) ‘A novel electrochemical biosensor for the detection of ethambutol,’ Indian Journal of Chemistry -Section a (IJCA), 57(7), pp. 887-895.
30. Ayranci, R. et al. (2017) ‘Rhodamine-based conjugated polymers: potentiometric, colorimetric and voltammetric sensing of mercury ions in aqueous medium,’ Analyst (London. 1877. Online)/Analyst, 142(18), pp. 3407-3415.
31. Sayato, Y. (1989) ‘WHO guidelines for drinking-water quality.,’ Eisei Kagaku, 35(5), pp. 307-312.

CONCLUSIONS AND RECOMMENDATIONS

Conclusion

Cu-based nanomaterials on RGO were successfully synthesized via both in situ and ex situ approaches. The morphological and structural composition of the prepared nanocomposites were determined by TEM, UV-vis, FTIR and XRD. The XRD revealed that the prepared CuO nanoparticles have a monoclinic phase. The UV-vis confirmed that the CuS nanoparticles have a covellite phase, this is due to the absorption band in the NIR region. A glassy carbon electrode was modified with GO, RGO, CuO, CuO-Au, CuS, CuS-Au, CuO-Au/RGO and CuS-Au/RGO nanomaterials/composites to determine the electrocatalytic activity using $[Fe(CN)_6]^{4-/3-}$ redox probe. CuS-Au/RGO modified GCEs were highly electro-active, this was confirmed by electrochemical impedance spectroscopy (EIS) and cyclic voltammetry (CV). The increased number of scans was shown to have no effect on the electrode sensitivities to the oxidation/reduction of $[Fe(CN)_6]^{-4/-3}$ on the surface of CuS-Au/RGO/GCE. This was explained by the extremely stable nanocomposite layer on the electrode surface. Attributed to the fact that the peak currents and peak potentials did not change as the number of scans increased, the CuS-Au/RGO nanocomposite was shown to be extremely stable on the electrode surface. The peak current versus square root of scan rate obeyed the Randles-Sevcik relationship indicating a diffusion-controlled electrochemical process. The diffusion co-efficient of the oxidation and reduction process was calculated to be 1.3×10^{-8} cm^2 s^{-1} and 1.5×10^{-8} cm^2 s^{-1} respectively. This confirmed fast electron transfer kinetics occurring at the electrode surface and that the oxidation and reduction processes occurred almost at the same rate. The CuS-Au/RGO nanocomposite was then utilized to fabricate an electrochemical sensor for two different toxic heavy metal ions. A CuS-Au/RGO/GCE sensing platform was developed for the detection of Chromium(III) and mercury(II). The fabricated sensor exhibited great sensitivity towards Hg (II) (LoD=2 ppb) and Cr(III) (LoD=2 ppb). Both detection limits for Hg (II) and Cr(III) were significantly lower than other sensing platforms reported in literature.

Recommendations

There should be a further study investigating the effect of temperature on the sensitivity of the fabricated sensor. Selectivity studies should also be done, to investigate the selectivity of the fabricated sensor to Cr(III) and Hg(II) in the presence of other interfering species or heavy metals.

Acknowledgments

Would like to express my gratitude to the University of Limpopo and all the students and staff members in the Department of Chemistry for the unwavering support. This research was sponsored by National Research Foundation (NRF).

Appendix A1: Fitting and simulation of Bare GCE, CuO/GCE, CuS/GCE, CuO-Au/GCE, CuS-Au/GCE, CuO-Au/RGO/GCE, CuS-Au-/RGO/GCE, GO/GCE and RGO/GCE

1. **GCE Bare**

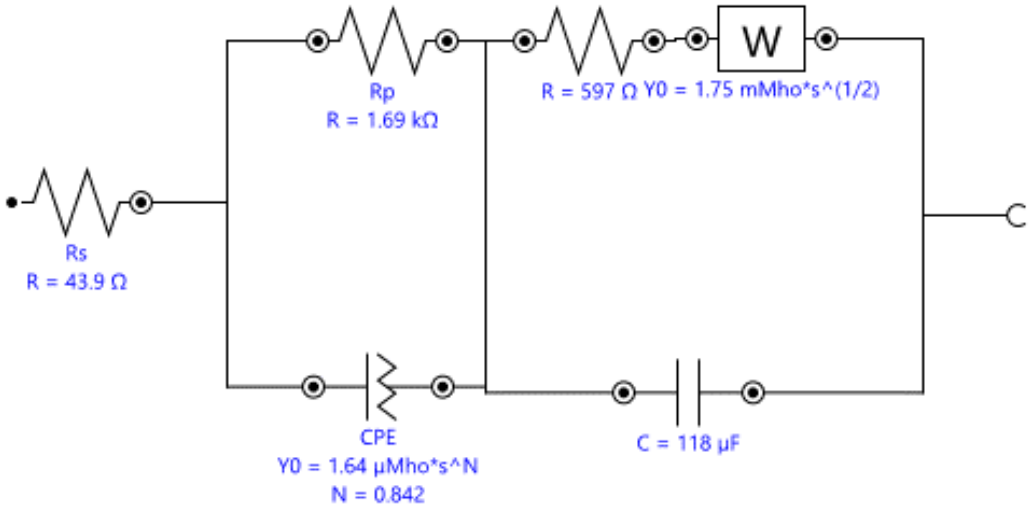

Element	Parameter	Value	Estimated Error (%)
Rs	R	43.889	1.144
Rp	R	1690.3	0.923
CPE	Y0	1.6401E-06	3.716
	N	0.84173	0.477
R1	R	596.63	4.267
C1	C	0.0001176	8.112
W1	Y0	0.0017503	2.547
	χ^2	0.046366	

2. GCE/CuS(GSH)

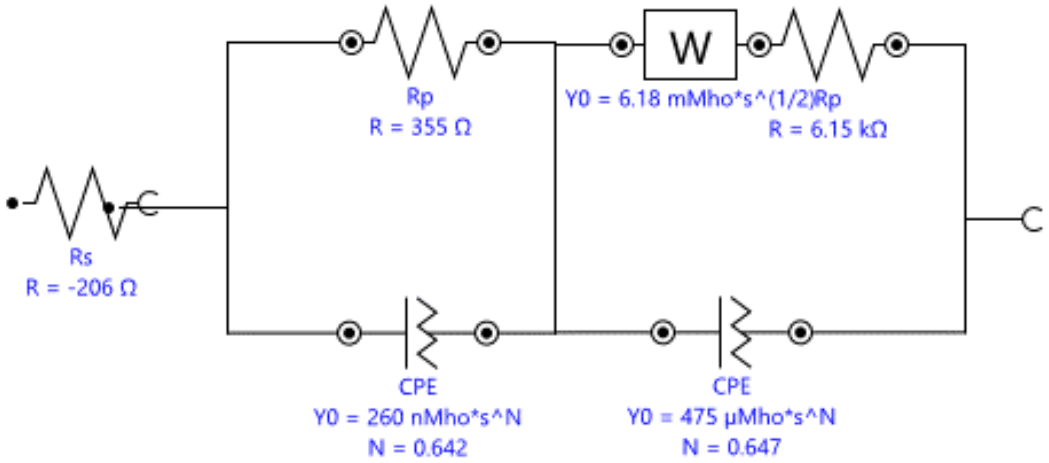

Element	Parameter	Value	Estimated Error (%)
Rs	R	-205.56	-57.992
CPE	Y0	2.605E-07	41.650
	N	0.64184	11.545
Rp	R	354.85	34.242
W1	Y0	0.00618	131.858
CPE	Y0	0.00047474	4.536
	N	0.64659	2.553
Rp	R	6152.4	13.515
	χ^2	0.41763	

3. **GCE/GO**

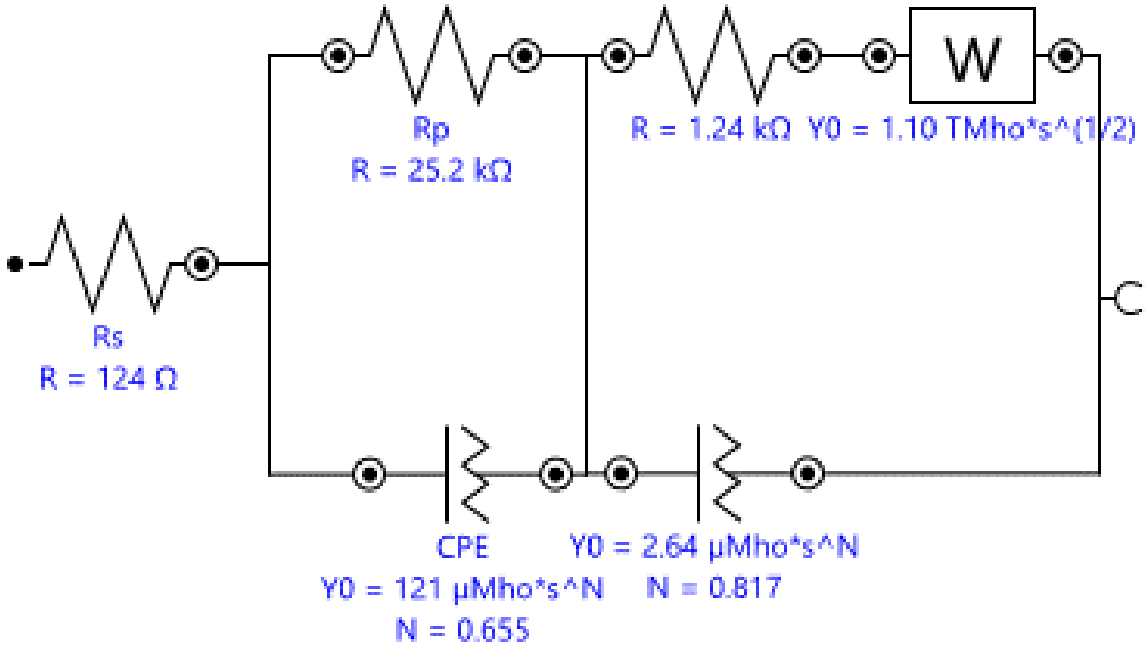

Element	Parameter	Value	Estimated Error (%)
Rs	R	123.86	1.989
Rp	R	25204	27.061
CPE	Y0	0.00012072	10.302
	N	0.65457	5.102
R1	R	1240.2	4.592
Q1	Y0	2.643E-06	12.765
	N	0.81708	1.910
W1	Y0	1.1E+12	97657803220776000.000
	χ^2	0.20663	

4. **GCE/RGO**

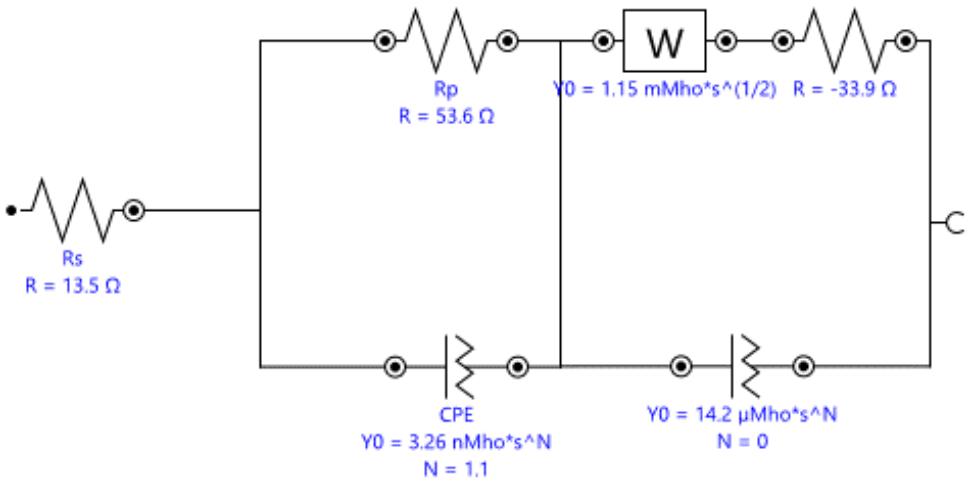

Element	Parameter	Value	Estimated Error (%)
Rs	R	13.465	0.000
Rp	R	53.565	0.000
CPE	Y0	3.2624E-09	0.000
	N	1.1	0.000
W1	Y0	0.0011514	0.000
Q1	Y0	1.4158E-05	0.000
	N	0	0.000
R1	R	-33.924	0.000
	χ^2	0.016795	

5. **GCE/[CuS/RGO]**

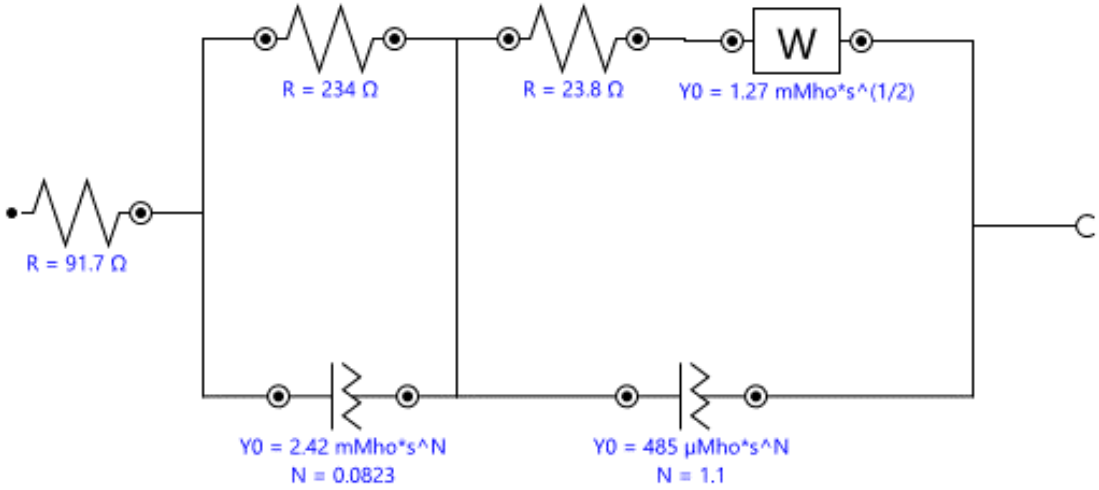

Element	Parameter	Value	Estimated Error (%)
R1	R	91.686	1526.217
R2	R	233.57	1528.046
Q1	Y0	0.002418	200.771
	N	0.082334	1503.258
R3	R	23.841	20756.498
Q2	Y0	0.00048473	1556.996
	N	1.1	173.136
W1	Y0	0.001267	8.625
	χ^2	0.19725	

6. **GCE/[CuS-Au]**

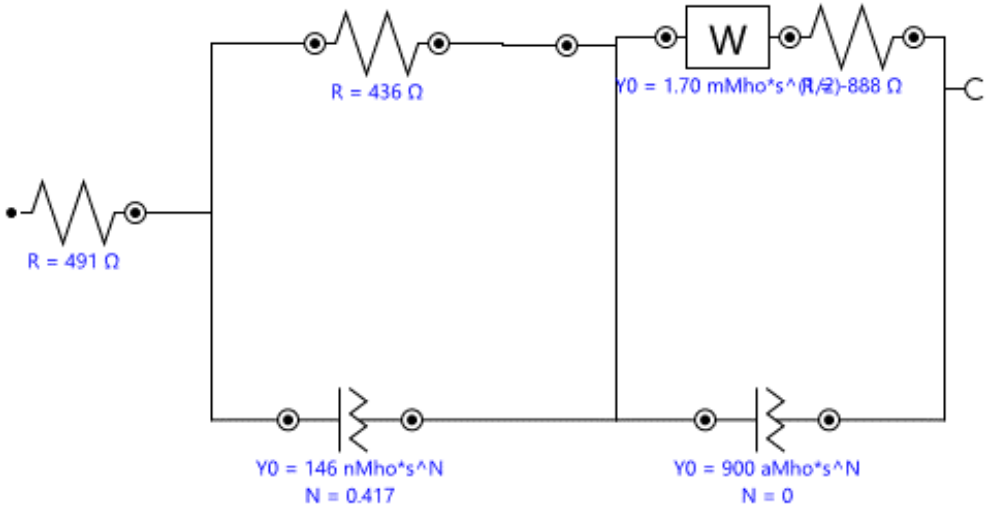

Element	Parameter	Value	Estimated Error (%)
R1	R	490.72	4033053.009
Q1	Y0	1.4649E-07	31229.428
	N	0.41664	359.143
R2	R	435.62	16528.821
W1	Y0	0.001704	4.464
Q2	Y0	9E-16	3689326271958.360
	N	0	∞
R3	R	-888.48	-2227547.692
	χ^2	0.67405	

7. **GCE/[CuS-Au/RGO]**

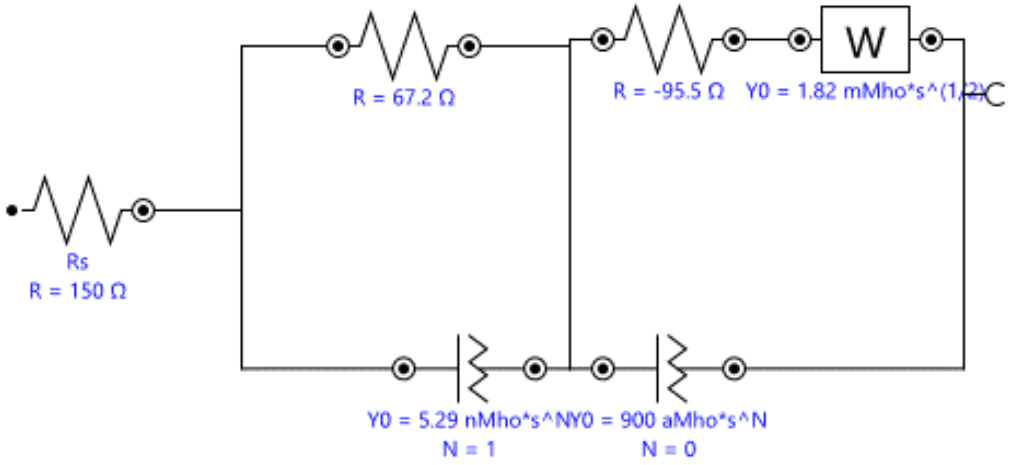

Element	Parameter	Value	Estimated Error (%)
Rs	R	150.2	0.000
R1	R	67.191	381.365
Q1	Y0	5.2879E-09	382.858
	N	0.99953	40.449
R2	R	-95.547	0.000
Q2	Y0	9E-16	2649926845333.600
	N	0	∞
W1	Y0	0.0018205	1.499
	χ^2	0.17656	

8. **GCE/[CuO]**

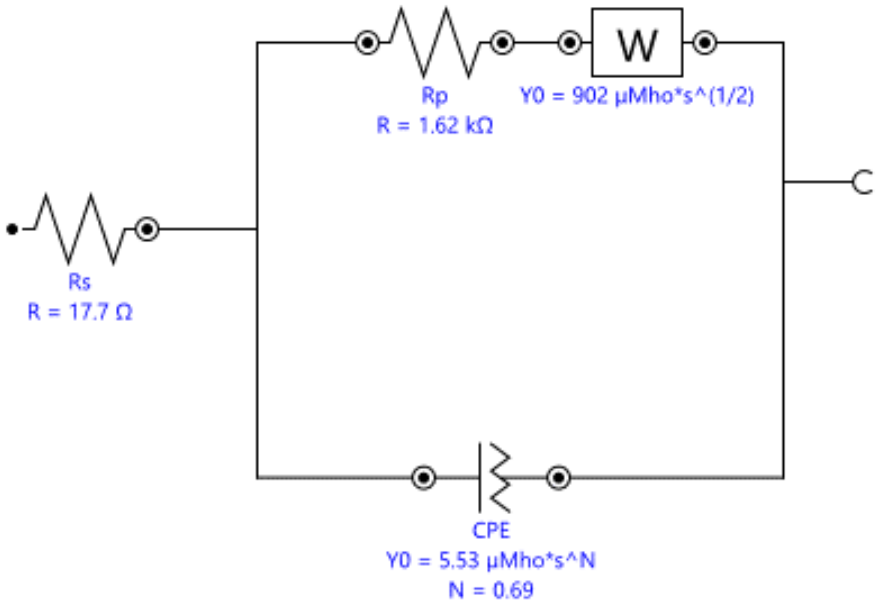

Element	Parameter	Value	Estimated Error (%)
Rs	R	17.686	16.395
Rp	R	1618.3	3.594
CPE	Y0	5.5253E-06	16.472
	N	0.69045	2.507
W1	Y0	0.00090177	5.840
	χ^2	1.0736	

9. **GCE/[CuO/RGO]**

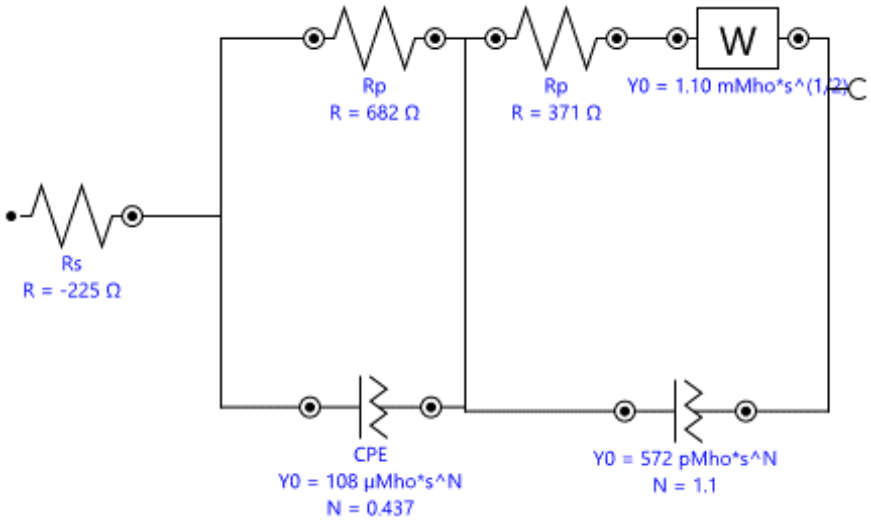

Element	Parameter	Value	Estimated Error (%)
Rs	R	-224.66	-28.499
CPE	Y0	0.00010771	13.645
	N	0.43687	5.108
Rp	R	682.32	4.611
Rp	R	370.77	18.646
Q1	Y0	5.7165E-10	48.580
	N	1.1	5.281
W1	Y0	0.0011047	1.782
	χ^2	0.089942	

10. **GCE/[CuO-Au/RGO]**

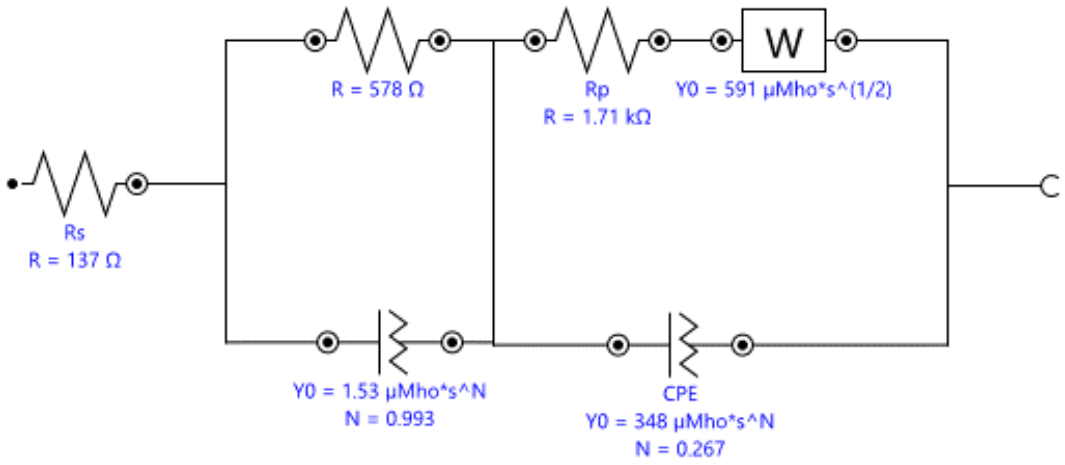

11.

Element	Parameter	Value	Estimated Error (%)
Rs	R	137.33	22.614
R1	R	578.36	19.870
Q1	Y0	1.5269E-06	66.410
	N	0.99268	10.272
Rp	R	1713.9	33.017
CPE	Y0	0.00034832	33.576
	N	0.26701	14.575
W1	Y0	0.00059071	57.108
	χ^2	0.7849	